UNIVERSITY OF SOUTHAMPTON

FACULTY OF ENGINEERING AND THE ENVIRONMENT

Aeronautics, Astronautics and Computational Engineering

Skyrmionic states in confined helimagnetic nanostructures

by

Marijan Beg

Thesis for the degree of Doctor of Philosophy

April 2016

UNIVERSITY OF SOUTHAMPTON

ABSTRACT

FACULTY OF ENGINEERING AND THE ENVIRONMENT
Aeronautics, Astronautics and Computational Engineering

Doctor of Philosophy

SKYRMIONIC STATES IN CONFINED HELIMAGNETIC NANOSTRUCTURES

by Marijan Beg

Magnetic skyrmions have the potential to provide solutions for low-power, high-density data storage and processing. One of the major challenges in developing skyrmion-based devices is the skyrmions' magnetic stability in confined helimagnetic nanostructures. Through a systematic study of equilibrium states, using a full three-dimensional micromagnetic model, we demonstrate that skyrmionic states are the lowest energy states in confined helimagnetic nanostructures at zero external magnetic field and in absence of magnetocrystalline anisotropy. We show that bistable skyrmionic states undergo hysteretic behaviour between two energetically equivalent skyrmionic configurations with different core orientation, even in the absence of both magnetocrystalline and demagnetisation-based shape anisotropies, suggesting the existence of novel Dzyaloshinskii-Moriya-based shape anisotropy. We show that the skyrmionic state core reversal is facilitated by the Bloch point occurrence and propagation. In this work, we also study the dynamic properties (resonance frequencies and corresponding eigenmodes) of these skyrmionic states in confined helimagnetic nanostructures. The eigenvalue method allows us to identify all resonance frequencies and corresponding eigenmodes that can exist in the simulated system. However, using a particular experimentally feasible excitation can excite only a limited set of eigenmodes. Because of that, we perform and report ringdown simulations that resemble the experimental setup using both an in-plane and an out-of-plane excitations. In addition, we report the nonlinear dependence of resonance frequencies on the external magnetic bias field and disk sample diameter and report the possible reversal mode of skyrmionic states. Finally, we show that neglecting the demagnetisation energy contribution or ignoring the magnetisation variation in the out-of-film direction in either static or dynamic simulations is not always justified.

Dedicated to the memory of my mother

Contents

List of figures

List of publications

1. A. Baker, **M. Beg**, G. Ashton, M. Albert, D. Chernyshenko, W. Wang, S. Zhang, M.-A. Bisotti, M. Franchin, C. Lian Hu, R. L. Stamps, T. Hesjedal, and H. Fangohr. Proposal of a micromagnetic standard problem for ferromagnetic resonance simulations. *Journal of Magnetism and Magnetic Materials* **421**, 428-439 (2017).

2. **M. Beg**, M. Albert, M.-A. Bisotti, D. Cortés-Ortuño, W. Wang, R. Carey, M. Vousden, O. Hovorka, C. Ciccarelli, C. S. Spencer, C. H. Marrows, and H. Fangohr. Dynamics of skyrmionic states in confined helimagnetic nanostructures. (*under review*) preprint: *arXiv* 1604.08347 (2016).

3. **M. Beg**, R.A. Pepper, and H. Fangohr, User interfaces for computational science: a domain specific language for OOMMF embedded in Python. *(under review)* preprint: *arXiv* 1609.07432 (2016).

4. R. Carey, **M. Beg**, M. Albert, M.-A. Bisotti, D. Cortés-Ortuño, M. Vousden, W. Wang, O. Hovorka, and H. Fangohr. Hysteresis of nanocylinders with Dzyaloshinskii-Moriya interaction. *Applied Physics Letters* **109**, 122401 (2016).

5. M. Albert, **M. Beg**, D. Chernyshenko, M.-A. Bisotti, R. L. Carey, H. Fangohr, and P. J. Metaxas. Frequency-based nanoparticle sensing over large field ranges using the ferromagnetic resonances of a magnetic nanodisc. *Nanotechnology* **27**, 455502 (2016).

6. M. Vousden, M. Albert, **M. Beg**, M.-A. Bisotti, R. Carey, D. Chernyshenko, D. Cortés-Ortuño, W. Wang, O. Hovorka, C. H. Marrows, and H. Fangohr. Skyrmions in thin films with easy-plane magnetocrystalline anisotropy. *Applied Physics Letters* **108**, 132406 (2016).

7. **M. Beg**, R. Carey, W. Wang, D. Cortés-Ortuño, M. Vousden, M.-A. Bisotti, M. Albert, D. Chernyshenko, O. Hovorka, R. L. Stamps, and H. Fangohr. Ground state search, hysteretic behaviour, and reversal mechanism of skyrmionic textures in confined helimagnetic nanostructures. *Scientific Reports* **5**, 17137 (2015).

8. W. Wang, M. Albert, **M. Beg**, M.-A. Bisotti, D. Chernyshenko, D. Cortés-Ortuño, I. Hawke, and H. Fangohr. Magnon driven domain wall motion with Dzyaloshinskii-Moriya interaction. *Physical Review Letters* **114**, 087203 (2015).

9. W. Wang, **M. Beg**, B. Zhang, W. Kuch, and H. Fangohr. Driving magnetic skyrmions with microwave fields. *Physical Review B (Rapid Communications)* **92**, 020403 (2015).

10. W. Wang, M. Dvornik, M.-A. Bisotti, D. Chernyshenko, **M. Beg**, M. Albert, A. Vansteenkiste, B. V. Waeyenberge, A. N. Kuchko, V. V. Kruglyak, and H. Fangohr. Phenomenological description of the nonlocal magnetization relaxation in magnonics, spintronics, and domain-wall dynamics. *Physical Review B* **92**, 054430 (2015).

11. B. Zhang, W. Wang, **M. Beg**, H. Fangohr, and W. Kuch. Microwave-induced dynamic switching of magnetic skyrmion cores in nanodots. *Applied Physics Letters* **106**, 102401 (2015).

Declaration of authorship

I, Marijan Beg, declare that the thesis entitled *Skyrmionic states in confined helimagnetic nanostructures* and the work presented in the thesis are both my own, and have been generated by me as the result of my own original research. I confirm that:

- this work was done wholly or mainly while in candidature for a research degree at this University;
- where any part of this thesis has previously been submitted for a degree or any other qualification at this University or any other institution, this has been clearly stated;
- where I have consulted the published work of others, this is always clearly attributed;
- where I have quoted from the work of others, the source is always given. With the exception of such quotations, this thesis is entirely my own work;
- I have acknowledged all main sources of help;
- where the thesis is based on work done by myself jointly with others, I have made clear exactly what was done by others and what I have contributed myself;
- Parts of this work have been published as:
  - Chapters 3 and 4 in Beg, M. *et al.* Ground state search, hysteretic behaviour, and reversal mechanism of skyrmionic textures in confined helimagnetic nanostructures. *Scientific Reports* **5**, 17137 (2015), and
  - Chapter 5 in Beg, M. *et al.* Dynamics of skyrmionic states in confined helimagnetic nanostructures. *(under review)*, preprint: *arXiv* 1604.08347 (2016).

Signed:.....

Date:.....

Acknowledgements

I would like to thank my supervisor Prof. Hans Fangohr for giving me the opportunity to perform this work as well as for his support and guidance. I also acknowledge the support from the colleagues: Dr Weiwei Wang, David Cortés-Ortuño, Ryan A. Pepper, Rebecca Carey, Dr Maximilian Albert, Mark Vousden, Marc-Antonio Bisotti, Dr Dmitri Chernyshenko, Dr Thomas Kluyver, and Dr Ondrej Hovorka. I acknowledge discussions with Prof. Robert L. Stamps (University of Glasgow) and Dr Chiara Ciccarelli (University of Cambridge) whose ideas and results supported the findings in this work. IRIDIS High Performance Computing Facility was used extensively in this work and I acknowledge its use as well as the associated support services at the University of Southampton.

This work was financially supported from the EPSRC's Doctoral Training Centre (DTC) grant EP/G03690X/1 as well as from the Institute of Complex System Simulations at the University of Southampton.

Nomenclature

$\boldsymbol{\mu}$	magnetic moment
$\mathbf{r}$	position vector
$\mathbf{v}$	velocity
$\mathbf{p}$	momentum
$\mathbf{L}$	orbital angular momentum
$\mathbf{S}$	intrinsic angular momentum (spin)
$\mathbf{J}$	total angular momentum
$\mathbf{H}$	magnetic field
$\mathbf{H}_{\text{eff}}$	effective magnetic field
$\mathbf{M}$	magnetisation
$\mathbf{m}$	unit (normalised) magnetisation vector field
$\mathbf{d}$	Dzyaloshinskii vector
I	electric (charge) current
A	area
V	volume
E	energy
w	energy density
P	power
f	frequency
g	correctional g-factor
μ_0	magnetic constant
h	Planck constant
$\hbar$	reduced Planck constant
e	elementary charge
m_{e}	electron mass
γ	gyromagnetic ratio
μ_{B}	Bohr magneton
M_{s}	magnetisation saturation
D	Dzyaloshinskii-Moriya energy constant
K	uniaxial anisotropy energy constant
$\hat{\mathbf{u}}$	uniaxial anisotropy energy axis
J	exchange integral

A	exchange energy constant
λ	Landau-Lifshitz damping constant
α	Gilbert damping constant
S	skyrmion number
S_{a}	scalar value S_{a}
l_{ex}	exchange length
L_{D}	helical period
ε_{ijk}	Levi-Civita symbol
δ_{ij}	Kronecker delta
LL	Landau-Lifshitz equation
LLG	Landau-Lifshitz-Gilbert equation
FMR	FerroMagnetic Resonance
iSk	incomplete Skyrmion
Sk	isolated Skyrmion
T	Target
BP	Bloch Point
PSD	Power Spectral Density

Chapter 1

Introduction

An ever increasing need for data storage creates great challenges for the development of high-capacity storage devices that are cheap, fast, reliable, and robust. Nowadays, hard disk drive technology uses magnetic grains pointing up or down to encode binary data (0 or 1) in so-called perpendicular recording media. Practical limitations are well understood and dubbed the "magnetic recording trilemma" [1]. It defines a trade-off between three conflicting requirements: signal-to-noise ratio, thermal stability of the stored data, and the ability to imprint information. Because of these fundamental constraints, further progress requires radically different approaches.

In magnetic systems that lack some type of inversion symmetry, the Dzyaloshinskii-Moriya Interactions [2, 3, 4, 5] (DMI) may occur. The inversion asymmetry can be present in the magnetic system either because of a non-centrosymmetric crystal lattice [3] (helimagnetic material) or due to the interfaces between different materials which inherently lack inversion symmetry [6, 7]. Consequently, the DMI can be classified either as bulk or interfacial. DMI favours magnetic moments at neighbouring lattice sites to be perpendicular to each other, which is in contrast to the symmetric ferromagnetic exchange interaction which tends to align them parallel or antiparallel. When acting together, these two interactions mutually compete and find a compromise in the twist between two neighbouring magnetic moments which could result in a rich variety of different magnetisation textures. One of them is a topologically stable skyrmionic configuration, with particle-like properties.

Now, we give a basic overview of interactions that lead to the magnetic skyrmion formation. The first interaction we focus on is the exchange energy. The exchange energy for two neighbouring magnetic moments (spins) $\mathbf{S}_i$ and $\mathbf{S}_j$ equals to $-J\mathbf{S}_i \cdot \mathbf{S}_j$, where J is the exchange energy constant [8]. We can conclude that depending on the exchange energy constant, this energy tends to align two neighbouring spins either parallel ($J > 0$) or antiparallel ($J < 0$) in order to minimise its energy. Let us assume that the exchange energy constant is positive and parallel alignment (ferromagnetic order) is preferred.

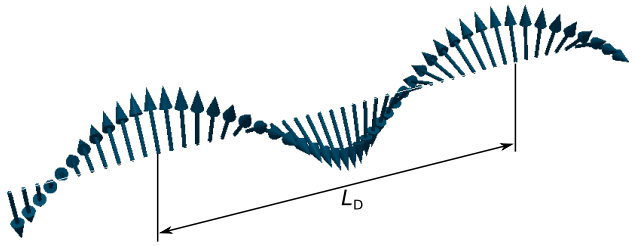

Figure 1.1: One-dimensional helical configuration with helical period L_D.

Also, it is worth noting that this interaction does not have a preferential direction in which all magnetic moments should be aligned. Two energies that introduce preferential directions to the magnetic configuration are Zeeman and magnetocrystalline anisotropy energies. Zeeman energy of a single magnetic moment $\boldsymbol{\mu}$ in external magnetic field $\mathbf{B}$ is $-\boldsymbol{\mu} \cdot \mathbf{B}$ [8]. In order to minimise itself, this energy tends to align the magnetic moment $\boldsymbol{\mu}$ in the same direction (parallel) to the external magnetic field $\mathbf{B}$. There are different types of magnetocrystalline anisotropy energies, and one of them is uniaxial anisotropy. The uniaxial anisotropy energy of a spin is $-k(\mathbf{S} \cdot \hat{\mathbf{u}})^2$, where k is the uniaxial anisotropy constant and $\hat{\mathbf{u}}$ is the uniaxial anisotropy axis [9]. This energy is minimum when spin is either parallel or antiparallel to $\hat{\mathbf{u}}$ if $k > 0$ (easy-axis anisotropy) or perpendicular to $\hat{\mathbf{u}}$ if $k < 0$ (easy-plane anisotropy). Both Zeeman and uniaxial anisotropy energies are local which is in contrast to the exchange energy. More precisely, both Zeeman and uniaxial anisotropy energies do not depend on the neighbouring spins, which is not the case with non-local exchange energy. Finally, the last non-local interaction we discuss now is the Dzyaloshinskii-Moriya energy, which between two neighbouring spins $\mathbf{S}_i$ and $\mathbf{S}_j$ is $\mathbf{d} \cdot (\mathbf{S}_i \times \mathbf{S}_j)$, where $\mathbf{d}$ is the Dzyaloshinskii vector [2, 3]. This energy tends to align two neighbouring spins perpendicular to each other so that they are in the plane which is perpendicular to the Dzyaloshinskii vector $\mathbf{d}$. The much more detailed overview of magnetic energies will be presented in Chapter 2.

However, rarely a single magnetic energy exists in the system, so let us predict what would be the preferential configuration if both exchange and DMI energies are present in the system. As we have previously seen, ferromagnetic exchange energy (with $J > 0$) tends to align two neighbouring magnetic moments so the the angle between them is $0°$ (parallel). On the other hand, Dzyaloshinskii-Moriya energy prefers a $90°$ angle (perpendicular configuration). Consequently, we can conclude that none of these two energies if acting together can be minimised. So, they mutually compete and find a compromise, which in this case would be an angle in the $[0°, 90°]$ range. This configuration is called a one-dimensional helical modulation and we show how this configuration looks like for an array of magnetic moments in Fig. 1.1. What is the angle between neighbouring magnetic moments depends on the relative strengths between ferromagnetic exchange and Dzyaloshinskii-Moriya energies. In other words, a length over which the spins cover a 2π angle, called the helical period L_D depends on J and D, so that

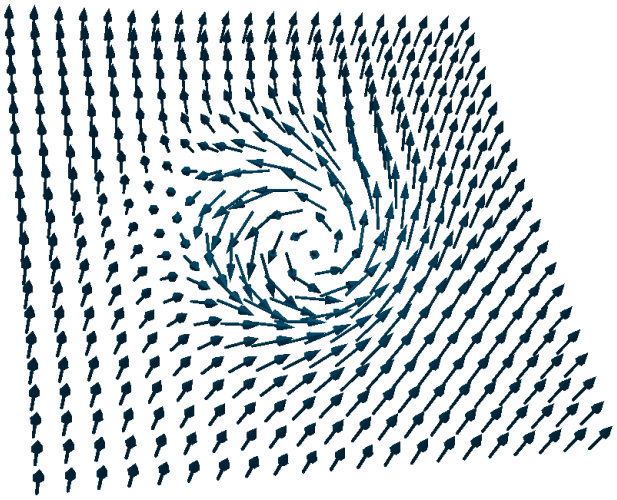

Figure 1.2: Two-dimensional chiral skyrmion configuration.

$L_{\mathrm{D}} \propto J/D$ [10, 11, 12, 13, 14, 15, 16, 17, 18]. Magnetic materials which support the formation of helical configurations are called the helimagnetic materials.

Helical configuration as a consequence of mutual competition between exchange and Dzyaloshinskii-Moriya energies was an example which could be easily intuitively understood. Now, let us assume we have a two-dimensional array of magnetic moments (spins) and all previously introduced energies (exchange, Dzyaloshinskii-Moriya, uniaxial anisotropy, and Zeeman) are present in the system. The question is: What is the magnetisation configuration which has the minimum energy for a particular set of energy parameters J, $\mathbf{D}$, k, and external magnetic field $\mathbf{B}$. We assume that both uniaxial anisotropy axis $\hat{\mathbf{u}}$ and external magnetic field $\mathbf{B}$ are out-of-plane. Now, it is highly non-intuitive what the preferred configuration would look like. One of the possible configurations that can emerge under these circumstances is the chiral skyrmion configuration, that we show in Fig. 1.2.

We see that a skyrmion looks like a whirl in the ferromagnetic background. All magnetic moments outside the skyrmion are in the opposite direction then a single magnetic moment at the skyrmion centre. If this configuration is mapped on a sphere, we could see that it covers the sphere exactly once. How many times a magnetisation configuration covers the sphere can be determined by computing the skyrmion number [19]

$$S = \frac{1}{4\pi} \int \mathbf{m} \cdot \left(\frac{\partial \mathbf{m}}{\partial x} \times \frac{\partial \mathbf{m}}{\partial y} \right) \mathrm{d}x\mathrm{d}y, \tag{1.1}$$

where $\mathbf{m}$ is the continuous magnetisation field and will be described in Chapter 2. For the skyrmion configuration, the skyrmion number value is $S = \pm 1$.

Recent research demonstrated that magnetic skyrmions have the potential for the development of future data storage and information processing devices, due to their competitive size [19, 20, 21] and easy manipulation using spin-polarised currents [22, 23]. For

instance, a skyrmion lattice formed in a monoatomic Fe layer grown on a Ir(111) surface [19] revealed skyrmions with diameters as small as a few atom spacings. In addition, it has been demonstrated that skyrmions can be easily manipulated using spin-polarised currents of the $10^6\,\mathrm{A\,m^{-2}}$ order [22, 23] which is a factor 10^5 to 10^6 smaller than the current densities required in conventional magneto-electronics. These unique skyrmion properties point to an opportunity for the realisation of ambitious novel high-density, power-efficient storage [24, 25] and logic [26] devices.

Magnetic skyrmions, after being predicted [27, 28, 29], were later experimentally observed in magnetic systems with both bulk [30, 31, 32, 33, 20, 16] and interfacial [19, 21] types of DMI. So far, a major challenge obstructing the development of skyrmion-based devices has been their thermal and magnetic stability [34]. Only recently, skyrmions were observed at the room temperature in magnetic systems with bulk [35] and interfacial [36, 37, 38] DMI. However, the magnetic stability of skyrmions in absence of external magnetic field was reported only for magnetic systems with interfacial DMI in one-atom layer thin films [19, 39], where the skyrmion state is stabilised in the presence of magnetocrystalline anisotropy.

The first focus of this work is on the zero-field stability of skyrmionic states in confined geometries of bulk DMI (helimagnetic) materials. Zero-field stability is a crucial requirement for the development of skyrmion-based devices: devices that require external magnetic fields to be stabilised are volatile, harder to engineer and consume more energy. We address the following questions that are relevant for the skyrmion-based data storage and processing nanotechnology. Can skyrmionic states be the ground state (i.e. have the lowest energy) in helimagnetic materials at zero external magnetic field, and if they can, what is the mechanism responsible for this stability? Do the demagnetisation energy and magnetisation variation along the out-of-film direction [40] have important contribution to the stability of skyrmionic states? Is the magnetocrystalline anisotropy an essential stabilisation mechanism? Are there any other equilibrium states that emerge in confined helimagnetic nanostructures? How robust are skyrmionic states against varying geometry? Do skyrmionic states undergo hysteretic behaviour in the presence of an external magnetic field (crucial for data imprint), and if they do, what is the skyrmionic state reversal mechanism?

Some stability properties of DMI-induced isolated skyrmions in two-dimensional confined systems have been studied analytically [41, 42, 43] and using simulations [39, 44]. However, in all these studies, either magnetocrystalline anisotropy or an external magnetic field (or both) are crucial for the stabilisation of skyrmionic states. In addition, an alternative approach to the similar problem, in absence of chiral interactions, where skyrmionic states can be stabilised at zero external magnetic field and at room temperature using a strong perpendicular anisotropy, has been studied analytically [45], experimentally [46, 47], as well as using simulations [48]. Our new results, and in particular the zero-field skyrmionic ground state in isotropic helimagnetic materials, can only

be obtained by allowing the chiral modulation of magnetisation direction along the film normal, which has recently been shown to radically change the skyrmion energetics [40].

In this work, we use a full three-dimensional simulation model that makes no assumption about translational invariance of magnetisation in the out-of-film direction and takes full account of the demagnetisation energy. We demonstrate, using this full model, that DMI-induced skyrmionic states in confined thin film helimagnetic nanostructures are the lowest energy states in the absence of both the stabilising external magnetic field and the magnetocrystalline anisotropy and are able to adapt their size to hosting nanostructures, providing the robustness for their practical use. We demonstrate that both the demagnetisation energy and the magnetisation variation in the out-of-film direction play an important role for the stability of skyrmionic states. In addition, we report the parameter space regions where other magnetisation configurations are in equilibrium. Moreover, we demonstrate that these zero-field stable skyrmionic states undergo hysteretic behaviour when their core orientation is changed using an external magnetic field, which is crucial for data imprint. The hysteretic behaviour remains present even in the absence of all relevant magnetic anisotropies (magnetocrystalline and demagnetisation-based shape anisotropies), suggesting the existence of a novel Dzyaloshinskii-Moriya-based shape anisotropy. We conclude the study by showing that the skyrmionic state core orientation reversal is facilitated by the Bloch point occurrence and propagation, where the Bloch point may propagate in either of the two possible directions. This work is based on the specific cubic helimagnetic B20 ($P2_13$ space group) material, FeGe with 70 nm helical period, in order to encourage the experimental verification of our predictions. Other materials could allow either to reduce the helical period [30, 20] and therefore the hosting nanostructure size or increase the operating temperature [35].

Understanding the dynamic response of skyrmionic states in confined helimagnetic nanostructures is of importance both from the aspect of fundamental physics as well as for their manipulation. In the second part of this work we explore the dynamics of three equilibrium skyrmionic states using a full three-dimensional model which includes the demagnetisation energy contribution and does not assume the translational invariance of magnetisation in the out-of-film direction. A similar dynamics simulation study was performed for the isolated skyrmion breathing eigenmodes [49] in confined two-dimensional samples with interfacial DMI; and high-frequency skyrmion spin excitations were analytically studied in thin cylindrical dots [50]. The low-frequency (two lateral and one breathing) eigenmodes were reported in two-dimensional simulations of a hexagonal skyrmion lattice [51], where the demagnetisation energy was neglected. Later, microwave absorption measurements explored the low frequency eigenmodes in Cu_2OSeO_3 [52, 53, 54], $Fe_{1-x}Co_xSi$ and MnSi [54] helimagnetic bulk samples. In the case of a magnetic bubble [45, 46, 47, 48] (skyrmionic state stabilised due to the strong uniaxial anisotropy in the absence of DMI) analytic [55], simulation [56], and experimental [57] studies reported the existence of two low frequency gyrotropic eigenmodes, suggesting that the

skyrmion possesses mass. In contrast, a recent analytic work [58] suggests that only one gyrotropic eigenmode exists in the confined DMI-induced skyrmion state, whereas another low-frequency lateral eigenmode can be interpreted as an azimuthal spin-wave mode [58].

Using our full three-dimensional model, employing the eigenvalue [59] method, we compute all existing (both lateral and breathing) eigenmodes below 50 GHz in three different skyrmionic states. In addition, using the ringdown [60] method, we determine what eigenmodes can be excited using two different experimentally feasible excitations (in-plane and out-of-plane). On the contrary to the magnetic bubble, in the confined DMI stabilised skyrmionic states we find the existence of only one low frequency gyrotropic eigenmode (characteristic of massless skyrmions). We also demonstrate the nonlinear dependence of eigenmode frequencies on the external magnetic bias field and the disk sample diameter, and show that the gyrotropic eigenmode might be the reversal mode of the studied states. After we identify all eigenmodes of incomplete Skyrmion (iSk) and isolated Skyrmion (Sk) ground states, we compare their Power Spectral Densities (PSDs) in the same sample at different external magnetic field values. We discuss these comparisons and observe several key differences that can contribute to the experimental identification of the state present in the studied sample. We experimentally measure the FeGe Gilbert damping, and using this value, show what power spectral densities are expected to be observed in experiments. Finally, we investigate how the demagnetisation energy contribution and magnetisation variation in the out-of-film direction affects the dynamics of skyrmionic states. We report that although the eigenmode magnetisation dynamics is not significantly affected, the resonance frequencies change substantially, concluding that ignoring the demagnetisation energy or modelling the thin film helimagnetic samples using two-dimensional meshes is not always justified. The results in this work, apart from the contribution to the fundamental physics, could support experimentalists to determine what magnetisation configuration is present in the confined helimagnetic sample by measuring ferromagnetic resonance spectra.

1.1 Thesis structure

In Chapter 2, the fundamental concepts of magnetism in condensed matter are introduced. A relation between the basic building block of magnetic materials – magnetic moment and angular momentum is described via gyrotropic ratio. After that, the dynamics of a magnetic moment in an external magnetic field is described by introducing Landau-Lifshitz-Gilbert (LLG) equation which consists of both precession and damping terms. Because magnetic materials are composed of a big number of magnetic moments, it is crucial to understand the interactions between them. We present symmetric exchange, Dzyaloshinskii-Moriya, uniaxial anisotropy, Zeeman, and demagnetisation interactions by showing their atomistic expressions as well as deriving their models in a continuous

form. Finally, we present the basic concepts of micromagnetics by introducing the basics of finite elements method, time integration, and describing the simulation tool that was used in this work. In Chapter. 3, we study the stability of skyrmionic states in confined helimagnetic nanostructures through a systematic study of equilibrium states. We find that skyrmionic states in the form of incomplete skyrmion and isolated skyrmion can emerge as the ground state in the studied system at zero external magnetic field and in absence of magnetocrystalline anisotropy. This is in contrast to infinitely large thin film helimagnetic samples, and because of that, we explore the possible stabilisation mechanism. We also demonstrate the robustness of skyrmionic states in confined helimagnetic nanostructures by showing they can adapt their size in order to accommodate the hosting nanostructure. Finally, we show that our results remain valid for an artificial helimagnetic material with ordering temperature above room temperature. In Chapter 4, we demonstrate that skyrmionic states exhibit hysteretic behaviour when the orientation between two energetically equivalent skyrmionic states is changed using an external magnetic field. We show that the reversal of an isolated skyrmion state is facilitated by the Bloch point occurrence and propagation, where its propagation direction strongly depends on the simulation parameters. Because understanding the dynamic response of skyrmionic states in confined helimagnetic nanostructures is important both for the fundamental physics and their manipulation, in Chapter 5, we simulate their dynamic properties using both eigenvalue and ringdown methods. We reveal how the resonance frequencies depend on disk sample diameter and external magnetic field. In addition, we compute the power spectral densities for the real value of FeGe Gilbert damping and explore whether demagnetisation energy and magnetisation variation in the out-of-film direction affect the dynamics of skyrmionic states. Chapter 6 provides the discussion of all results presented in this thesis and concludes the work.

Chapter 2

Magnetism and micromagnetics

In this chapter, we present the fundamental concepts of magnetism in condensed matter as well as computational micromagnetic models. Firstly, we define a basic building block of all magnetic materials – magnetic moment – as a consequence of angular momentum. Secondly, we present an equation governing its dynamics (Landau-Lifshitz-Gilbert equation) by deriving the precession term and introducing the phenomenological damping term. Magnetic moments at different atoms mutually interact with each other via different interactions as well as with their immediate environment, which can result in a rich variety of different magnetisation configurations that can emerge in a magnetic system. We introduce symmetric exchange, Dzyaloshinskii-Moriya, uniaxial anisotropy, Zeeman, and dipolar (demagnetisation) interactions by presenting their atomistic models and deriving their continuous energy and effective field expressions. Finally, we present the basics of finite element approximation of continuous functions and time integration, that we used for the simulation tool implementation.

2.1 Magnetic moment

A basic building block of any magnetic material is the magnetic moment $\boldsymbol{\mu}$. In conventional (macroscopic) electromagnetics, the magnetic moment emerges as a consequence of an electric current I in a closed loop of area A [61, 8], as shown in Fig. 2.1 (a). It is defined as

$$\boldsymbol{\mu} = I \int_A \mathrm{d}\mathbf{A}, \tag{2.1}$$

where $\mathrm{d}\mathbf{A} = \mathrm{d}A\hat{\mathbf{n}}$, with $\hat{\mathbf{n}}$ being the unit vector perpendicular to the plane containing $\mathrm{d}A$, whose direction is uniquely defined by the direction of current I [61, 8] in the closed loop.

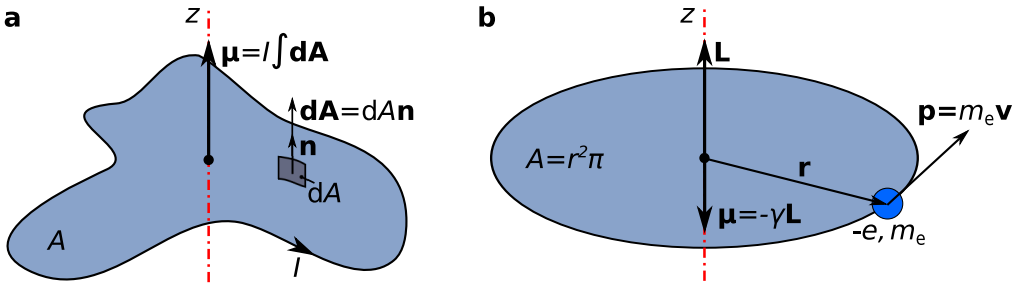

Figure 2.1: (**a**) The conventional electromagnetic definition of a magnetic moment as a consequence of current in the closed loop. (**b**) The magnetic moment of a single electron orbiting the atomic nucleus, where its relation with the angular momentum and the magnetic moment is given by the gyromagnetic ratio γ ($\boldsymbol{\mu} = -\gamma\mathbf{L}$). Due to the negative charge of an electron, vectors $\mathbf{L}$ and $\boldsymbol{\mu}$ are antiparallel (have opposite directions).

2.1.1 Gyromagnetic ratio

If the conventional electromagnetic definition of a magnetic moment is scaled down to an atomic level, we can make an analogy that an atomic magnetic moment is a consequence of an electric current produced by an electron orbiting the atomic nucleus. A fact that an orbiting electron has a mass m_e implies that it possesses an angular momentum $\mathbf{L}$. Therefore, one might attempt to find a relation between magnetic moment $\boldsymbol{\mu}$ and angular momentum $\mathbf{L}$. The relation between $\mathbf{L}$ and $\boldsymbol{\mu}$ was experimentally demonstrated [62, 63, 64] where the angular momentum was induced by changing the magnetisation of the magnetic sample and this effect is now called Einstein-de Haas effect. Similarly, an opposite effect – magnetisation occurrence by introducing the angular momentum to the system was also demonstrated [65] and we refer to it as the Barnett effect. The focus of this section is to derive the relation between electron's magnetic moment and its angular momentum.

In spite of being fundamentally wrong, an intuitive classical approach to magnetism can provide some useful insights that can be used when the magnetic moment concepts are studied from the quantum perspective. For instance, we can obtain the gyromagnetic ratio γ that establishes the relationship between magnetic moment and angular momentum. In the simplest Rutherford-Bohr model [66, 67] of a single electron with charge $-e$ and mass m_e orbiting the atomic nucleus, as shown in Fig. 2.1 (b), the electron's angular momentum is

$$\mathbf{L} = \mathbf{r} \times \mathbf{p} = r m_\mathrm{e} v \hat{\mathbf{z}}, \tag{2.2}$$

where $\mathbf{r}$ is the electron's position vector with respect to the atomic nucleus (r is the orbit's radius), which is perpendicular to the electron's linear velocity $\mathbf{v}$. In order to compute the magnetic moment, defined by Eq. (2.1), we must compute an electric current that an orbiting electron produces. This current is $I = e/\tau$, with $\tau = 2r\pi/v$ being the orbital

period. Consequently, the magnetic moment is

$$\boldsymbol{\mu} = I\mathbf{A} = -\frac{1}{2}evr\hat{\mathbf{z}}, \tag{2.3}$$

where $\mathbf{A} = r^2\pi\hat{\mathbf{z}}$ is the current loop area vector defined in Fig. 2.1 (a). Please note that the direction of current I is opposite to the electron's orbiting direction. After we found both the angular momentum $\mathbf{L}$ and the magnetic moment $\boldsymbol{\mu}$, we can establish a relation between them as

$$\boldsymbol{\mu} = -\frac{e}{2m_\mathrm{e}}\mathbf{L} = -\gamma\mathbf{L}, \tag{2.4}$$

where $\gamma = e/2m_\mathrm{e} > 0$ is called the gyromagnetic ratio. The minus sign is present in the gyromagnetic relation due to the negative charge of an electron. This means that the electron's magnetic moment $\boldsymbol{\mu}$ and its angular momentum $\mathbf{L}$ are always antiparallel (have opposite directions) as shown in Fig. 2.1 (b).

2.1.2 Quantised angular momentum

In the previously presented classical approach to the magnetic moment, where we established how it is related to the angular momentum, electron's velocity vector $\mathbf{v}$ changes its direction as the electron orbits the atomic nucleus. This would result in the electromagnetic energy radiation, violating the energy conservation law. In addition, the classical model of magnetism also fails to explain a wide range of different magnetic phenomena. Because of that, a fundamentally different quantum approach to the analysis of angular momentum is required.

The fundamental commutation relations of angular momentum $\mathbf{J}$ are [68, 69, 70, 71]

$$[J_i, J_j] = i\hbar\varepsilon_{ijk}J_k, \tag{2.5}$$

where J_i, J_j, and J_k are the components of angular momentum vector $\mathbf{J}$, ε_{ijk} is the Levi-Civita symbol, $\hbar = h/2\pi$ is the reduced Planck constant, and i is the imaginary unit. In this section, we use symbol $\mathbf{J}$ for the atomic angular momentum and later we will show that it is actually a sum of orbital $\mathbf{L}$ and intrinsic (spin) $\mathbf{S}$ angular momenta. If we define a ladder operator as $J_\pm = J_x \pm iJ_y$ and knowing that $\mathbf{J}^2 = J_xJ_x + J_yJ_y + J_zJ_z$, we can show that $[\mathbf{J}^2, J_z] = 0$, $[J_z, J_\pm] = \pm\hbar J_\pm$, and $[\mathbf{J}^2, J_\pm] = 0$, which will be used later. The zero value of $[\mathbf{J}^2, J_z]$ implies that the operators $\mathbf{J}^2$ and J_z commute and that their observables can be mutually known. Subsequently, we will determine what are their eigenvalues, which would allow us to compute the atomic magnetic moment $\boldsymbol{\mu}$ and its z component μ_z.

We can assume that an eigenket of both $\mathbf{J}^2$ and J_z is $|a, b\rangle$, so that

$$\mathbf{J}^2 |a, b\rangle = a |a, b\rangle , \tag{2.6}$$

$$J_z \left|a, b\right\rangle = b \left|a, b\right\rangle , \tag{2.7}$$

where a and b are eigenvalues of $\mathbf{J}^2$ and J_z operators, respectively. Now, we can compute how the eigenvalue of operator $\mathbf{J}^2$ changes after the ladder operator is applied on the eigenket $|a, b\rangle$. Knowing that $\mathbf{J}^2$ and $J_\pm$ mutually commute ($[\mathbf{J}^2, J_\pm] = 0$), we obtain

$$\mathbf{J}^2(J_\pm \left|a, b\right\rangle) = J_\pm(\mathbf{J}^2 \left|a, b\right\rangle) = J_\pm(a \left|a, b\right\rangle) = a(J_\pm \left|a, b\right\rangle). \tag{2.8}$$

This shows that applying the ladder operator on eigenket $|a, b\rangle$ does not change the eigenvalue of $\mathbf{J}^2$. On the other hand, knowing the commutation relation $[J_z, J_\pm] = \pm\hbar J_\pm$, for the operator J_z, we get

$$\begin{aligned} J_z(J_\pm \left|a, b\right\rangle) &= [J_z, J_\pm] \left|a, b\right\rangle + J_\pm(J_z \left|a, b\right\rangle) \\ &= \pm\hbar J_\pm \left|a, b\right\rangle + J_\pm(b \left|a, b\right\rangle) \\ &= (b \pm \hbar)(J_\pm \left|a, b\right\rangle). \end{aligned} \tag{2.9}$$

We conclude that if the ladder operator $J_\pm$ is applied on the eigenket $|a, b\rangle$, the z component of angular momentum changes by $\pm\hbar$, while the angular momentum magnitude remains unchanged. Intuitively, because the angular momentum component value cannot exceed its magnitude ($J_z^2 \leq \mathbf{J}^2$), we can impose a relation between eigenvalues a and b as $b^2 \leq a$. This condition implies that there are eigenkets $|a, b_{\max}\rangle$ and $|a, b_{\min}\rangle$, so that applying the raising or lowering operator is not allowed (results in the zero state): $J_+ \left|a, b_{\max}\right\rangle = 0$ and $J_- \left|a, b_{\min}\right\rangle = 0$. At this point, we can show that

$$\begin{aligned} J_-(J_+ \left|a, b_{\max}\right\rangle) &= (J_- J_+) \left|a, b_{\max}\right\rangle \\ &= (\mathbf{J}^2 - J_z^2 - \hbar J_z) \left|a, b_{\max}\right\rangle \\ &= (a^2 - b_{\max}^2 - \hbar b_{\max}) \left|a, b_{\max}\right\rangle \end{aligned} \tag{2.10}$$

and

$$\begin{aligned} J_+(J_- \left|a, b_{\min}\right\rangle) &= (J_+ J_-) \left|a, b_{\min}\right\rangle \\ &= (\mathbf{J}^2 - J_z^2 + \hbar J_z) \left|a, b_{\min}\right\rangle \\ &= (a^2 - b_{\min}^2 + \hbar b_{\min}) \left|a, b_{\min}\right\rangle . \end{aligned} \tag{2.11}$$

Because the obtained eigenvalues $a^2 - b_{\max}^2 - \hbar b_{\max}$ and $a^2 - b_{\min}^2 + \hbar b_{\min}$ are both zero, we get a relation $b_{\max}(b_{\max} + \hbar) = b_{\min}(b_{\min} - \hbar)$. This relation results in two possible solutions: physically impossible $b_{\min} = b_{\max} + \hbar$ and physically possible $b_{\max} = -b_{\min}$. Because the $b_{\max}$ value can be obtained by $N \in \mathbb{N}^0$ successive applications of the raising operator L_+ on $|a, b_{\min}\rangle$, we can write $b_{\max} = b_{\min} + N\hbar$. From this relation we get that $b_{\max} = (N/2)\hbar$ and total angular momentum quantum number $j \equiv b_{\max}/\hbar = N/2$ can be defined. Now, we know that the maximum eigenvalue of J_z is $j\hbar$, and that we can express any eigenvalue of J_z as $m\hbar$, where $m = -j, -j+1, -j+2, \ldots, j-2, j-1, j$. From these relations, we can determine eigenvalues $a = \sqrt{b_{\max}(b_{\max} + \hbar)} = \hbar\sqrt{j(j+1)}$

and $b = m\hbar$. Finally, if we change the eigenket notation from $|a, b\rangle$ to $|j, m\rangle$, we can write

$$\mathbf{J}^2 |j, m\rangle = \hbar^2 j(j+1) |j, m\rangle , \tag{2.12}$$

$$J_z |j, m\rangle = \hbar m |j, m\rangle , \tag{2.13}$$

where $j = N/2$ ($N \in \mathbb{N}^0$) is any half integer number and $m = -j, -j+1, -j+2, \ldots j-2, j-1, j$ has $2j+1$ possible values.

In reality, the atomic angular momentum $\mathbf{J}$ is a sum of two fundamentally different angular momenta – orbital angular momentum $\mathbf{L}$ and intrinsic angular momentum (spin) $\mathbf{S}$:

$$\mathbf{J} = \mathbf{L} + \mathbf{S}, \tag{2.14}$$

The general theory of quantum angular momentum previously presented remains valid for both $\mathbf{L}$ and $\mathbf{S}$. The orbital angular momentum emerges as a consequence of electron's wave function in the central potential of nucleus and it is determined by the integer quantum numbers $l \in \mathbb{N}$ and $m_l = -l, -l+1, -l+2, \ldots l-2, l-1, l$ [8, 72, 73]. We can conclude that the orbital angular momentum cannot have any value from a continuous set of values, but it takes a value from a discrete set as it was firstly postulated by Bohr [66, 67]. Accordingly, the orbital angular momentum magnitude μ_l and its z component μ_l^z are

$$\mu_l = -\gamma\hbar\sqrt{l(l+1)}, \tag{2.15}$$

$$\mu_l^z = -\gamma\hbar m_l. \tag{2.16}$$

Electron's orbital angular momentum component for $m_l = 1$ is $L_z = \hbar$ and the associated magnetic moment is $\mu_l^z = -\gamma\hbar = -e\hbar/2m_\mathrm{e} \equiv \mu_\mathrm{B}$. This value is also known as Bohr magneton μ_B and it is usually used as a "unit" for expressing the value of a magnetic moment.

Orbital magnetic moment fails to explain some of the magnetic phenomena, due to the existence of an additional electron's angular momentum as discovered by Stern and Gerlach [74]. The Stern-Gerlach experiment showed that electrons possess a quantised intrinsic angular momentum, also known as spin [75, 76], whose z component may have just one of the two possible values: $-\hbar/2$ or $\hbar/2$. In other words, intrinsic angular momentum is defined by two quantum numbers: $s = 1/2$ and $m_s = -1/2, 1/2$. The spin magnetic moment magnitude μ_s is

$$\mu_\mathrm{s} = -g\gamma\hbar\sqrt{s(s+1)} = g\gamma\hbar\frac{\sqrt{3}}{2}, \tag{2.17}$$

where $g \approx 2$ is the correctional g-factor [77]. The gyromagnetic ratio for the spin magnetic moment is two times larger than the gyromagnetic ratio for the orbital magnetic

moment. Similarly, the z component of a spin magnetic moment is

$$\mu_{\mathrm{s}}^{z} = -g\gamma\hbar m_s = \pm\frac{1}{2}g\gamma\hbar. \tag{2.18}$$

Because of the very common quenching of the orbital angular momentum in a very wide range of different magnetic materials, the magnetic moment is primarily determined by an intrinsic magnetic moment and the orbital magnetic moment can usually be neglected. Due to this, a single atomic magnetic moment $\boldsymbol{\mu}$ is usually referred to as spin $\mathbf{S}$. The atomic magnetic moment expressions presented in this section are valid for isolated atoms. However, in magnetic materials, magnetic moments are associated to atoms that constitute a crystal lattice, which further modifies the value of atomic magnetic moment in some cases.

2.2 Landau-Lifshitz-Gilbert equation

In this section, the Landau-Lifshitz-Gilbert (LLG) equation, governing the magnetic moment dynamics is presented by introducing its two (precession and damping) terms. Because the magnetic moment is always associated with the angular momentum, its dynamics in an external magnetic field is not as simple as in the case of an electric dipole. Therefore, the equation of motion must be derived taking into account the angular momentum.

From the Heisenberg picture of quantum mechanics [68, 70]

$$\frac{\mathrm{d}}{\mathrm{d}t}A(t) = \frac{i}{\hbar}[H, A(t)], \tag{2.19}$$

where $A(t)$ is the time-dependent operator and H is the system's Hamiltonian operator, the rate of change of angular momentum x component is

$$\begin{aligned}
\frac{\mathrm{d}}{\mathrm{d}t}J_x &= \frac{i}{\hbar}[H, J_x] \\
&= \frac{i}{\hbar}\left[\frac{\partial H}{\partial J_x}[J_x, J_x] + \frac{\partial H}{\partial J_y}[J_y, J_x] + \frac{\partial H}{\partial J_z}[J_z, J_x]\right] \\
&= \frac{i}{\hbar}\left[\frac{\partial H}{\partial J_y}(-i\hbar J_z) + \frac{\partial H}{\partial J_z}i\hbar J_y\right] \\
&= \frac{\partial H}{\partial J_y}J_z - \frac{\partial H}{\partial J_z}J_y,
\end{aligned} \tag{2.20}$$

where we obtain the values of commutators $[J_x, J_x]$, $[J_x, J_x]$, and $[J_x, J_x]$ from the commutation relations, given in Eq. 2.5. Also, we used the relation $[f(A), B] = \partial f/\partial A[A, B]$.

Similarly, the rates of change of J_y and J_z are

$$\begin{aligned}\frac{\mathrm{d}}{\mathrm{d}t}J_y &= \frac{i}{\hbar}[H, J_y] \\ &= \frac{i}{\hbar}\left[\frac{\partial H}{\partial J_x}[J_x, J_y] + \frac{\partial H}{\partial J_y}[J_y, J_y] + \frac{\partial H}{\partial J_z}[J_z, J_y]\right] \\ &= \frac{i}{\hbar}\left[\frac{\partial H}{\partial J_x}i\hbar J_z + \frac{\partial H}{\partial J_z}(-i\hbar J_x)\right] \\ &= \frac{\partial H}{\partial J_z}J_x - \frac{\partial H}{\partial J_x}J_z\end{aligned} \tag{2.21}$$

and

$$\begin{aligned}\frac{\mathrm{d}}{\mathrm{d}t}J_z &= \frac{i}{\hbar}[H, J_z] \\ &= \frac{i}{\hbar}\left[\frac{\partial H}{\partial J_x}[J_x, J_z] + \frac{\partial H}{\partial J_y}[J_y, J_z] + \frac{\partial H}{\partial J_z}[J_z, J_z]\right] \\ &= \frac{i}{\hbar}\left[\frac{\partial H}{\partial J_x}(-i\hbar J_y) + \frac{\partial H}{\partial J_y}i\hbar J_x\right] \\ &= \frac{\partial H}{\partial J_x}J_y - \frac{\partial H}{\partial J_y}J_x.\end{aligned} \tag{2.22}$$

Accordingly, the rate of change of the angular momentum vector $\mathbf{J}$ is

$$\frac{\mathrm{d}\mathbf{J}}{\mathrm{d}t} = \left(\frac{\partial H}{\partial J_y}J_z - \frac{\partial H}{\partial J_z}J_y, \frac{\partial H}{\partial J_z}J_x - \frac{\partial H}{\partial J_x}J_z, \frac{\partial H}{\partial J_x}J_y - \frac{\partial H}{\partial J_y}J_x\right), \tag{2.23}$$

which can be written as

$$\frac{\mathrm{d}\mathbf{J}}{\mathrm{d}t} = -\mathbf{J} \times \frac{\partial H}{\partial \mathbf{J}}, \tag{2.24}$$

if $\partial H/\partial \mathbf{J}$ is defined as $(\partial H/\partial J_x, \partial H/\partial J_y, \partial H/\partial J_z)$. Knowing that $\boldsymbol{\mu} = -\gamma\mathbf{J}$, Eq. 2.24 can be written as

$$\frac{\mathrm{d}\boldsymbol{\mu}}{\mathrm{d}t} = \gamma\boldsymbol{\mu} \times \frac{\partial H}{\partial \boldsymbol{\mu}}. \tag{2.25}$$

The derivative of the Hamiltonian with respect to the magnetic moment $\partial H/\partial\boldsymbol{\mu}$ results in a vector, which is called the effective field $\mathbf{B}_{\mathrm{eff}} = \mu_0\mathbf{H}_{\mathrm{eff}}$. We can now write the rate of change of magnetic moment as

$$\frac{\mathrm{d}\boldsymbol{\mu}}{\mathrm{d}t} = \gamma\mu_0\boldsymbol{\mu} \times \mathbf{H}_{\mathrm{eff}}. \tag{2.26}$$

This is the equation of precessive motion of a single atomic magnetic moment. However, in micromagnetics, instead of studying all atomic magnetic moments individually, a continuous vector field $\mathbf{M}$, called magnetisation, is considered. It is defined as a spatial density of atomic magnetic moments

$$\mathbf{M} = \frac{\sum_{i\in\mathrm{V}}\boldsymbol{\mu}_i}{V}. \tag{2.27}$$

This way, the atomistic structure of a studied material is ignored and the whole material can be considered as a single continuous domain.

In general, the magnetisation is a function of both space and time $\mathbf{M} = \mathbf{M}(\mathbf{r}, t)$, but due to simplicity, this dependence is usually omitted in writing. In micromagnetics the magnetisation vector field $\mathbf{M}$ must satisfy the following two assumptions:

1. The magnetisation vector field $\mathbf{M}$ is continuous and slowly changing in both space $\mathbf{r}$ and time t.
2. The magnitude of magnetisation $M_\mathrm{s} = |\mathbf{M}|$ is constant and both space and time invariant. Consequently, the magnetisation can be written as $\mathbf{M} = M_\mathrm{s}\mathbf{m}$, where M_s is called the saturation magnetisation and $\mathbf{m}$ is the unit vector field $|\mathbf{m}| = 1$.

If we use a definition of the magnetisation field $\mathbf{M} = M_\mathrm{s}\mathbf{m}$ and define the effective field as

$$\mathbf{H}_\mathrm{eff} = \frac{1}{\mu_0}\mathbf{B}_\mathrm{eff} = \frac{1}{\mu_0}\left(-\frac{\delta E[\mathbf{m}]}{\delta \mathbf{M}}\right) = -\frac{1}{\mu_0 M_\mathrm{s}}\frac{\delta E[\mathbf{m}]}{\delta \mathbf{m}}, \tag{2.28}$$

where $E[\mathbf{m}]$ is the total magnetic energy functional, which will be discussed in Sec. 2.3, the precession term becomes

$$\frac{\mathrm{d}\mathbf{m}}{\mathrm{d}t} = -\gamma_0 \mathbf{m} \times \mathbf{H}_\mathrm{eff}, \tag{2.29}$$

where $\gamma_0 = \gamma\mu_0$.

From Eq. 2.29, we can see that the rate of change $\mathrm{d}\mathbf{m}/\mathrm{d}t$ is perpendicular to both $\mathbf{m}$ and $\mathbf{H}_\mathrm{eff}$ which means that the $\mathbf{m}$ precesses around the effective field and the parallel alignment between $\boldsymbol{\mu}$ and $\mathbf{H}_\mathrm{eff}$ is never reached. In reality, this is not true because the macroscopic kinetic and potential energies of motion are transformed to the microscopic thermal motion - heat. Therefore, an additional dissipative damping term must be included. Landau and Lifshitz [78] introduced a phenomenological damping term, so that the dynamics equation now becomes

$$\frac{\mathrm{d}\mathbf{m}}{\mathrm{d}t} = -\gamma_0 \mathbf{m} \times \mathbf{H}_\mathrm{eff} - \lambda \mathbf{m} \times (\mathbf{m} \times \mathbf{H}_\mathrm{eff}), \tag{2.30}$$

where λ is the damping constant and this equation is also called the Landau-Lifshitz (LL) equation. This equation does not describe dynamics well for high values of damping, and because of that, Gilbert [79] introduced a different damping term, so that the equation of magnetisation dynamics becomes

$$\frac{\mathrm{d}\mathbf{m}}{\mathrm{d}t} = -\gamma_0^* \mathbf{m} \times \mathbf{H}_\mathrm{eff} + \alpha \mathbf{m} \times \frac{\mathrm{d}\mathbf{m}}{\mathrm{d}t}, \tag{2.31}$$

where α is the Gilbert damping constant and γ_0^* is the modified gyromagnetic ratio. We refer to the Eq. 2.31 as the Landau-Lifshitz-Gilbert (LLG) equation.

Landau-Lifshitz and Landau-Lifshitz-Gilbert equations are equivalent, and relations between γ_0 and γ_0^*, as well as between λ and α can be established. If the cross product of $\mathbf{m}$ and Eq. 2.31 is taken, we get

$$\mathbf{m} \times \frac{\mathrm{d}\mathbf{m}}{\mathrm{d}t} = -\gamma_0^* \mathbf{m} \times (\mathbf{m} \times \mathbf{H}_{\mathrm{eff}}) + \alpha \mathbf{m} \times \left(\mathbf{m} \times \frac{\mathrm{d}\mathbf{m}}{\mathrm{d}t} \right). \tag{2.32}$$

Using the Grassman identity $\mathbf{a} \times (\mathbf{b} \times \mathbf{c}) = (\mathbf{a} \cdot \mathbf{c})\mathbf{b} - (\mathbf{a} \cdot \mathbf{b})\mathbf{c}$ and knowing that $|\mathbf{m}|^2 = 1$ and $\mathbf{m} \perp \mathrm{d}\mathbf{m}/\mathrm{d}t$, this equation becomes

$$\mathbf{m} \times \frac{\mathrm{d}\mathbf{m}}{\mathrm{d}t} = -\gamma_0^* \mathbf{m} \times (\mathbf{m} \times \mathbf{H}_{\mathrm{eff}}) - \alpha \frac{\mathrm{d}\mathbf{m}}{\mathrm{d}t}, \tag{2.33}$$

Now, $\mathbf{m} \times \frac{\mathrm{d}\mathbf{m}}{\mathrm{d}t}$ can be substituted back to Eq. 2.31, which results in

$$\frac{\mathrm{d}\mathbf{m}}{\mathrm{d}t} = -\frac{\gamma_0^*}{1+\alpha^2} \mathbf{m} \times \mathbf{H}_{\mathrm{eff}} - \frac{\gamma_0^* \alpha}{1+\alpha^2} \mathbf{m} \times (\mathbf{m} \times \mathbf{H}_{\mathrm{eff}}), \tag{2.34}$$

which has the same form as LL equation, given by Eq. 2.30. By comparing the terms in Eq. 2.30 and Eq. 2.34, we get the relations between the constants in LL and LLG equations:

$$\gamma_0 = \frac{\gamma_0^*}{1+\alpha^2} \tag{2.35}$$

$$\lambda = \frac{\gamma_0^* \alpha}{1+\alpha^2}. \tag{2.36}$$

2.3 Magnetic energies

The local magnetic energy density $w = w(\mathbf{r})$ can be calculated as a sum of different energy density contributions

$$w = w_{\mathrm{ex}} + w_{\mathrm{dmi}} + w_{\mathrm{a}} + w_{\mathrm{z}} + w_{\mathrm{d}}, \tag{2.37}$$

where w_{ex} is the symmetric exchange, w_{dmi} is Dzyaloshinskii-Moriya, w_{z} is Zeeman, w_{a} is the magnetocrystalline anisotropy, and w_{d} is the demagnetisation energy density. In this section, we present both discrete and continuous models of these interactions and derive their effective fields. In a continuous micromagnetic framework, using the local energy density $w(\mathbf{r})$, the total energy functional is

$$E[\mathbf{m}] = \int_V w(\mathbf{r}) \, \mathrm{d}^3\mathbf{r}, \tag{2.38}$$

where V is the system's volume. From the system's total energy functional, we compute an effective field $\mathbf{H}_{\text{eff}}$ at point $\mathbf{r}_0$ using Eq. (2.28) as [80]

$$\begin{aligned}\mathbf{H}_{\text{eff}}(\mathbf{r}_0) = \begin{pmatrix} H^x_{\text{eff}}(\mathbf{r}_0) \\ H^y_{\text{eff}}(\mathbf{r}_0) \\ H^z_{\text{eff}}(\mathbf{r}_0) \end{pmatrix} &= -\frac{1}{\mu_0 M_{\text{s}}} \frac{\delta E[\mathbf{m}(\mathbf{r})]}{\delta \mathbf{m}(\mathbf{r}_0)} \\ &= -\frac{1}{\mu_0 M_{\text{s}}} \lim_{\varepsilon \to 0} \frac{1}{\varepsilon} \begin{pmatrix} E[\mathbf{m} + \varepsilon \hat{\mathbf{x}} \delta(\mathbf{r} - \mathbf{r}_0)] - E[\mathbf{m}] \\ E[\mathbf{m} + \varepsilon \hat{\mathbf{y}} \delta(\mathbf{r} - \mathbf{r}_0)] - E[\mathbf{m}] \\ E[\mathbf{m} + \varepsilon \hat{\mathbf{z}} \delta(\mathbf{r} - \mathbf{r}_0)] - E[\mathbf{m}] \end{pmatrix}.\end{aligned} \tag{2.39}$$

We then use the effective field to compute the magnetisation dynamics using Landau-Lifshitz-Gilbert equation.

2.3.1 Symmetric exchange energy

At sufficiently low temperatures, magnetic moments of individual neighbouring atoms order parallel or antiparallel to each other in ferromagnets and antiferromagnets, respectively. This occurs as a consequence of interactions between different magnetic moments at neighbouring crystal lattice sites due to the Coulomb forces and Pauli exclusion principle [68]. Symmetric exchange interaction only orders magnetic moments without selecting a preferred direction, and because of that, this interaction is also called the isotropic exchange interaction. This interaction is well understood from the quantum perspective, but the accurate solution of this interaction in a solid material is very complex. Due to that, some simplified models are used instead. The simplest model, which is still widely used to this day, is the Heisenberg exchange model [81]. According to this model, the exchange energy between two neighbouring spins $\mathbf{S}_i$ and $\mathbf{S}_j$ is

$$E_{\text{ex}} = -J_{ij}\, \mathbf{S}_i \cdot \mathbf{S}_j, \tag{2.40}$$

where J_{ij} is an exchange integral between two spins $\mathbf{S}_i$ and $\mathbf{S}_j$. Detailed derivations of both Eq. 2.40 and the exchange integral J_{ij}, can be found in the relevant literature [8, 72, 81, 9]. The exchange energy is minimal when spins $\mathbf{S}_i$ and $\mathbf{S}_j$ are aligned parallel for $J_{ij} > 0$ (ferromagnets) or antiparallel for $J_{ij} < 0$ (antiferromagnets).

The generalisation of Eq. 2.40 for many-body systems is difficult due to a very complicated evaluation of an exchange integral J. However, in spite of this complexity, the total exchange energy E_{ex} in a crystal can be approximated as a sum of two-electron exchange energies between all spins in the crystal:

$$E_{\text{ex}} = -\sum_{i,j} J_{ij} \mathbf{S}_i \cdot \mathbf{S}_j. \tag{2.41}$$

Exchange interactions are very strong over short ranges and we can assume that every spin $\mathbf{S}_i$ interacts only with the spins at its nearest neighbour lattice sites $\mathbf{S}_{nn}$. Thus, this equation can be rewritten as

$$E_{\text{ex}} = -J \sum_i \mathbf{S}_i \cdot \sum_{nn} \mathbf{S}_{nn}, \tag{2.42}$$

where we assume that the exchange integral value between all nearest neighbours' spins is constant and equals J.

In order to implement this interaction into the micromagnetic framework, a continuous model that ignores the system's atomic structure must be derived. If we assume that all spins in the magnetic system have the same magnitude S, we can use a continuous unit vector field $\mathbf{m}(\mathbf{r}_i) = \mathbf{S}_i/S$ to represent the spins at different lattice sites. Using the continuous vector field, Eq. 2.42 becomes

$$E_{\text{ex}} = -JS^2 \sum_i \mathbf{m}(\mathbf{r}_i) \cdot \sum_{nn} \mathbf{m}(\mathbf{r}_{nn}). \tag{2.43}$$

Now, we assume a simple cubic lattice with lattice constant a where every atom has six nearest neighbours at positions $\mathbf{r}_1 = (a, 0, 0)$, $\mathbf{r}_2 = (-a, 0, 0)$, $\mathbf{r}_3 = (0, a, 0)$, $\mathbf{r}_4 = (0, -a, 0)$, $\mathbf{r}_5 = (0, 0, a)$, and $\mathbf{r}_6 = (0, 0, -a)$. By expanding the continuous $\mathbf{m}(\mathbf{r})$ in the vicinity of $\mathbf{r}_i$, we can compute the sum over six nearest neighbours as

$$\begin{aligned}
\sum_{nn} \mathbf{m}(\mathbf{r}_{nn}) =& \mathbf{m}(\mathbf{r}_i) + \frac{\partial \mathbf{m}(\mathbf{r}_i)}{\partial x} a + \frac{1}{2} \frac{\partial^2 \mathbf{m}(\mathbf{r}_i)}{\partial x^2} a^2 + \mathcal{O}(a^3) \\
&+ \mathbf{m}(\mathbf{r}_i) + \frac{\partial \mathbf{m}(\mathbf{r}_i)}{\partial x} (-a) + \frac{1}{2} \frac{\partial^2 \mathbf{m}(\mathbf{r}_i)}{\partial x^2} (-a)^2 + \mathcal{O}(a^3) \\
&+ \mathbf{m}(\mathbf{r}_i) + \frac{\partial \mathbf{m}(\mathbf{r}_i)}{\partial y} a + \frac{1}{2} \frac{\partial^2 \mathbf{m}(\mathbf{r}_i)}{\partial y^2} a^2 + \mathcal{O}(a^3) \\
&+ \mathbf{m}(\mathbf{r}_i) + \frac{\partial \mathbf{m}(\mathbf{r}_i)}{\partial y} (-a) + \frac{1}{2} \frac{\partial^2 \mathbf{m}(\mathbf{r}_i)}{\partial y^2} (-a)^2 + \mathcal{O}(a^3) \\
&+ \mathbf{m}(\mathbf{r}_i) + \frac{\partial \mathbf{m}(\mathbf{r}_i)}{\partial z} a + \frac{1}{2} \frac{\partial^2 \mathbf{m}(\mathbf{r}_i)}{\partial z^2} a^2 + \mathcal{O}(a^3) \\
&+ \mathbf{m}(\mathbf{r}_i) + \frac{\partial \mathbf{m}(\mathbf{r}_i)}{\partial z} (-a) + \frac{1}{2} \frac{\partial^2 \mathbf{m}(\mathbf{r}_i)}{\partial z^2} (-a)^2 + \mathcal{O}(a^3) \\
=& 6\mathbf{m}(\mathbf{r}_i) + \left[\frac{\partial^2 \mathbf{m}(\mathbf{r}_i)}{\partial x^2} + \frac{\partial^2 \mathbf{m}(\mathbf{r}_i)}{\partial y^2} + \frac{\partial^2 \mathbf{m}(\mathbf{r}_i)}{\partial z^2} \right] a^2 + \mathcal{O}(a^4) \\
=& 6\mathbf{m}(\mathbf{r}_i) + \nabla^2 \mathbf{m}(\mathbf{r}_i) a^2 + \mathcal{O}(a^4),
\end{aligned} \tag{2.44}$$

where ∇^2 is the vector Laplacian operator. If we now insert this sum into Eq. 2.43 and neglect all higher order terms, we get

$$E_{\text{ex}} = -JS^2 \sum_i \mathbf{m}(\mathbf{r}_i) \cdot [6\mathbf{m}(\mathbf{r}_i) + \nabla^2 \mathbf{m}(\mathbf{r}_i) a^2]. \tag{2.45}$$

Since $\mathbf{m}(\mathbf{r}_i) \cdot \mathbf{m}(\mathbf{r}_i) = 1$ and we can always choose the energy reference level so that the constant energy terms can be ignored, this equation becomes

$$E_{\text{ex}} = -JS^2a^2 \sum_i \mathbf{m}(\mathbf{r}_i) \cdot \nabla^2 \mathbf{m}(\mathbf{r}_i). \tag{2.46}$$

In the continuous limit, we replace the sum with an integral, having in mind that the volume d^3r contains $(n/a^3)\mathrm{d}^3r$ atoms, with n being the number of atoms in a unit cell

$$E_{\text{ex}} = -\frac{JS^2n}{a} \int_V \mathbf{m} \cdot \nabla^2 \mathbf{m} \, \mathrm{d}^3r = -A \int_V \mathbf{m} \cdot \nabla^2 \mathbf{m} \, \mathrm{d}^3r, \tag{2.47}$$

where $A = JS^2n/a$ is the exchange energy constant. The exchange energy density is $w_{\text{ex}} = -A\mathbf{m} \cdot \nabla^2 \mathbf{m}$. However, in literature, an equivalent form of the exchange energy density can be found

$$w_{\text{ex}} = A \left[(\nabla m_x)^2 + (\nabla m_y)^2 + (\nabla m_z)^2 \right], \tag{2.48}$$

where m_x, m_y, and m_z are Cartesian components of the magnetisation unit vector $\mathbf{m}$. This form of exchange energy density can be obtained using $\nabla \cdot (\psi \mathbf{A}) = \psi \nabla \cdot \mathbf{A} + \mathbf{A} \cdot \nabla \psi$ identity.

We compute the effective field $\mathbf{H}_{\text{eff}} = (H^x_{\text{eff}}, H^y_{\text{eff}}, H^z_{\text{eff}})^{\mathrm{T}}$ as a consequence of the exchange energy using Eq. 2.39. Consequently, the x component of effective field $\mathbf{H}_{\text{eff}}$ is

$$\begin{aligned}
H^x_{\text{eff}} &= -\frac{1}{\mu_0 M_{\text{s}}} \lim_{\varepsilon \to 0} \frac{1}{\varepsilon} \left(E_{\text{ex}}[\mathbf{m} + \varepsilon \hat{\mathbf{x}} \delta(\mathbf{r} - \mathbf{r}_0)] - E_{\text{ex}}[\mathbf{m}] \right) \\
&= -\frac{A}{\mu_0 M_{\text{s}}} \lim_{\varepsilon \to 0} \frac{1}{\varepsilon} \int \left[\left(\frac{\partial \mathbf{m}}{\partial x} + \varepsilon \hat{\mathbf{x}} \frac{\partial \delta(\mathbf{r} - \mathbf{r}_0)}{\partial x} \right)^2 + \left(\frac{\partial \mathbf{m}}{\partial y} + \varepsilon \hat{\mathbf{x}} \frac{\partial \delta(\mathbf{r} - \mathbf{r}_0)}{\partial y} \right)^2 \right. \\
&\quad \left. + \left(\frac{\partial \mathbf{m}}{\partial z} + \varepsilon \hat{\mathbf{x}} \frac{\partial \delta(\mathbf{r} - \mathbf{r}_0)}{\partial z} \right)^2 - \left(\frac{\partial \mathbf{m}}{\partial x} \right)^2 - \left(\frac{\partial \mathbf{m}}{\partial y} \right)^2 - \left(\frac{\partial \mathbf{m}}{\partial z} \right)^2 \right] \mathrm{d}^3r \\
&= -\frac{2A}{\mu_0 M_{\text{s}}} \hat{\mathbf{x}} \cdot \int \left[\frac{\partial \mathbf{m}}{\partial x} \frac{\partial \delta(\mathbf{r} - \mathbf{r}_0)}{\partial x} + \frac{\partial \mathbf{m}}{\partial y} \frac{\partial \delta(\mathbf{r} - \mathbf{r}_0)}{\partial y} + \frac{\partial \mathbf{m}}{\partial z} \frac{\partial \delta(\mathbf{r} - \mathbf{r}_0)}{\partial z} \right] \mathrm{d}^3r \\
&= -\frac{2A}{\mu_0 M_{\text{s}}} \hat{\mathbf{x}} \cdot \left(-\frac{\partial^2 \mathbf{m}}{\partial x^2} - \frac{\partial^2 \mathbf{m}}{\partial y^2} - \frac{\partial^2 \mathbf{m}}{\partial z^2} \right) = \frac{2A}{\mu_0 M_{\text{s}}} \hat{\mathbf{x}} \cdot \nabla^2 \mathbf{m} \\
&= \frac{2A}{\mu_0 M_{\text{s}}} \nabla^2 m_x
\end{aligned} \tag{2.49}$$

Similarly, y and z components of the effective field are

$$\begin{aligned} H_{\text{eff}}^{y} =& -\frac{1}{\mu_0 M_{\text{s}}} \lim_{\varepsilon \to 0} \frac{1}{\varepsilon} \left(E_{\text{ex}}[\mathbf{m} + \varepsilon \hat{\mathbf{y}} \delta(\mathbf{r} - \mathbf{r}_0)] - E_{\text{ex}}[\mathbf{m}] \right) \\ =& -\frac{2A}{\mu_0 M_{\text{s}}} \hat{\mathbf{y}} \cdot \int \left[\frac{\partial \mathbf{m}}{\partial x} \frac{\partial \delta(\mathbf{r} - \mathbf{r}_0)}{\partial x} + \frac{\partial \mathbf{m}}{\partial y} \frac{\partial \delta(\mathbf{r} - \mathbf{r}_0)}{\partial y} + \frac{\partial \mathbf{m}}{\partial z} \frac{\partial \delta(\mathbf{r} - \mathbf{r}_0)}{\partial z} \right] \mathrm{d}^3 r \\ =& -\frac{2A}{\mu_0 M_{\text{s}}} \hat{\mathbf{y}} \cdot \left(-\frac{\partial^2 \mathbf{m}}{\partial x^2} - \frac{\partial^2 \mathbf{m}}{\partial y^2} - \frac{\partial^2 \mathbf{m}}{\partial z^2} \right) == \frac{2A}{\mu_0 M_{\text{s}}} \hat{\mathbf{y}} \cdot \nabla^2 \mathbf{m} \\ =& \frac{2A}{\mu_0 M_{\text{s}}} \nabla^2 m_y \end{aligned} \tag{2.50}$$

$$\begin{aligned} H_{\text{eff}}^{z} =& -\frac{1}{\mu_0 M_{\text{s}}} \lim_{\varepsilon \to 0} \frac{1}{\varepsilon} \left(E_{\text{ex}}[\mathbf{m} + \varepsilon \hat{\mathbf{z}} \delta(\mathbf{r} - \mathbf{r}_0)] - E_{\text{ex}}[\mathbf{m}] \right) \\ =& -\frac{2A}{\mu_0 M_{\text{s}}} \hat{\mathbf{z}} \cdot \int \left[\frac{\partial \mathbf{m}}{\partial x} \frac{\partial \delta(\mathbf{r} - \mathbf{r}_0)}{\partial x} + \frac{\partial \mathbf{m}}{\partial y} \frac{\partial \delta(\mathbf{r} - \mathbf{r}_0)}{\partial y} + \frac{\partial \mathbf{m}}{\partial z} \frac{\partial \delta(\mathbf{r} - \mathbf{r}_0)}{\partial z} \right] \mathrm{d}^3 r \\ =& -\frac{2A}{\mu_0 M_{\text{s}}} \hat{\mathbf{z}} \cdot \left(-\frac{\partial^2 \mathbf{m}}{\partial x^2} - \frac{\partial^2 \mathbf{m}}{\partial y^2} - \frac{\partial^2 \mathbf{m}}{\partial z^2} \right) == \frac{2A}{\mu_0 M_{\text{s}}} \hat{\mathbf{z}} \cdot \nabla^2 \mathbf{m} \\ =& \frac{2A}{\mu_0 M_{\text{s}}} \nabla^2 m_z \end{aligned} \tag{2.51}$$

After we calculated all three components of the effective field, the total effective field is

$$\mathbf{H}_{\text{eff}} = \frac{2A}{\mu_0 M_{\text{s}}} \begin{pmatrix} \nabla^2 m_x \\ \nabla^2 m_y \\ \nabla^2 m_z \end{pmatrix} = \frac{2A}{\mu_0 M_{\text{s}}} \nabla^2 \mathbf{m}. \tag{2.52}$$

2.3.2 Dzyaloshinskii-Moriya energy

In magnetic systems that lack some type of inversion symmetry, chiral interactions may occur. Chiral interactions occur either in materials with noncentrosymmetric crystal structure [2, 3, 4] (helimagnets) or at interfaces between different materials [6, 7, 11, 13, 82, 5] which inherently lack inversion symmetry. This phenomenon was firstly introduced by Dzyaloshinskii [2] who analysed the crystal structure symmetry and later Moriya [3, 4] managed to explain chiral interactions as an extension of superexchange theory to include the spin-orbit coupling effect. In recognition of their achievement, this interaction is now called the Dzyaloshinskii-Moriya Interaction (DMI).

The Dzyaloshinskii-Moriya energy between two spins $\mathbf{S}_i$ and $\mathbf{S}_j$ is [3, 5]

$$E_{\text{dmi}} = \mathbf{d}_{ij} \cdot (\mathbf{S}_i \times \mathbf{S}_j), \tag{2.53}$$

where $\mathbf{d}_{ij}$ is the Dzyaloshinskii vector. The Dzyaloshinskii-Moriya energy is minimal when neighbouring spins $\mathbf{S}_i$ and $\mathbf{S}_j$ are perpendicular to each other in the plane perpendicular to the Dzyaloshinskii vector $\mathbf{d}_{ij}$.

We can write an expression of the total DMI energy as a sum of energies between all individual spins:

$$E_{\text{dmi}} = \frac{1}{2} \sum_{i,j} \mathbf{d}_{ij} \cdot (\mathbf{S}_i \times \mathbf{S}_j) \,, \tag{2.54}$$

where we add 1/2 factor in order to avoid the double counting in the sum. Similar to the case of exchange energy, DMI energy is very strong over short ranges and it can be assumed that every spin $\mathbf{S}_i$ interacts only with spins at its nearest neighbour lattice sites. Accordingly, we compute the DMI energy as

$$E_{\text{dmi}} = \frac{1}{2} \sum_{i} \sum_{nn} \mathbf{d}_{i,nn} \cdot (\mathbf{S}_i \times \mathbf{S}_{nn}) \,. \tag{2.55}$$

Now, we derive a continuous expression suitable for the implementation in a micromagnetic framework. In helimagnetic materials, which are considered in this study, we can write the Dzyaloshinskii vector between two neighbouring spins $\mathbf{S}_i$ and $\mathbf{S}_{nn}$ as $\mathbf{d}_{ij} = d\hat{\mathbf{r}}_{ij}$ [83], where $\hat{\mathbf{r}}_{ij}$ is a unit vector pointing from spin $\mathbf{S}_i$ to $\mathbf{S}_j$. Also, if we use a continuous unit vector field $\mathbf{m}(\mathbf{r}_i) = \mathbf{S}_i/S$ to represent the spins at different lattice sites, Eq. 2.55 becomes

$$E_{\text{dmi}} = \frac{dS^2}{2} \sum_{i} \sum_{nn} \mathbf{r}_{i,nn} \cdot [\mathbf{m}(\mathbf{r}_i) \times \mathbf{m}(\mathbf{r}_j)] \,. \tag{2.56}$$

At this point, we assume a simple cubic lattice with lattice constant a where every atom has six nearest neighbours at positions $\mathbf{r}_1 = (a, 0, 0)$, $\mathbf{r}_2 = (-a, 0, 0)$, $\mathbf{r}_3 = (0, a, 0)$, $\mathbf{r}_4 = (0, -a, 0)$, $\mathbf{r}_5 = (0, 0, a)$, and $\mathbf{r}_6 = (0, 0, -a)$. By expanding the continuous $\mathbf{m}(\mathbf{r})$ in the vicinity of the spin at lattice site $\mathbf{r}_i$ in Taylor series, we can compute the sum over

nearest neighbours as

$$
\begin{aligned}
&\sum_{nn} \mathbf{r}_{i,nn} \cdot [\mathbf{m}(\mathbf{r}_i) \times \mathbf{m}(\mathbf{r}_j)] = \\
&\qquad \hat{\mathbf{x}} \cdot \left\{ \mathbf{m}(\mathbf{r}_i) \times \left[\mathbf{m}(\mathbf{r}_i) + \frac{\partial \mathbf{m}(\mathbf{r}_i)}{\partial x} a + \frac{1}{2} \frac{\partial^2 \mathbf{m}(\mathbf{r}_i)}{\partial x^2} a^2 + \mathcal{O}(a^3) \right] \right\} \\
&\qquad + (-\hat{\mathbf{x}}) \cdot \left\{ \mathbf{m}(\mathbf{r}_i) \times \left[\mathbf{m}(\mathbf{r}_i) + \frac{\partial \mathbf{m}(\mathbf{r}_i)}{\partial x} (-a) + \frac{1}{2} \frac{\partial^2 \mathbf{m}(\mathbf{r}_i)}{\partial x^2} (-a)^2 + \mathcal{O}(a^3) \right] \right\} \\
&\qquad + \hat{\mathbf{y}} \cdot \left\{ \mathbf{m}(\mathbf{r}_i) \times \left[\mathbf{m}(\mathbf{r}_i) + \frac{\partial \mathbf{m}(\mathbf{r}_i)}{\partial y} a + \frac{1}{2} \frac{\partial^2 \mathbf{m}(\mathbf{r}_i)}{\partial y^2} a^2 + \mathcal{O}(a^3) \right] \right\} \\
&\qquad + (-\hat{\mathbf{y}}) \cdot \left\{ \mathbf{m}(\mathbf{r}_i) \times \left[\mathbf{m}(\mathbf{r}_i) + \frac{\partial \mathbf{m}(\mathbf{r}_i)}{\partial y} (-a) + \frac{1}{2} \frac{\partial^2 \mathbf{m}(\mathbf{r}_i)}{\partial y^2} (-a)^2 + \mathcal{O}(a^3) \right] \right\} \\
&\qquad + \hat{\mathbf{z}} \cdot \left\{ \mathbf{m}(\mathbf{r}_i) \times \left[\mathbf{m}(\mathbf{r}_i) + \frac{\partial \mathbf{m}(\mathbf{r}_i)}{\partial z} a + \frac{1}{2} \frac{\partial^2 \mathbf{m}(\mathbf{r}_i)}{\partial z^2} a^2 + \mathcal{O}(a^3) \right] \right\} \\
&\qquad + (-\hat{\mathbf{z}}) \cdot \left\{ \mathbf{m}(\mathbf{r}_i) \times \left[\mathbf{m}(\mathbf{r}_i) + \frac{\partial \mathbf{m}(\mathbf{r}_i)}{\partial z} (-a) + \frac{1}{2} \frac{\partial^2 \mathbf{m}(\mathbf{r}_i)}{\partial z^2} (-a)^2 + \mathcal{O}(a^3) \right] \right\} \\
&= 2a\hat{\mathbf{x}} \cdot \left[\mathbf{m}(\mathbf{r}_i) \times \frac{\partial \mathbf{m}(\mathbf{r}_i)}{\partial x} \right] + 2a\hat{\mathbf{y}} \cdot \left[\mathbf{m}(\mathbf{r}_i) \times \frac{\partial \mathbf{m}(\mathbf{r}_i)}{\partial y} \right] + 2a\hat{\mathbf{z}} \cdot \left[\mathbf{m}(\mathbf{r}_i) \times \frac{\partial \mathbf{m}(\mathbf{r}_i)}{\partial z} \right] + \mathcal{O}(a^3) \\
&= 2a \left[m_x \left(\frac{\partial m_y}{\partial z} - \frac{\partial m_z}{\partial y} \right) + m_y \left(\frac{\partial m_z}{\partial x} - \frac{\partial m_x}{\partial z} \right) + m_z \left(\frac{\partial m_x}{\partial y} - \frac{\partial m_y}{\partial x} \right) \right] + \mathcal{O}(a^3) \\
&= -2a\mathbf{m}(\mathbf{r}_i) \cdot (\nabla \times \mathbf{m}(\mathbf{r}_i)) + \mathcal{O}(a^3)
\end{aligned}
\tag{2.57}
$$

Now, we can substitute the sum into Eq. 2.56 and ignore all higher order terms and get

$$E_{\mathrm{dmi}} = -adS^2 \sum_i \mathbf{m}(\mathbf{r}_i) \cdot (\nabla \times \mathbf{m}(\mathbf{r}_i)). \tag{2.58}$$

In the continuous limit, we can replace the sum with an integral, knowing that the volume $\mathrm{d}^3 r$ contains $(n/a^3)\mathrm{d}^3 r$ atoms, where n is the number of atoms in a unit cell:

$$E_{\mathrm{dmi}} = -\frac{dS^2 n}{a^2} \int \mathbf{m} \cdot (\nabla \times \mathbf{m}) \, \mathrm{d}^3 r = D \int \mathbf{m} \cdot (\nabla \times \mathbf{m}) \, \mathrm{d}^3 r, \tag{2.59}$$

where $D = -dS^2 n/a^2$ is the Dzyaloshinskii-Moriya energy constant.

We compute the effective field $\mathbf{H}_{\mathrm{eff}} = (H^x_{\mathrm{eff}}, H^y_{\mathrm{eff}}, H^z_{\mathrm{eff}})^{\mathrm{T}}$ as a consequence of the DMI energy using Eq. 2.39. Accordingly, the x component of effective field $\mathbf{H}_{\mathrm{eff}}$ is

$$
\begin{aligned}
H^x_{\mathrm{eff}} &= -\frac{1}{\mu_0 M_{\mathrm{s}}} \lim_{\varepsilon \to 0} \frac{1}{\varepsilon} \left(E_{\mathrm{dmi}}[\mathbf{m} + \varepsilon \hat{\mathbf{x}} \delta(\mathbf{r} - \mathbf{r}_0)] - E_{\mathrm{dmi}}[\mathbf{m}] \right) \\
&= -\frac{D}{\mu_0 M_{\mathrm{s}}} \int \left[\frac{\partial m_z}{\partial y} \delta(\mathbf{r} - \mathbf{r}_0) - \frac{\partial m_y}{\partial z} \delta(\mathbf{r} - \mathbf{r}_0) + m_y \frac{\partial \delta(\mathbf{r} - \mathbf{r}_0)}{\partial z} - m_z \frac{\partial \delta(\mathbf{r} - \mathbf{r}_0)}{\partial y} \right] \mathrm{d}^3 r \\
&= -\frac{2D}{\mu_0 M_{\mathrm{s}}} \left(\frac{\partial m_z}{\partial y} - \frac{\partial m_y}{\partial z} \right)
\end{aligned}
\tag{2.60}
$$

Similarly, the other two components of the effective field are

$$\begin{aligned} H_{\text{eff}}^{y} &= -\frac{1}{\mu_0 M_{\text{s}}} \lim_{\varepsilon \to 0} \frac{1}{\varepsilon} \left(E_{\text{dmi}}[\mathbf{m} + \varepsilon \hat{\mathbf{y}} \delta(\mathbf{r} - \mathbf{r}_0)] - E_{\text{dmi}}[\mathbf{m}] \right) \\ &= -\frac{D}{\mu_0 M_{\text{s}}} \int \left[\frac{\partial m_x}{\partial z} \delta(\mathbf{r} - \mathbf{r}_0) - \frac{\partial m_z}{\partial x} \delta(\mathbf{r} - \mathbf{r}_0) + m_z \frac{\partial \delta(\mathbf{r} - \mathbf{r}_0)}{\partial x} - m_x \frac{\partial \delta(\mathbf{r} - \mathbf{r}_0)}{\partial z} \right] \mathrm{d}^3 r \\ &= -\frac{2D}{\mu_0 M_{\text{s}}} \left(\frac{\partial m_x}{\partial z} - \frac{\partial m_z}{\partial x} \right) \end{aligned} \tag{2.61}$$

$$\begin{aligned} H_{\text{eff}}^{z} &= -\frac{1}{\mu_0 M_{\text{s}}} \lim_{\varepsilon \to 0} \frac{1}{\varepsilon} \left(E_{\text{dmi}}[\mathbf{m} + \varepsilon \hat{\mathbf{z}} \delta(\mathbf{r} - \mathbf{r}_0)] - E_{\text{dmi}}[\mathbf{m}] \right) \\ &= -\frac{D}{\mu_0 M_{\text{s}}} \int \left[\frac{\partial m_y}{\partial x} \delta(\mathbf{r} - \mathbf{r}_0) - \frac{\partial m_x}{\partial y} \delta(\mathbf{r} - \mathbf{r}_0) + m_x \frac{\partial \delta(\mathbf{r} - \mathbf{r}_0)}{\partial y} - m_y \frac{\partial \delta(\mathbf{r} - \mathbf{r}_0)}{\partial x} \right] \mathrm{d}^3 r \\ &= -\frac{2D}{\mu_0 M_{\text{s}}} \left(\frac{\partial m_y}{\partial x} - \frac{\partial m_x}{\partial y} \right) \end{aligned} \tag{2.62}$$

Finally, the effective field as a consequence of the DMI energy is

$$\mathbf{H}_{\text{eff}} = -\frac{2D}{\mu_0 M_{\text{s}}} \begin{pmatrix} \frac{\partial m_z}{\partial y} - \frac{\partial m_y}{\partial z} \\ \frac{\partial m_x}{\partial z} - \frac{\partial m_z}{\partial x} \\ \frac{\partial m_y}{\partial x} - \frac{\partial m_x}{\partial y} \end{pmatrix} = -\frac{2D}{\mu_0 M_{\text{s}}} \nabla \times \mathbf{m}. \tag{2.63}$$

2.3.3 Uniaxial anisotropy energy

In real magnetic materials, the magnetisation $\mathbf{m}$ tends to be aligned along certain directions depending on the material's crystal structure. The electron's orbitals depend on the crystal electric field of the surrounding crystal order. Due to this electric field, via spin-orbit interactions, the magnetic moments tend to align along some preferential directions. If there is only one preferential direction, this type of anisotropy is called the uniaxial anisotropy. The local anisotropy energy density of a single spin $\mathbf{S}_i$ is [9]

$$E_{\text{a}} = -k(\mathbf{S}_i \cdot \hat{\mathbf{u}})^2 = -k \cos^2(\theta), \tag{2.64}$$

where k is the anisotropy constant, $\hat{\mathbf{u}}$ is the unit vector along the preferential anisotropy axis, and theta is the angle between $\mathbf{S}_i$ and $\hat{\mathbf{u}}$. From this expression, it can be seen that the anisotropy energy is minimal if $\theta = 0$ or $\theta = \pi$. The uniaxial anisotropy expression, given by Eq. (2.64), can also contain higher order terms, but they can be usually neglected.

We can compute the total uniaxial anisotropy energy as

$$E_{\text{a}} = -k \sum_i (\mathbf{S}_i \cdot \hat{\mathbf{u}})^2. \tag{2.65}$$

If we introduce a continuous unit vector field $\mathbf{m}(\mathbf{r}_i) = \mathbf{S}_i/S$, this expression becomes

$$E_\mathrm{a} = -kS^2 \sum_i (\mathbf{m}(\mathbf{r}_i) \cdot \hat{\mathbf{u}})^2. \tag{2.66}$$

In the continuous limit, a sum can be replaced by an integral, so that the continuous form of uniaxial anisotropy is

$$E_\mathrm{a} = -\frac{kS^2 n}{a^3} \int_V (\mathbf{m} \cdot \hat{\mathbf{u}})^2 \, \mathrm{d}^3 r = -K \int_V (\mathbf{m} \cdot \hat{\mathbf{u}})^2 \, \mathrm{d}^3 r, \tag{2.67}$$

because $\mathrm{d}^3 r$ volume contains $(n/a^3)\mathrm{d}^3 r$ atoms, where $K = kS^2 n/a^3$ is the uniaxial anisotropy constant, with n being the number of atoms in the unit cell.

We derive the uniaxial anisotropy effective field $\mathbf{H}_\mathrm{eff} = (H^x_\mathrm{eff}, H^y_\mathrm{eff}, H^z_\mathrm{eff})^\mathrm{T}$ using Eq. 2.39. Accordingly, the x component of effective field $\mathbf{H}_\mathrm{eff}$ is

$$\begin{aligned} H^x_\mathrm{eff} &= -\frac{1}{\mu_0 M_\mathrm{s}} \lim_{\varepsilon \to 0} \frac{1}{\varepsilon} \left(E_\mathrm{a}[\mathbf{m} + \varepsilon \hat{\mathbf{x}} \delta(\mathbf{r} - \mathbf{r}_0)] - E_\mathrm{a}[\mathbf{m}] \right) \\ &= \frac{K}{\mu_0 M_\mathrm{s}} \lim_{\varepsilon \to 0} \frac{1}{\varepsilon} \int \left[(\mathbf{m} \cdot \hat{\mathbf{u}} + \varepsilon \hat{\mathbf{x}} \delta(\mathbf{r} - \mathbf{r}_0) \cdot \hat{\mathbf{u}})^2 - (\mathbf{m} \cdot \hat{\mathbf{u}})^2 \right] \mathrm{d}^3 r \\ &= \frac{2K}{\mu_0 M_\mathrm{s}} m_x u_x \end{aligned} \tag{2.68}$$

Similarly, the other two components of the uniaxial anisotropy effective field are

$$\begin{aligned} H^y_\mathrm{eff} &= -\frac{1}{\mu_0 M_\mathrm{s}} \lim_{\varepsilon \to 0} \frac{1}{\varepsilon} \left(E_\mathrm{a}[\mathbf{m} + \varepsilon \hat{\mathbf{y}} \delta(\mathbf{r} - \mathbf{r}_0)] - E_\mathrm{a}[\mathbf{m}] \right) \\ &= \frac{K}{\mu_0 M_\mathrm{s}} \lim_{\varepsilon \to 0} \frac{1}{\varepsilon} \int \left[(\mathbf{m} \cdot \hat{\mathbf{u}} + \varepsilon \hat{\mathbf{y}} \delta(\mathbf{r} - \mathbf{r}_0) \cdot \hat{\mathbf{u}})^2 - (\mathbf{m} \cdot \hat{\mathbf{u}})^2 \right] \mathrm{d}^3 r \\ &= \frac{2K}{\mu_0 M_\mathrm{s}} m_y u_y \end{aligned} \tag{2.69}$$

and

$$\begin{aligned} H^z_\mathrm{eff} &= -\frac{1}{\mu_0 M_\mathrm{s}} \lim_{\varepsilon \to 0} \frac{1}{\varepsilon} \left(E_\mathrm{a}[\mathbf{m} + \varepsilon \hat{\mathbf{z}} \delta(\mathbf{r} - \mathbf{r}_0)] - E_\mathrm{a}[\mathbf{m}] \right) \\ &= \frac{K}{\mu_0 M_\mathrm{s}} \lim_{\varepsilon \to 0} \frac{1}{\varepsilon} \int \left[(\mathbf{m} \cdot \hat{\mathbf{u}} + \varepsilon \hat{\mathbf{z}} \delta(\mathbf{r} - \mathbf{r}_0) \cdot \hat{\mathbf{u}})^2 - (\mathbf{m} \cdot \hat{\mathbf{u}})^2 \right] \mathrm{d}^3 r \\ &= \frac{2K}{\mu_0 M_\mathrm{s}} m_z u_z. \end{aligned} \tag{2.70}$$

Finally, the uniaxial anisotropy effective field is

$$\mathbf{H}_\mathrm{eff} = \frac{2K}{\mu_0 M_\mathrm{s}} \begin{pmatrix} m_x u_x \\ m_y u_y \\ m_z u_z \end{pmatrix} = \frac{2K}{\mu_0 M_\mathrm{s}} \mathbf{m} \cdot \hat{\mathbf{u}}. \tag{2.71}$$

In helimagnetic materials, the magnetocrystalline anisotropy is very weak in comparison to other energy terms and it is usually neglected.

2.3.4 Zeeman energy

When a single magnetic moment $\boldsymbol{\mu}$ is placed into an external magnetic field $\mathbf{B}$, its Zeeman energy is [8, 61]

$$E_{\mathrm{z}} = -\boldsymbol{\mu}_i \cdot \mathbf{B}. \tag{2.72}$$

Zeeman energy tends to align the magnetic moment in the same direction as the external magnetic field. Now, if the magnetic moment is replaced by a normalised magnetisation vector field $\mathbf{m}(\mathbf{r}_i)/\mu$, the total Zeeman energy is

$$E_{\mathrm{z}} = -\mu_0 \mu \sum_i \mathbf{m}(\mathbf{r}_i) \cdot \mathbf{H}, \tag{2.73}$$

since $\mathbf{B} = \mu_0 \mathbf{H}$. In the continuous limit we replace the sum with an integral and the total Zeeman energy is

$$E_{\mathrm{z}} = -\frac{\mu_0 \mu n}{a^3} \int_V \mathbf{m} \cdot \mathbf{H} \, \mathrm{d}^3 r = -\mu_0 M_{\mathrm{s}} \int_V \mathbf{m} \cdot \mathbf{H} \, \mathrm{d}^3 r, \tag{2.74}$$

because $\mathrm{d}^3 r$ volume contains $(n/a^3)\mathrm{d}^3 r$ atoms, with n being the number of atoms in a unit cell. If Eq. 2.27 is applied on a unit cell volume we get $M_{\mathrm{s}} = \mu n/a^3$. It is obvious that, the effective field associated to the Zeeman energy is

$$\mathbf{H}_{\mathrm{eff}} = \begin{pmatrix} H_{\mathrm{eff}}^x \\ H_{\mathrm{eff}}^y \\ H_{\mathrm{eff}}^z \end{pmatrix} = \mathbf{H}. \tag{2.75}$$

2.3.5 Demagnetisation energy

A magnetic field $\mathbf{B}(\mathbf{r}_j)$ at position $\mathbf{r}_j$ of a single magnetic moment (magnetic dipole) $\boldsymbol{\mu}_j$ can be computed using [61]

$$\mathbf{B}_j = \frac{\mu_0}{4\pi} \left[\frac{3\hat{\mathbf{n}}_j (\hat{\mathbf{n}}_j \cdot \boldsymbol{\mu}_j) - \boldsymbol{\mu}_j}{|\mathbf{r}_j^3|} \right] \tag{2.76}$$

where $\hat{\mathbf{n}}_j = \mathbf{r}_j/|\mathbf{r}_j|$. In magnetic samples, every magnetic moment "feels" the magnetic field of all surrounding magnetic moments and, therefore, the total magnetic field on a single magnetic moment $\mathbf{B}(\mathbf{r}_i)$ can be written as a sum of individual fields $\mathbf{B}(\mathbf{r}_j)$:

$$\mathbf{B}(\mathbf{r}_i) = \frac{\mu_0}{4\pi} \sum_{j \neq i} \left[\frac{3\hat{\mathbf{n}}_{ji} (\hat{\mathbf{n}}_{ji} \cdot \boldsymbol{\mu}_j) - \boldsymbol{\mu}_j}{|\mathbf{r}_{ji}^3|} \right]. \tag{2.77}$$

Consequently, the energy of a magnetic moment $\boldsymbol{\mu}_i$ due its interaction with magnetic field of all surrounding magnetic moments is

$$E_{\mathrm{d}} = -\boldsymbol{\mu}_i \cdot \mathbf{B}(\mathbf{r}_i) = -\frac{\mu_0}{4\pi}\boldsymbol{\mu}_i \cdot \sum_{j \neq i} \left[\frac{3\hat{\mathbf{n}}_{ji}(\hat{\mathbf{n}}_{ji} \cdot \boldsymbol{\mu}_j) - \boldsymbol{\mu}_j}{|\mathbf{r}_{ji}^3|} \right]. \tag{2.78}$$

Since this energy occurs as a consequence of mutual interaction of magnetic moments (dipoles), it is also called the dipolar interaction energy. The total demagnetisation energy E_{d} in a magnetic sample we can compute by summing Eq. 2.78 over all magnetic moments in the sample as

$$E_{\mathrm{d}} = -\frac{\mu_0}{4\pi}\sum_i \boldsymbol{\mu}_i \cdot \sum_{j \neq i} \left[\frac{3\hat{\mathbf{n}}_{ji}(\hat{\mathbf{n}}_{ji} \cdot \boldsymbol{\mu}_j) - \boldsymbol{\mu}_j}{|\mathbf{r}_{ji}^3|} \right]. \tag{2.79}$$

In order to compute the dipolar interaction energy in a continuous magnetic sample, ignoring the material's atomistic structure, a continuous equation must be derived. The Ampere's law in differential form is [61]

$$\nabla \times \mathbf{H} = \mathbf{J} + \epsilon_0 \frac{\partial \mathbf{E}}{\partial t}, \tag{2.80}$$

where $\mathbf{J}$ is the current density and $\mathbf{E}$ is the electric field. In the case when no current exists $\mathbf{J} = 0$ and in the absence of time changing electric field $\partial\mathbf{E}/\partial t = 0$, the Ampere's law becomes

$$\nabla \times \mathbf{H} = 0, \tag{2.81}$$

meaning that the magnetic field $\mathbf{H}$ is conservative. Knowing that, the magnetic field can be computed from the magnetic scalar potential Φ_{M} as

$$\mathbf{H} = -\nabla\Phi_{\mathrm{M}}. \tag{2.82}$$

Furthermore, since $\mathbf{B} = \mu_0(\mathbf{H} + \mathbf{M})$ and magnetic flux density has no conservative component ($\nabla \cdot \mathbf{B} = 0$), we can write

$$\nabla \cdot \mathbf{H} = -\nabla \cdot \mathbf{M} = \nabla^2\Phi_{\mathrm{M}}. \tag{2.83}$$

The magnetic scalar potential $\Phi_{\mathrm{M}}(\mathbf{r})$ at position $\mathbf{r}$ we compute using

$$\Phi_{\mathrm{M}}(\mathbf{r}) = \frac{1}{4\pi}\int_V \frac{1}{|\mathbf{r} - \mathbf{r}'|}\left(-\nabla \cdot \mathbf{M}(\mathbf{r})\right)\,\mathrm{d}^3r' + \frac{1}{4\pi}\int_A \frac{1}{|\mathbf{r} - \mathbf{r}'|}\mathbf{M}(\mathbf{r}) \cdot \mathrm{d}\mathbf{A}', \tag{2.84}$$

where $\mathrm{d}\mathbf{A}' = \mathrm{d}A'\mathbf{n}(\mathbf{r})$, with $\mathbf{n}(\mathbf{r})$ being the vector normal to the plane containing the element $\mathrm{d}A'$. The first term is a solution to the Poisson equation, whereas the second term takes into account the boundary conditions.

Finally, knowing the magnetic scalar potential, the effective field due to the demagnetisation energy is

$$\mathbf{H}_{\text{eff}} = \mathbf{H}_{\text{d}} = -\nabla\Phi_{\text{M}}, \tag{2.85}$$

and the total demagnetisation energy of a magnetic sample we can compute using

$$E_{\text{d}} = \frac{1}{2}\mu_0 M_{\text{s}} \int \mathbf{m} \cdot (\nabla\Phi_{\text{M}})\, \text{d}^3 r. \tag{2.86}$$

The factor 1/2 occurs in order to avoid "double counting".

2.4 Numerical method

The main unknown in micromagnetics is the magnetisation vector field $\mathbf{m} = \mathbf{M}/M_{\text{s}}$, where $\mathbf{M}$ is the magnetisation and M_{s} is the saturation magnetisation as it was described in previous sections. So far, the magnetisation vector field $\mathbf{m}$ was a continuous function of both space and time $\mathbf{m} = \mathbf{m}(\mathbf{r}, t)$. However, there is a very limited number of cases where $\mathbf{m}$ can be solved analytically. In most cases, micromagnetic model must be solved numerically.

Because computers are discrete machines with limited amount of operating memory, before the magnetisation vector $\mathbf{m}$ is numerically computed, the magnetisation field must be discretised. There are two main methods of discretising continuous functions into a discrete set of values: finite difference and finite elements. In this section, we present the basics of finite difference and finite element discretisations, time integration, micromagnetic software algorithm, and the micromagnetic simulation software implementation.

2.4.1 Finite difference method

In the finite difference method, the continuous field is discretised so that the three-dimensional domain, where continuous function is defined, is divided into cuboids. More precisely, the domain becomes an aggregate of cuboids. If the domain on which field is defined is one-dimensional it is divided into line segments, whereas two-dimensional domains are divided into rectangles. After that, it is assumed that the field value is constant in each domain cuboid cell. The advantage of this method is that apart from being very intuitive, it is also easy to implement and numerically solve. However, this method has some serious disadvantages. First of all, cuboid aggregates can accurately represent only the cuboid domain geometry. Usually, this is not the case and different irregular domain shapes cannot be appropriately discretised. This introduces artefacts and eventually error in the numerically computed solution. Secondly, because the finite difference discretisation is always cuboidal, if we need to discretise a sphere, we would have to discretise the cuboid which contains the sphere we are interested in, and set

the values of the discretised field outside the sphere to be zero. This wastes memory and computation time increases. Last but not least, the regularity of finite difference mesh introduces anisotropy to the micromagnetic system which would could affect the solution [84, 85].

2.4.2 Finite element method

An alternative to the finite difference method is the finite element method. In this method, the domain where a continuous field is defined is discretised into an aggregate of simplices (finite elements). In the three-dimensional case, a simplex is of the tetrahedron shape with four vertices (nodes). This way, in the case of irregular shapes, nodes (vertices) are placed at the domain boundaries, which are then connected with line segments. This approximates the simulated domain better than the finite difference method. However, the main disadvantage of this method is that in addition to being much less intuitive than the finite difference method, its numerical solution and implementation is not trivial.

The first step in this method is to define a finite element mesh, which can be done using various software packages – one of them is Gmsh [86]. Examples of three-dimensional finite element meshes are shown in Fig. 2.2 for 5 nm thin film disk and square samples, respectively. The discretisation is chosen so that the maximum spacing between two neighbouring mesh nodes is less than 3 nm. Similar meshes are going to be used in later chapters.

After the domain is discretised into finite elements (simplices), a set of basis function is defined on that mesh. There are many different types of basis functions which can be used for discretising continuous fields, but in this work we will use linear piecewise basis functions (first-order polynomials). Because the discretised vector magnetisation field $\mathbf{m}(\mathbf{r})$ consists of three scalar fields $m^c(\mathbf{r})$, where $c = x, y, z$, each component in one mesh simplex (tetrahedron) can be approximated as

$$m^c(\mathbf{r}) = \sum_{i=1}^{4} m_i^c \psi_i(\mathbf{r}), \tag{2.87}$$

where $4 = \dim + 1$ is the number of vertices associated to a single tetrahedron, with dim being the simplex dimension, m_i^c is the field component value at vertex i, and $\psi_i(\mathbf{r})$ is a basis function (shape function) associated to the node i [87].

Basis function $\psi_i(\mathbf{r})$ is defined so that its value is 1 at the node i and zero at all other nodes. Consequently,

$$\psi_i(\mathbf{r}_j) = \delta_{ij} \tag{2.88}$$

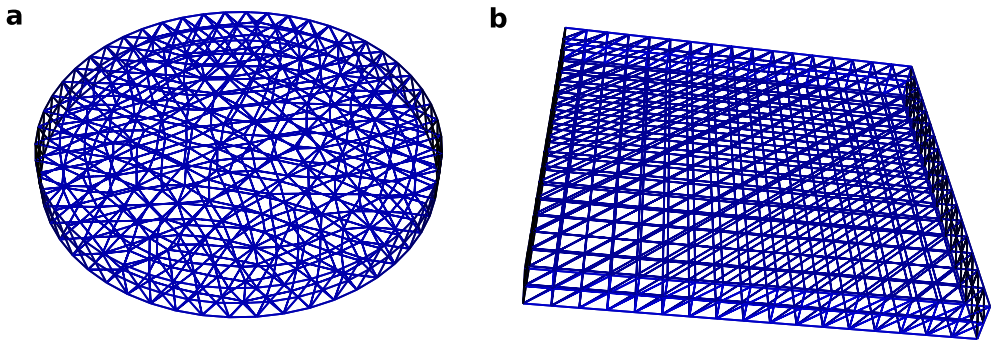

Figure 2.2: (**a**) A three-dimensional finite elements mesh of a 5 nm thin film disk sample with diameter $d = 50$ nm. (**a**) A finite elements mesh of a 5 nm thin film square sample with edge length $d = 50$ nm. The discretisation is chosen so that the maximum spacing between two neighbouring mesh nodes is smaller that 3 nm.

where δ_{ij} is the Kronecker delta function. Also all basis functions in a single simplex must be normalised so that

$$\sum_{i=1}^{4} \psi_i(\mathbf{r}) = 1. \tag{2.89}$$

In the case of linear (first-order) approximation, a basis function associated to vertex i is defined as

$$\psi_i(\mathbf{r}) = a_i + b_i x + c_i y + d_i z, \tag{2.90}$$

where x, y, and z are components of position vector $\mathbf{r}$ [87, 88]. The values of coefficients a_i, b_i, c_i, and d_i for the node $i = 1$ are

$$a_1 = \frac{1}{6V_s}\begin{vmatrix} x_2 & y_2 & z_2 \\ x_3 & y_3 & z_3 \\ x_4 & y_4 & z_4 \end{vmatrix} \tag{2.91}$$

$$b_1 = -\frac{1}{6V_s}\begin{vmatrix} 1 & y_2 & z_2 \\ 1 & y_3 & z_3 \\ 1 & y_4 & z_4 \end{vmatrix} \tag{2.92}$$

$$c_1 = -\frac{1}{6V_s}\begin{vmatrix} x_2 & 1 & z_2 \\ x_3 & 1 & z_3 \\ x_4 & 1 & z_4 \end{vmatrix} \tag{2.93}$$

$$d_1 = -\frac{1}{6V_s}\begin{vmatrix} x_2 & y_2 & 1 \\ x_3 & y_3 & 1 \\ x_4 & y_4 & 1 \end{vmatrix} \tag{2.94}$$

where V_s is the simplex (finite element) volume [87] and can be computed as

$$V_s = \frac{1}{6}\begin{vmatrix} 1 & x_1 & y_1 & z_1 \\ 1 & x_2 & y_2 & z_2 \\ 1 & x_3 & y_3 & z_3 \\ 1 & x_4 & y_4 & z_4 \end{vmatrix}. \tag{2.95}$$

The coefficients associated to other simplex nodes 2, 3, and 4 can be computed using previous expressions with cyclic permutation.

Using these basis functions, a continuous field can be discretised and uniquely described with a set of discrete field values at nodes i. In the finite element discretisation, all operations on fields can be written as operations on individual basis functions. Accordingly, the spatial differentiation of a single magnetisation component at point $\mathbf{r}$ which is contained in simplex becomes [87]

$$\frac{\partial m^c(\mathbf{r})}{\partial x} = \sum_{i=1}^{4} m_i^c \frac{\partial \psi_i(\mathbf{r})}{\partial x}, \tag{2.96}$$

$$\frac{\partial m^c(\mathbf{r})}{\partial y} = \sum_{i=1}^{4} m_i^c \frac{\partial \psi_i(\mathbf{r})}{\partial y}, \tag{2.97}$$

$$\frac{\partial m^c(\mathbf{r})}{\partial z} = \sum_{i=1}^{4} m_i^c \frac{\partial \psi_i(\mathbf{r})}{\partial z}. \tag{2.98}$$

or

$$\nabla m^c(\mathbf{r}) = \sum_{i=1}^{4} m_i^c \nabla \psi_i(\mathbf{r}). \tag{2.99}$$

Similarly, the integration of discretised field over the entire domain discretised is

$$\int_V m^c(\mathbf{r})\,\mathrm{d}V = \sum_{n=1}^{N}\sum_{i=1}^{4} m_i^{c,n} \int_V \psi_i^n(\mathbf{r})\,\mathrm{d}V, \tag{2.100}$$

where N is the number of simplices [88].

By performing these basic operations on discretised magnetisation field components, an effective field $\mathbf{H}_{\text{eff}}$ can be computed. Basis functions can be also defined using higher order polynomials which would increase the accuracy of the approximation. However, this would increase the number of coefficients which must be computed which further affects the computation time.

In this work, all low-level finite element operations are performed using FEniCS package [89].

2.4.3 Time integration

In micromagnetics, the magnetisation dynamics is governed by the Landau-Lifshitz-Gilbert (LLG) equation, which in its explicit form is

$$\frac{\mathrm{d}\mathbf{m}}{\mathrm{d}t} = -\frac{\gamma_0^*}{1+\alpha^2}\mathbf{m}\times\mathbf{H}_{\text{eff}} - \frac{\gamma_0^*\alpha}{1+\alpha^2}\mathbf{m}\times(\mathbf{m}\times\mathbf{H}_{\text{eff}}) = f(\mathbf{m},\mathbf{H}_{\text{eff}}(\mathbf{m})), \tag{2.101}$$

and was derived in previous sections. For a magnetisation configuration $\mathbf{m}$, which is discretised using finite elements, an effective field $\mathbf{H}_{\text{eff}}$ can be computed by performing operations on basis functions. Using that value, the rate of change of magnetisation $\mathrm{d}\mathbf{m}/\mathrm{d}t$ is computed using the LLG equation. Knowing this, time integration can be performed in order to compute the magnetisation at the next time step.

The simplest method for computing the magnetisation field at the next time step is the Euler method. The magnetisation field at time $t_n + \Delta t$ can be expanded in Taylor series in the vicinity of time t_n

$$\mathbf{m}(\mathbf{r}, t_n+\Delta t) = \mathbf{m}(\mathbf{r}, t_n) + \Delta t\frac{\mathrm{d}\mathbf{m}(\mathbf{r}, t_n)}{\mathrm{d}t} + \frac{1}{2}(\Delta t)^2\frac{\mathrm{d}^2\mathbf{m}(\mathbf{r}, t_n)}{\mathrm{d}t^2} + \mathcal{O}(\Delta t^3). \tag{2.102}$$

If we neglect the second-order terms and higher, the magnetisation at time $t_n + \Delta t$ is

$$\mathbf{m}(\mathbf{r}, t_n+\Delta t) \approx \mathbf{m}(\mathbf{r}, t_n) + \Delta t\frac{\mathrm{d}\mathbf{m}(\mathbf{r}, t_n)}{\mathrm{d}t}, \tag{2.103}$$

where $\mathrm{d}\mathbf{m}(\mathbf{r}, t_n)/\mathrm{d}t$ is computed using the LLG equation. This is the Euler method.

The Euler method is the first order method because it ignores all terms of the second order and higher. Consequently, the error is of the $(\Delta t)^2$ order. This means that using two times smaller time step reduces the error four times. However, this leads to the increased computation time. Consequently, an appropriate trade-off between accuracy and computation time must be made.

If we want to increase the order of error associated to the time integration, we must include higher order terms to the integration algorithm. Again, if we start from the Taylor expansion:

$$\mathbf{m}(\mathbf{r}, t_n+\Delta t) = \mathbf{m}(\mathbf{r}, t_n) + \Delta t\frac{\mathrm{d}\mathbf{m}(\mathbf{r}, t_n)}{\mathrm{d}t} + \frac{1}{2}(\Delta t)^2\frac{\mathrm{d}^2\mathbf{m}(\mathbf{r}, t_n)}{\mathrm{d}t^2} + \mathcal{O}(\Delta t^3). \tag{2.104}$$

and neglect terms of the third order and higher, we obtain:

$$\mathbf{m}(\mathbf{r}, t_n+\Delta t) \approx \mathbf{m}(\mathbf{r}, t_n) + \Delta t\frac{\mathrm{d}\mathbf{m}(\mathbf{r}, t_n)}{\mathrm{d}t} + \frac{1}{2}(\Delta t)^2\frac{\mathrm{d}^2\mathbf{m}(\mathbf{r}, t_n)}{\mathrm{d}t^2}. \tag{2.105}$$

Now, if we want to compute the magnetisation field at time $t_n + \Delta t$, we have to know both the first and second order derivatives of the magnetisation field $\mathbf{m}(\mathbf{r})$. The first order we know how to compute by using the LLG equation. However, we do not know

how to compute the second order derivative. We can approximate the second order derivative as a forward difference

$$\frac{\mathrm{d}^2\mathbf{m}(\mathbf{r},t_n)}{\mathrm{d}t^2} = \frac{2}{\Delta t}\left[\frac{\mathrm{d}\mathbf{m}(\mathbf{r},t_n+\Delta t/2)}{\mathrm{d}t} - \frac{\mathrm{d}\mathbf{m}(\mathbf{r},t_n)}{\mathrm{d}t}\right]. \tag{2.106}$$

If we substitute the second order derivative, we get

$$\mathbf{m}(\mathbf{r},t_n+\Delta t) \approx \mathbf{m}(\mathbf{r},t_n) + \Delta t\frac{\mathrm{d}\mathbf{m}(\mathbf{r},t_n+\Delta t/2)}{\mathrm{d}t}. \tag{2.107}$$

However, now instead of computing one time step, we have to perform two time step computations. More precisely:

1. At time step t_n with magnetisation configuration $\mathbf{m}(\mathbf{r},t_n)$, we compute the effective field $\mathbf{H}_{\text{eff}}$.

2. We compute the magnetisation configuration at $t_n+\Delta t/2$ by performing an Euler step
$$\mathbf{m}(\mathbf{r},t_n+\Delta t/2) = \mathbf{m}(\mathbf{r},t_n) + \frac{\Delta t}{2}\frac{\mathrm{d}\mathbf{m}(\mathbf{r},t_n)}{\mathrm{d}t} \tag{2.108}$$

3. After we computed the magnetisation configuration $\mathbf{m}(\mathbf{r},t_n+\Delta t/2)$, we again compute the effective field $\mathbf{H}_{\text{eff}}$ and the right hand side of LLG equation.

4. Finally, we perform an Euler step using this time derivative, but this time for the entire time step:
$$\mathbf{m}(\mathbf{r},t_n+\Delta t) = \mathbf{m}(\mathbf{r},t_n) + \Delta t\frac{\mathrm{d}\mathbf{m}(\mathbf{r},t_n+\Delta t/2)}{\mathrm{d}t}. \tag{2.109}$$

Using this method, the error is of the third order $(\Delta t)^3$. However, in order to progress time for Δt, we have to compute the effective field and the right hand side of the LLG equation twice as well as to compute an Euler step two times.

In all previously described time integration algorithms, a constant time step Δt is assumed for the entire time evolution. However, in reality, we cannot predict how the magnetisation field is going to evolve and whether the used time step is appropriate at any time not to introduce an unacceptable error. This problem can be solved by choosing a small time step for time integration. However, in the case of slowly changing magnetisation this would introduce unjustified number of computation steps which would further increase the total simulation time. Because of that, an adaptive time step algorithms can be used. Now, we briefly describe the background of adaptive time step integration.

If we perform the first order Euler time integration, as we previously showed, the error is of the second order and can be computed as

$$\Delta \mathbf{m}^{err} \approx \frac{1}{2}(\Delta t)^2 \frac{\mathrm{d}^2 \mathbf{m}(\mathbf{r}, t_n)}{\mathrm{d}t^2}. \tag{2.110}$$

Using forward difference, the second order magnetisation derivative can be approximated and the error at time step n can be defined as

$$\varepsilon_n = \frac{1}{2}\Delta t \left\| \frac{\mathrm{d}\mathbf{m}(\mathbf{r}, t_n + \Delta t)}{\mathrm{d}t} - \frac{\mathrm{d}\mathbf{m}(\mathbf{r}, t_n)}{\mathrm{d}t} \right\|. \tag{2.111}$$

Now we can specify two different errors. The first one is the absolute error ε_A and we require that the error at any time step is smaller than the defined absolute error $\varepsilon < \varepsilon_\mathrm{A}$. The second one is the relative error using which we introduce a condition

$$\varepsilon_n < \varepsilon_\mathrm{R} \left\| \frac{\mathrm{d}\mathbf{m}(\mathbf{r}, t_n + \Delta t)}{\mathrm{d}t} - \frac{\mathrm{d}\mathbf{m}(\mathbf{r}, t_n)}{\mathrm{d}t} \right\|. \tag{2.112}$$

By evaluating these conditions, we can determine at each time step whether our time step Δt is too large. If it is too large, we decrease Δt and eventually increase the total number of time steps [90].

In this work, we perform an adaptive time step integration using Sundials (CVODE) software package [91, 92].

2.4.4 Simulation algorithm

In this subsection we summarise the algorithm that is used to compute the magnetisation time evolution. Before we perform the time integration, we initialise the system with an initial magnetisation configuration $\mathbf{m}_0$. This is the magnetisation configuration at time t_0. This magnetisation configuration (vector field) is discretised using finite elements, so that each magnetisation component is discretised into N discrete values which are defined at mesh vertices (nodes). By performing differentiation operations on finite element basis functions, we can compute the effective field $\mathbf{H}_\mathrm{eff}$ for the energies present in the system. Using the effective field values at all finite element mesh vertices, together with magnetisation configuration values, we can compute the magnetisation time derivative using LLG equation. Now, we progress the time as it was previously explained. This procedure is iterated until the final time is reached or until the system is fully relaxed. We assume the system is relaxed when the torque which is exerted on magnetisation $\mathbf{H}_\mathrm{eff} \times \mathbf{m}$ at all mesh nodes is below the specified minimum value. In addition, if the minimum torque tolerance is too small, zero torque could never be reached because of the unavoidable numerical noise. In that case, we compute the total energy of the system and when the energy increases (as a consequence of numerical noise) more than the specified number of times, we stop the time integration.

2.4.5 Simulation software

We implemented the presented model in the finite element method framework and developed a micromagnetic simulation tool Finmag[1] (successor of Nmag [93]). For the low-level finite element operations, we use the FEniCS project [89] and for the adaptive step time integration we use Sundials/CVODE solver [91, 92]. For visualisation, we use Matplotlib [94] and ParaView [95].

2.5 Summary

In this chapter, basic concepts of magnetism in condensed matter were presented. After introducing the magnetic moment, the equation governing its dynamics was derived. Magnetic energies (symmetric exchange, Dzyaloshinskii-Moriya, uniaxial anisotropy, Zeeman, and demagnetisation) were presented in both their discrete and continuous forms, and their effective fields were derived. Furthermore, basic concepts of discretising continuous fields (finite difference and finite element methods) were introduced as well as the basics of time integration. Finally, we summarise the simulation algorithm and provide some details of the micromagnetic code implementation.

[1] Finmag is a simulation tool developed at the University of Southampton as a joint work by Marc-Antonio Bisotti, Dmitri Chernyshenko, Marijan Beg, Weiwei Wang, David Cortẽs-Ortuño, Maximilian Albert, Rebecca Carey, Mark Vousden, and Hans Fangohr.

Chapter 3

Stability

Magnetic skyrmions have the potential to provide solutions for low-power, high-density data storage and processing. One of the major challenges in developing skyrmion-based devices is the skyrmions' magnetic stability in confined helimagnetic nanostructures. Through a systematic study of equilibrium states, using a full three-dimensional micromagnetic model including demagnetisation effects, we demonstrate that skyrmionic states are the lowest energy states in helimagnetic thin film nanostructures at zero external magnetic field and in the absence of magnetocrystalline anisotropy. We also report the regions of metastability for non-ground state equilibrium configurations. This is in contrast to the infinitely large helimagnetic thin film samples, where skyrmions must be stabilised with an external magnetic field, and because of that, we explore what might be the possible stabilisation mechanism in confined helimagnetic nanostructures. In particular, we study the effects of the demagnetisation energy contribution as well as the magnetisation variation in the out-of-film direction. We find that if the demagnetisation energy is neglected or the translational variance of magnetisation is not present, the isolated skyrmion state is metastable, but not the ground state at zero external magnetic field. Also, we examine the robustness of skyrmionic states and show that they are able to adapt their size in order to accommodate the hosting nanostructure, which is a necessary requirement for their possible technological use. Finally, we report whether our findings remain valid in the case of a helimagnetic material with ordering temperature above room temperature, which is required for the implementation of skyrmion-based devices.

3.1 Methods

3.1.1 Micromagnetic model

We use an energy model consistent with a non-centrosymmetric cubic B20 ($P2_13$ space group) crystal structure. This is appropriate for a range of isostructural compounds and pseudo-binary alloys in which skyrmionic states have been experimentally observed [23, 30, 31, 32, 33, 96, 97]. The magnetic free energy of the system E contains several contributions and can be written in the form:

$$E = \int \left[w_{\text{ex}} + w_{\text{dmi}} + w_{\text{z}} + w_{\text{d}} + w_{\text{a}} \right] \mathrm{d}^3 r. \tag{3.1}$$

The first term $w_{\text{ex}} = A \left[(\nabla m_x)^2 + (\nabla m_y)^2 + (\nabla m_z)^2 \right]$ is the symmetric exchange energy density with exchange stiffness material parameter A, where m_x, m_y, and m_z are the Cartesian components of the vector $\mathbf{m} = \mathbf{M}/M_{\text{s}}$ that describes the magnetisation $\mathbf{M}$, with $M_{\text{s}} = |\mathbf{M}|$ being the saturation magnetisation. The second term is the Dzyaloshinskii-Moriya Interaction (DMI) energy density $w_{\text{dmi}} = D\mathbf{m}\cdot(\nabla \times \mathbf{m})$, obtained by constructing the allowed Lifshitz invariants for the crystallographic class T [10, 27], where D is the material parameter. The third term is the Zeeman energy density term $w_{\text{z}} = -\mu_0 \mathbf{H} \cdot \mathbf{M}$ which defines the coupling of magnetisation to an external magnetic field $\mathbf{H}$. The w_{d} term represents the demagnetisation (magnetostatic) energy density. The last term w_{a} is the magnetocrystalline anisotropy energy density, and because the simulated material is assumed to be isotropic, we neglect it throughout this work. Neglecting this term also allows us to determine whether magnetocrystalline anisotropy is necessary to stabilise skyrmionic states in confined helimagnetic nanostructures.

The Landau-Lifshitz-Gilbert (LLG) equation [79, 78]:

$$\frac{\partial \mathbf{m}}{\partial t} = -\gamma_0^* \mathbf{m} \times \mathbf{H}_{\text{eff}} + \alpha \mathbf{m} \times \frac{\partial \mathbf{m}}{\partial t}, \tag{3.2}$$

governs the magnetisation dynamics, where $\gamma_0^* = \gamma_0(1+\alpha^2)$, with $\gamma_0 = 2.21\times10^5\,\mathrm{m\,A^{-1}s^{-1}}$ and $\alpha \geq 0$ being the gyromagnetic ratio and Gilbert damping, respectively. We compute the effective magnetic field using

$$\mathbf{H}_{\text{eff}} = -\frac{1}{\mu_0 M_{\text{s}}} \frac{\delta E[\mathbf{m}]}{\delta \mathbf{m}}, \tag{3.3}$$

where $E[\mathbf{m}]$ is the total energy functional given by Eq. (3.1). With this model, we solve for magnetic configurations $\mathbf{m}$ using the condition of minimum torque arrived by integrating a set of dissipative, time-dependent equations. The boundary conditions are validated by a series of simulations reproducing the results reported by Rohart and Thiaville [41].

3.1.2 Material parameters

We estimate the material parameters in our simulations to represent the cubic B20 FeGe helimagnet with four Fe and four Ge atoms per unit cell [98] and crystal lattice constant $a = 4.7\,\text{Å}$ [99]. The local magnetic moments of iron and germanium atoms are $1.16\mu_\text{B}$ and $-0.086\mu_\text{B}$ [100], respectively, where μ_B is the Bohr magneton constant. Accordingly, we estimate the saturation magnetisation as $M_\text{s} = 4N(1.16 - 0.086)\mu_\text{B} = 384\,\text{kA}\,\text{m}^{-1}$, with $N = a^{-3}$ being the number of lattice unit cells in a cubic metre. The spin-wave stiffness is $D_\text{sw} = a^2 T_\text{C}$ [101], where the FeGe ordering temperature is $T_\text{C} = 278.7\,\text{K}$ [102]. Consequently, the exchange stiffness parameter value is $A = D_\text{sw} M_\text{s}/(2g\mu_\text{B}) = 8.78\,\text{pJ}\,\text{m}^{-1}$ [103], where $g \approx 2$ is the Landé g-factor. The estimated DMI material parameter D from the long-range FeGe helical period $L_\text{D} = 70\,\text{nm}$ [102], using $L_\text{D} = 4\pi A/|D|$ [96], is $|D| = 1.58\,\text{mJ}\,\text{m}^{-2}$.

3.1.3 Skyrmion number S and injective scalar value S_a

In order to support the discussion of skyrmionic states, the topological skyrmion number [19]

$$S^\text{2D} = \frac{1}{4\pi} \int \mathbf{m} \cdot \left(\frac{\partial \mathbf{m}}{\partial x} \times \frac{\partial \mathbf{m}}{\partial y} \right) \text{d}^2 r, \tag{3.4}$$

can be computed for two-dimensional samples hosting the magnetisation configuration. However, for confined systems, the skyrmion number S^2D is not quantised into integers [39, 44], and therefore, a more suitable name for S^2D may be the "scalar spin chirality" (and consequently the expression under an integral would be called the "spin chirality density"), but we will follow the existing literature [39, 44] and refer to S^2D as the skyrmion number. It will be shown subsequently in Sec. 3.2 that the skyrmion number in confined geometries is not an injective function since it does not preserve distinctness (one-to-one mapping between skyrmionic states and skyrmion number value S^2D). Therefore, for two-dimensional samples, we define a different scalar value

$$S_\text{a}^\text{2D} = \frac{1}{4\pi} \int \left| \mathbf{m} \cdot \left(\frac{\partial \mathbf{m}}{\partial x} \times \frac{\partial \mathbf{m}}{\partial y} \right) \right| \text{d}^2 r. \tag{3.5}$$

This scalar value is injective and provides necessary distinctness between S_a^{2D} values for different skyrmionic states as discussed in Sec. 3.2. In terms of the terminology discussion above regarding S^2D, the entity S_a^{2D} describes the "scalar absolute spin chirality". We also emphasise that although the skyrmion number S^2D has a clear mathematical [104] and physical [105] interpretation, we define the artificial injective scalar value S_a only to support the classification and discussion of different skyrmionic states observed in this work.

Skyrmion number S^{2D} and artificially defined scalar value S_a^{2D}, given by Eq. (3.4) and Eq. (3.5), respectively, are valid only for the two-dimensional samples hosting the magnetisation configuration. However, in this work, we study three-dimensional samples and, because of that, we now define a new set of expressions taking into account the third dimension. The skyrmion number in three-dimensional samples S^{3D} we compute using

$$S^{3D} = \frac{1}{8\pi} \int \mathbf{m} \cdot \left(\frac{\partial \mathbf{m}}{\partial x} \times \frac{\partial \mathbf{m}}{\partial y} \right) \mathrm{d}^3 r, \tag{3.6}$$

as suggested by Lee et al. [106], which results in a value proportional to the anomalous Hall conductivity. Similar to the two-dimensional case, we also define the artificial injective scalar value S_a^{3D} for three-dimensional samples as

$$S_a^{3D} = \frac{1}{8\pi} \int \left| \mathbf{m} \cdot \left(\frac{\partial \mathbf{m}}{\partial x} \times \frac{\partial \mathbf{m}}{\partial y} \right) \right| \mathrm{d}^3 r. \tag{3.7}$$

In order to allow the S_a^{3D} value to fall within the two-dimensional skyrmionic states classification scheme, we normalise the computed S_a^{3D} value by a constant ($t/2$, where t is the sample thickness).

For simplicity, in this work, we refer to both two-dimensional and three-dimensional skyrmion number and scalar value expressions as S and S_a because it is always clear what expression has been used according to the dimensionality of the sample.

3.2 Initial magnetisation configurations

The magnetisation configurations that we use as initial states in the micromagnetic simulations are shown in Fig. 3.1. We vary the disk sample diameter d and external magnetic field H, and for every point in the d–H parameter space, we relax twelve different initial magnetisation configurations. These are the five skyrmionic configurations (A, B, C, D, and E), three helical configurations (H2, H3, and H4), the uniform configuration (U), and three random magnetisation configurations (R).

Now, we introduce an approximate analytic model[1] that helps us generate a range of physically meaningful and reproducible initial skyrmionic magnetisation configurations labelled A-E in Fig. 3.1. The used DMI energy density term $w_{\mathrm{dmi}} = D\mathbf{m} \cdot (\nabla \times \mathbf{m})$ is consistent with the helimagnetic material of crystallographic class T, and one expects a skyrmionic state configuration with no radial spin component (chiral skyrmion) to emerge [29]. Consequently, if we consider a two-dimensional disk sample of radius R in the plane containing the x and y axes, as shown in Fig. 3.2 (b) inset, an approximation of the chiral skyrmionic magnetisation configuration (for $D > 0$), in cylindrical coordinates

[1] A zero-torque analytic model was initially proposed and derived by Robert L. Stamps (University of Glasgow).

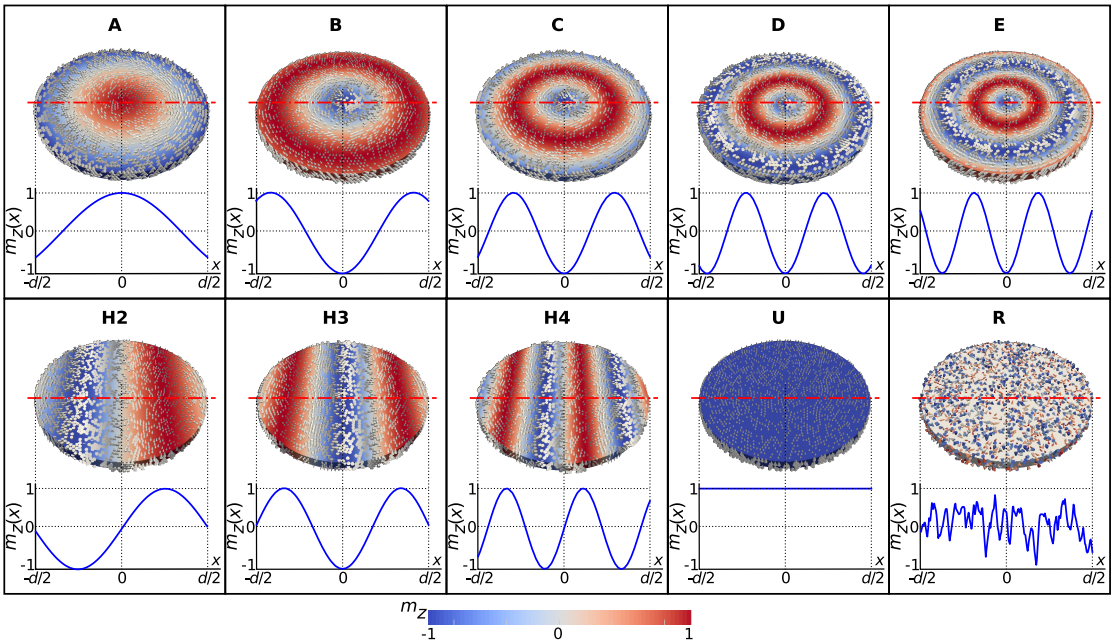

Figure 3.1: The magnetisation configurations relaxed using the full three-dimensional micromagnetic simulations. The configurations labelled A-E correspond to the first five solutions of the approximate analytic model, whereas the three helical states with 2, 3, and 4 helical half-periods are labelled as H2, H3, and H4, respectively. The uniform out-of-plane magnetisation state is labelled as U, and an example of random magnetisation state is marked with R.

(ρ, φ, z), is

$$\begin{aligned} m_\rho &= 0, \\ m_\varphi &= \sin(k\rho), \\ m_z &= -\cos(k\rho), \end{aligned} \tag{3.8}$$

where $k = 2\pi/s$ is a measure of the skyrmionic state size s.

An equilibrium configuration requires that the torque exerted on the magnetisation $\mathbf{m}$ vanishes at every point in sample ($\mathbf{m} \times \mathbf{H}_{\text{eff}} = 0$), including the boundary. The effective field functional $\mathbf{H}_{\text{eff}} = -(\delta E[\mathbf{m}]/\delta \mathbf{m})/(\mu_0 M_\text{s})$, due to only symmetric exchange and DMI energy contributions, in absence of an external magnetic field, as we have shown in Chapter 2, is

$$\mathbf{H}_{\text{eff}} = \frac{2}{\mu_0 M_\text{s}} \left[A\nabla^2 \mathbf{m} - D\left(\nabla \times \mathbf{m}\right) \right], \tag{3.9}$$

for any magnetisation configuration. Computing this expression for the radially symmetric approximate skyrmionic state model $\mathbf{m} = \sin(k\rho)\hat{\boldsymbol{\varphi}} - \cos(k\rho)\hat{\mathbf{z}}$ results in

$$\begin{aligned} \mathbf{H}_{\text{eff}} = &\frac{2}{\mu_0 M_\text{s}} \left[\left(Dk - Ak^2 - \frac{A}{\rho^2} \right) \sin(k\rho) + \frac{Ak}{\rho} \cos(k\rho) \right] \hat{\boldsymbol{\varphi}} + \\ &\frac{2}{\mu_0 M_\text{s}} \left[\left(\frac{Ak}{\rho} - \frac{D}{\rho} \right) \sin(k\rho) + \left(Ak^2 - Dk \right) \cos(k\rho) \right] \hat{\mathbf{z}}. \end{aligned} \tag{3.10}$$

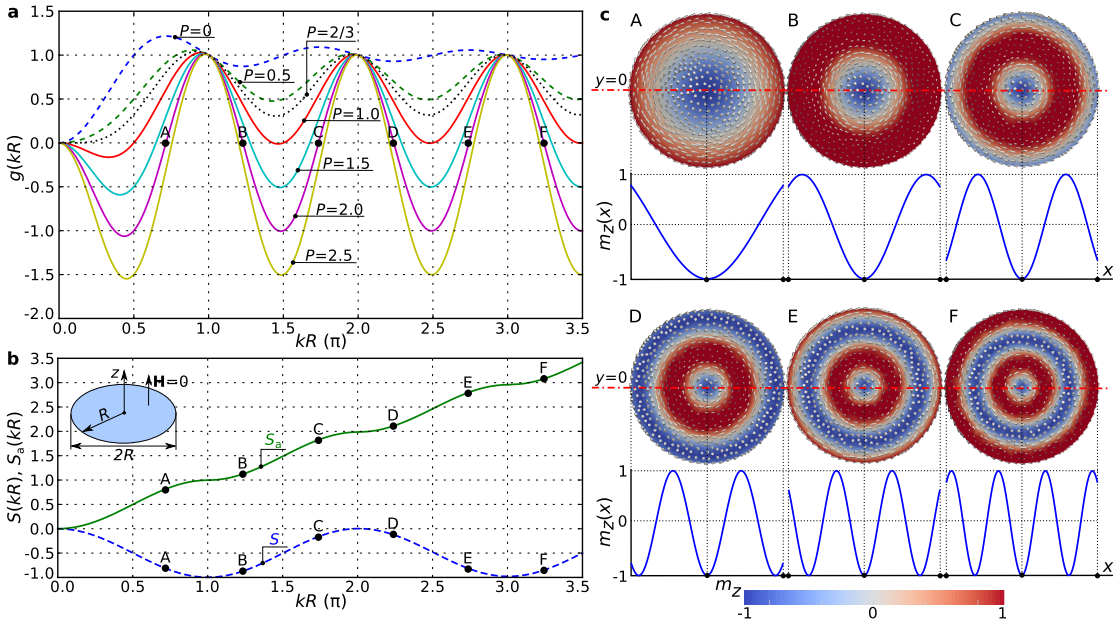

Figure 3.2: (**a**) The zero-torque condition $g(kR)$ plots, given by Eq. (3.12), for different values of $P = D/kA$. All zero-torque conditions for P smaller than the boundary case $P = 2/3$ (dotted line) have no solutions, whereas for $P > 2/3$, multiple solutions (A-F) exist. (**b**) The non-injective dependence of skyrmion number S and the injective dependence of scalar value S_a on kR. (**c**) The magnetisation configurations and the out-of-plane magnetisation component $m_z(x)$ along the horizontal symmetry line for different solutions (A-F) of Eq. (3.12) for $P = 2$.

Consequently, the torque exerted on the magnetisation $\mathbf{m}$ is

$$\mathbf{m} \times \mathbf{H}_\mathrm{eff} = \frac{2}{\mu_0 M_\mathrm{s}} \left[\frac{Ak}{\rho} - \frac{D}{\rho} \sin^2(k\rho) - \frac{A}{2\rho^2} \sin(2k\rho) \right] \hat{\mathbf{r}}. \tag{3.11}$$

Requiring the torque to vanish at the disk boundary $\rho = R$ results in the zero-torque condition:

$$g(kR) \equiv -P \sin^2(kR) - \frac{\sin(2kR)}{2kR} + 1 = 0, \tag{3.12}$$

where $P = D/kA$. The analysis of this condition shows that the parameter P must satisfy the inequality $P > 2/3$ in order for $g(kR)$ to have roots and, thus, a skyrmionic state core to exist in at least metastable equilibrium. In Fig. 3.2 (a), we plot the zero-torque condition as a function of kR for different values of P. Since $P = 2/3$ is the boundary case (dotted line in the plot), all plots for $P < 2/3$ have no solutions, whereas the zero-torque condition has multiple solutions if $P > 2/3$.

We show the skyrmionic magnetisation configurations, used as initial states in the energy minimisation process, corresponding to the zero-torque condition solutions (marked A-F) for $P = 2$, in Fig. 3.2 (c). In order to support the discussion of these magnetisation configurations, we compute the skyrmion number S, which for our approximate analytic model results in $S = (\cos(kR) - 1)/2$. Its dependence on kR, presented in Fig. 3.2 (b)

as a dashed line, shows that the skyrmion number for the skyrmionic states in confined nanostructures is not an injective function since it does not preserve distinctness (one-to-one mapping between kR and skyrmion number value S). Therefore, a different scalar value S_a is computed and from its dependence on kR, shown in Fig. 3.2 (b) as a solid line, we conclude that this scalar value is injective and provides necessary distinctness between S_a values for different skyrmionic states.

For the helical state, which emerges as a consequence of the Dzyaloshinskii-Moriya interaction considered in this work, we expect that the magnetisation vector at any point is perpendicular to the helical propagation direction (Bloch-wall-like configuration). Consequently, if both x and y axis are in the plane of the thin-film sample and the x axis is chosen as a propagation direction, the helical magnetisation configuration in Cartesian coordinates is

$$\begin{aligned} m_x &= 0, \\ m_y &= \cos(k_\mathrm{h} x), \\ m_z &= \sin(k_\mathrm{h} x), \end{aligned} \tag{3.13}$$

where $k_\mathrm{h} = 2\pi/L_\mathrm{D}$, with L_D being the helical period [10].

Now, we investigate whether the helical period L_D in confined nanostructures is independent on the sample diameter, and if not, what are the helical period values that can occur in our simulated system. After relaxing helical configurations and varying both the helical period and disk sample diameter (up to 180 nm), we find that all relax to a limited set of helical states with different helical periods. More precisely, the observed relaxed helical states consist of either 2, 3, or 4 helical half-periods along the disk sample diameter, including the characteristic magnetisation tilting at the boundary [41]. Thus, we define three different helical magnetisation configurations as initial states with helical periods $2d/2$, $2d/3$, or $2d/4$, where d is the disk sample diameter, and are named H2, H3, and H4, respectively. Magnetisation configurations of these states, together with their $m_z(x)$ profiles along the horizontal symmetry, are shown in Fig. 3.1.

In addition to the previously defined eight chiral initial states, we also use the uniform magnetisation configuration, where the magnetisation at all mesh nodes is in the positive out-of-plane z direction, as shown in Fig. 3.1 marked as U. Finally, in order to capture other equilibrium states that cannot be obtained by relaxing previously described well-defined magnetisation configurations, we also use additional three random magnetisation configurations. At every mesh node, we choose three random numbers in the $[-1, 1]$ range for three magnetisation components and then normalise them in order to fulfil the $|\mathbf{m}| = 1$ micromagnetic condition. An example of one random magnetisation configuration is shown in Fig. 3.1 and labelled as R.

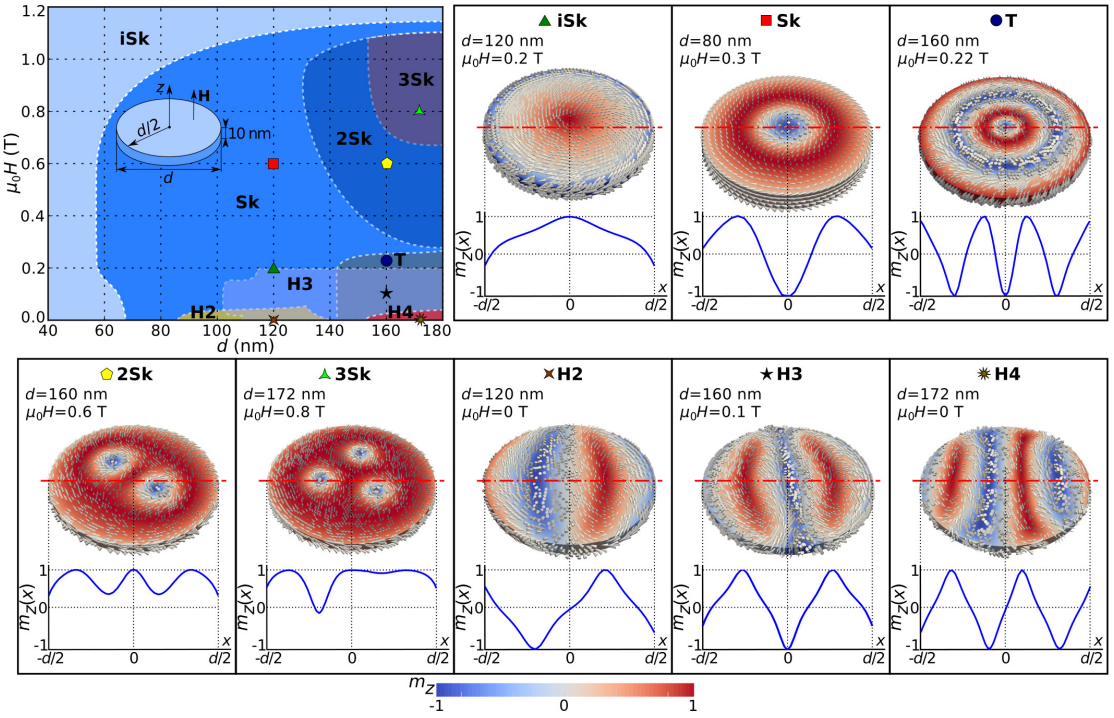

Figure 3.3: The phase diagram with overlapping regions where different states are in an equilibrium together with magnetisation configurations and out-of-plane magnetisation component $m_z(x)$ along the horizontal symmetry line corresponding to different regions in the phase diagram.

3.3 Equilibrium states

In order to identify the lowest energy magnetisation state in confined helimagnetic nanostructures, firstly, all equilibrium magnetisation states (local energy minima) must be identified, and secondly, their energies compared. In this section, we focus on the first step – identifying the equilibrium magnetisation states. We compute them by solving a full three-dimensional model using a finite element based micromagnetic simulator. In particular, we simulate a thin film helimagnetic FeGe disk nanostructure with thickness $t = 10\,\text{nm}$ and diameter d, as shown in Fig. 3.3 inset. The relevant lengthscales in the simulated system are: exchange length $l_{\text{ex}} = \sqrt{2A/\mu_0 M_{\text{s}}^2} = 9.73\,\text{nm}$ and helical length $L_{\text{D}} = 4\pi A/D = 70\,\text{nm}$. Consequently, we choose the finite element mesh discretisation so that the maximum spacing between two neighbouring mesh nodes is below $l_{\text{max}} = 3\,\text{nm}$. We apply a uniform external magnetic field perpendicular to the thin film sample, i.e. in the positive z direction.

In this section, we determine what magnetisation configurations emerge as the equilibrium states at different d–H parameter space points. In order to do that, we systematically explore the parameter space by varying the disk sample diameter d from 40 nm to 180 nm and the external magnetic field $\mu_0 H$ from 0 T to 1.2 T in steps of $\Delta d = 4\,\text{nm}$ and $\mu_0 \Delta H = 20\,\text{mT}$, respectively. At every point in the parameter space, we minimise

the energy for a set of different initial magnetisation configurations: (i) five different skyrmionic configurations, (ii) three helical-like configurations with different helical period, (iii) the uniform out-of-plane configuration, and (iv) three random magnetisation configurations. We use the random magnetisation configurations in order to capture other equilibrium states not obtained by relaxing the well-defined initial magnetisation configurations.

The equilibrium states to which different initial magnetisation configurations relax in the energy minimisation process (at every d–H parameter space point) we present and discuss later in Sec. 3.7. We summarise the results from that section and determine the parameter space regions where different magnetisation states are in an equilibrium, and show them in Fig. 3.3. Among the eight computed equilibrium states, three are radially symmetric and we label them as iSk, Sk, and T, whereas the other states, marked as H2, H3, H4, 2Sk, and 3Sk, are not. Subsequently, we discuss the meaning of the chosen labels.

Firstly, we focus on the analysis of radially symmetric skyrmionic equilibrium states, supported by computing the skyrmion number S and scalar value S_a. In the first configuration, marked in Fig. 3.3 as iSk, the out-of-plane magnetisation component $m_z(x)$ profile along the horizontal symmetry line does not cover the entire $[-1, 1]$ range, as would be the case for a skyrmion configuration (where the magnetisation vector field $\mathbf{m}$ needs to cover the whole sphere). Accordingly, the scalar value S_a is smaller than 1. For these reasons we refer to this skyrmionic equilibrium state as the incomplete Skyrmion (iSk) state. A similar magnetisation configuration has been predicted and observed in other works for the case of two-dimensional systems in the presence of magnetocrystalline anisotropy where it is called either the quasi-ferromagnetic [41, 39] or edged vortex state [44, 42]. Because the iSk equilibrium state clearly differs from the ferromagnetic configuration and using the word vortex implies the topological charge of $1/2$, we prefer calling this state the incomplete skyrmion state. The incomplete Skyrmion (iSk) state emerges as an equilibrium state in the entire simulated d–H parameter space range. In the second equilibrium state, marked as Sk in Fig. 3.3, $m_z(x)$ covers the entire $[-1, 1]$ range, the magnetisation covers the sphere at least once and, consequently, the skyrmion configuration is present in the simulated sample. Although the skyrmion number value for this solution is $|S| < 1$ due to the additional magnetisation tilting at the disk boundary [41], which makes it indistinguishable from the previously described iSk equilibrium state, the scalar value is $1 < S_\mathrm{a} < 2$. This state is referred to as the isolated Skyrmion or just Skyrmion (Sk), in two-dimensional systems [41, 39], and we use the same name subsequently in this work. We find that the Sk state is not in an equilibrium for sample diameters smaller than 56 nm and external magnetic field values larger than approximately 1.14 T. Finally, the equilibrium magnetisation state marked as T in Fig. 3.3 covers the sphere at least twice. In other works, this state together with all other predicted higher-order solutions (not observed in this work) are called the

"target states" [43], and we use the same Target (T) state name. The analytic model in Sec. 3.2, used for generating initial skyrmionic states, also predicts the existence of target states. The T magnetisation configuration emerges as an equilibrium state for samples with diameter $d \geq 144\,\mathrm{nm}$ and field values $\mu_0 H \leq 0.24\,\mathrm{T}$.

The equilibrium states lacking radial symmetry can be classified into two groups: helical-like (marked as H2, H3, and H4) and multiple skyrmion (marked as 2Sk and 3Sk) states. The difference between the three helical-like states is in their helical period. More precisely, in the studied range of disk sample diameter values, either 2, 3, or 4 helical half-periods, including the additional magnetisation tilting at the disk sample edge due to the specific boundary conditions [41], fit in the sample diameter. Consequently, we refer to these states, that occur as an equilibrium state for samples larger than 88 nm and field values lower than 0.2 T, as H2, H3, and H4 . The other two radially non-symmetric equilibrium states are the multiple skyrmion configurations with 2 or 3 skyrmions present in the sample and we call these equilibrium states 2Sk and 3Sk, respectively. These configurations emerge as equilibrium states for samples with $d \geq 132\,\mathrm{nm}$ and external magnetic field values between $0.28\,\mathrm{T} \leq \mu_0 H \leq 1.06\,\mathrm{T}$.

3.4 Ground state

After we identified all observed equilibrium states in confined helimagnetic nanostructures, in this section, we focus on finding the equilibrium state with the lowest energy at all d–H parameter space points. For every parameter space point (d, H), after we compute and compare the energies of all found equilibrium states, we determine the lowest energy state, and refer to it, in this context, as the ground state. For the identified ground state, we compute the scalar value S_a and use it for plotting a d–H phase diagram shown in Fig. 3.4 (a). Discontinuous changes in the scalar value S_a define the boundaries between regions where different magnetisation configurations are the ground state. In the studied phase space, two different ground states emerge in the confined helimagnetic FeGe thin film disk samples: one with $S_\mathrm{a} < 1$ and the other with $1 < S_\mathrm{a} < 2$. The previous discussion of the S_a value suggests that these two regions correspond to the incomplete Skyrmion (iSk) and the isolated Skyrmion (Sk) states. We confirm this by visually inspecting two identified ground states, taken from the two phase space points (marked with circle and triangle symbols) in different regions, and show them in Fig. 3.4 (b) together with their out-of-plane magnetisation component $m_z(x)$ along the horizontal symmetry line.

A key result of this study is that the incomplete Skyrmion (iSk) and isolated Skyrmion (Sk) are the ground states at zero external magnetic field for different disk sample diameters. More precisely, iSk is the ground state for samples with diameter $d < 140\,\mathrm{nm}$

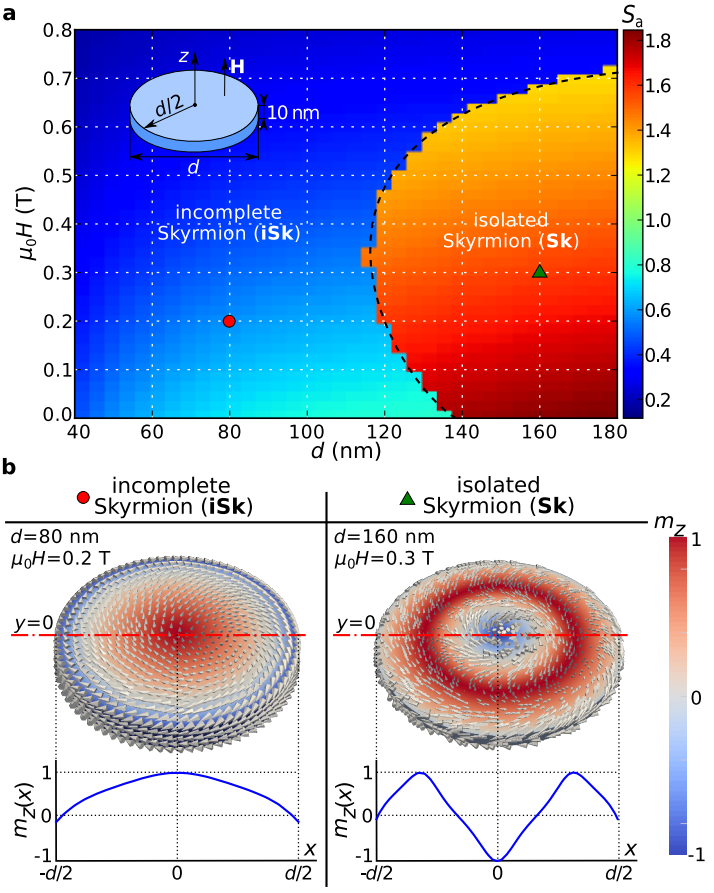

Figure 3.4: (**a**) The scalar value S_a for the thin film disk sample with thickness $t = 10\,\text{nm}$ as a function of disk diameter d and external out-of-plane magnetic field **H** (as shown in an inset). (**b**) Two identified ground states: incomplete Skyrmion (iSk) and isolated Skyrmion (Sk) magnetisation configurations at single phase diagram points together with their out-of-plane magnetisation component $m_z(x)$ profiles along the horizontal symmetry line.

and Sk is the ground state for $d \geq 140\,\text{nm}$. The Sk changes to the iSk ground state for large values of external magnetic field.

The phase diagram in Fig. 3.4 shows the phase space regions where iSk and Sk are the ground states, which means that all other previously identified equilibrium states are metastable. Now, we focus on computing the energies of metastable states relative to the identified ground state. Firstly, we compute the energy density E/V for all equilibrium states, where E is the total energy of the system and V is the disk sample volume, and then subtract the ground state energy density corresponding to that phase space point. We show the computed energy density differences $\Delta E/V$ when the disk sample diameter is changed in steps of $\Delta d = 2\,\text{nm}$ at zero external magnetic field in Fig. 3.5 (a). Similarly, the case when the disk sample diameter is $d = 160\,\text{nm}$ and the external magnetic field is changed in steps of $\mu_0 \Delta H = 20\,\text{mT}$ is shown in Fig. 3.5 (b). The magnetisation configurations are the equilibrium states in the d or H values range where the line is shown and collapse otherwise.

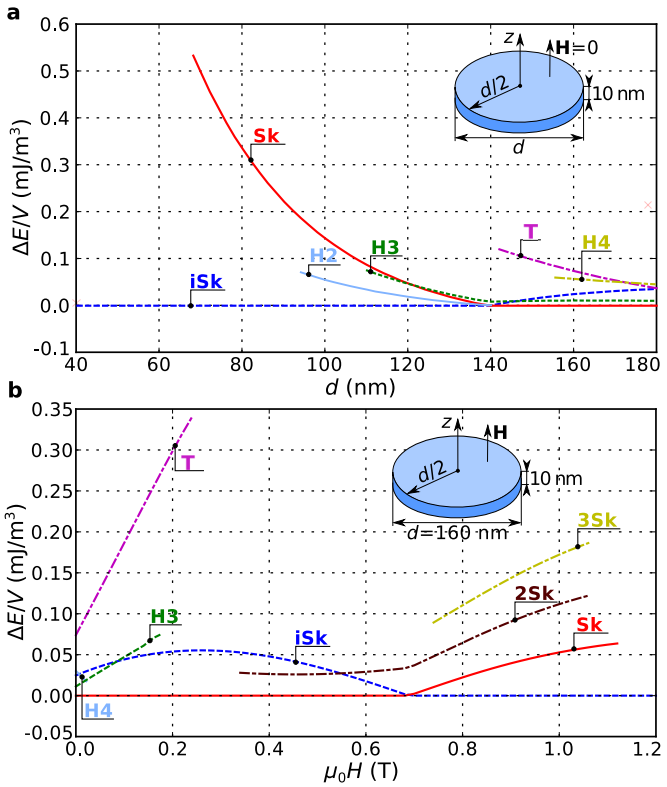

Figure 3.5: Energy density differences $\Delta E/V$ at (**a**) zero field for different sample diameters d and for (**b**) sample diameter $d = 160\,\mathrm{nm}$ and different external magnetic field values. Configurations are in equilibrium where the line is shown and collapse for other diameter or external magnetic field values.

The energy differences plotted in Fig. 3.5 are approximately of the $10^{-4}\,\mathrm{J/m^3}$ order. This could mean that even small thermal fluctuations could cause the transition between different states. This would further imply that these states cannot be used for storing data in confined helimagnetic nanostructures in practical data storage devices. However, the thermal stability of found states does not depend on the energy difference, but on the energy barriers separating them in the energy landscape. For instance, in a ferromagnetic grain with strong uniaxial anisotropy storing the bit, there are two energetically equivalent magnetisation states (up and down) storing the information bit (0 or 1). Consequently, the energy difference between them is zero. However, thermal fluctuations at room temperature do not disturb the system's state. This is because a large energy barrier (several dozens of $k_\mathrm{B}T$) is present between two equilibrium states. Consequently, in order to determine the thermal stability of individual equilibrium states presented in this work, additional studies must be performed. One of the possible ways is running nudged elastic band method [107, 108, 109, 110] simulations where a set of initial state images are relaxed in the energy landscape.

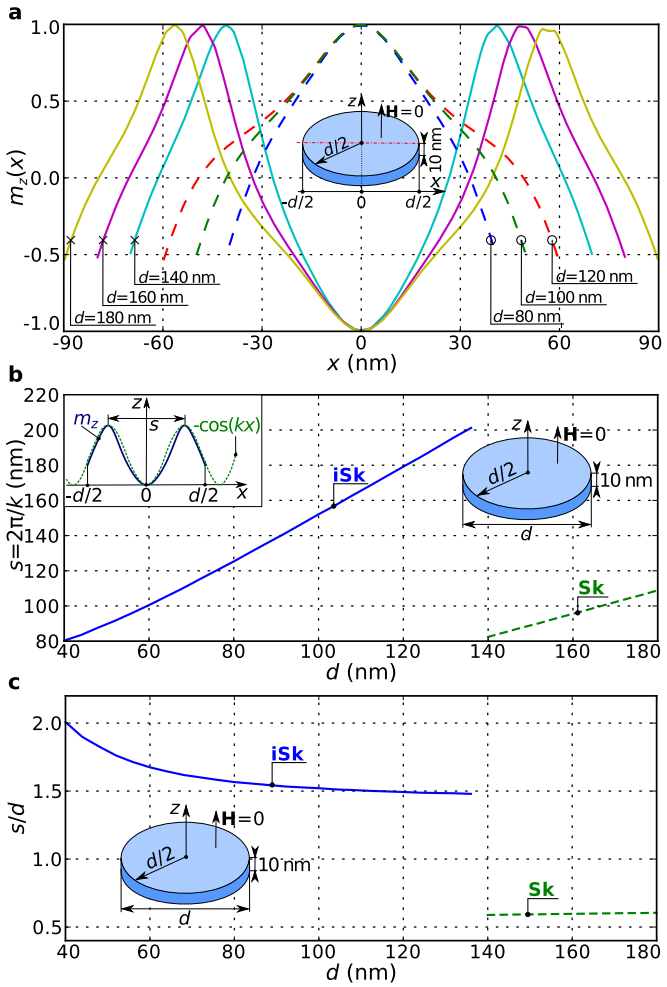

Figure 3.6: (**a**) Profiles of the out-of-plane magnetisation component $m_z(x)$ along the horizontal symmetry line for different thin film disk sample diameters with thickness $t = 10\,\text{nm}$ at zero external magnetic field $\mu_0 H = 0\,\text{T}$. The curves for $d \leq 120\,\text{nm}$ represent incomplete skyrmion ($\circ$) states, and for $d \geq 140\,\text{nm}$ represent isolated skyrmion ($\times$) states. (**b**) The skyrmionic state size $s = 2\pi/k$ (that can be interpreted as the length along which the full magnetisation rotation occurs) as a function of the hosting nanostructure size, obtained by fitting $m_z(x) = \pm\cos(kx)$ to the simulated profile. (**c**) The ratio of skyrmionic state size to disk sample diameter (s/d) as a function of hosting nanostructure size d.

3.5 Robustness

For the practical use of ground state skyrmionic states in helimagnetic nanostructures, their robustness is of great significance due to the unavoidable variations in the patterning process. Because of that, in Fig. 3.6 (a) we plot the out-of-plane magnetisation component $m_z(x)$ along the horizontal symmetry line for the iSk and the Sk ground state at zero external magnetic field for six different diameters d of the hosting disk nanostructure: three iSk profiles for $d \leq 120\,\mathrm{nm}$, and three Sk profiles for $d \geq 140\,\mathrm{nm}$. The profiles show that the two skyrmionic ground states have the opposite core orientations. In the case of the Sk states, the magnetisation at the core is antiparallel and at the outskirt parallel to the external magnetic field. This reduces the Zeeman energy $E_\mathrm{z} = -\mu_0 M_\mathrm{s} \int \mathbf{H} \cdot \mathbf{m}\,\mathrm{d}^3 r$ because the majority of the magnetisation in the isolated skyrmion outskirts points in the same direction as the external magnetic field $\mathbf{H}$. Once the disk diameter is sufficiently small that less than a complete spin rotation fits into the sample, this orientation is not energetically favourable anymore and the iSk state emerges. In this iSk state, the core magnetisation points in the same direction as the external magnetic field in order to minimise the Zeeman energy. We compute and plot the skyrmionic state size $s = 2\pi/k$ as a function of the disk sample diameter d in Fig. 3.6 (b). We obtain the size s, that can be interpreted as the length along which the full magnetisation rotation occurs, by fitting k in the $f(x) = \pm\cos(kx)$ function to the simulated iSk and Sk $m_z(x)$ profiles. In Fig. 3.6 (c), we show how the ratio of skyrmionic state size to disk sample diameter (s/d) depends on the hosting nanostructure size. Although this ratio is constant ($s/d \approx 0.6$) for the Sk state, in the iSk case, it is larger for smaller samples and decreases to $s/d \approx 1.5$ in larger nanostructures. In agreement with related findings for two-dimensional disk samples [42] we find that both iSk and Sk are able to change their size s in order to accommodate the size of hosting nanostructure, which provides robustness for the technological use.

3.6 Possible stabilisation mechanism

The emergence of skyrmionic configuration ground state in helimagnetic nanostructures at zero external magnetic field and in absence of magnetocrystalline anisotropy is unexpected [34]. Now, we discuss the possible mechanisms, apart from the geometrical confinement, responsible for this stability, in particular (i) the demagnetisation energy contribution, and (ii) the magnetisation variation along the out-of-film direction, shown in Fig. 3.7, which can radically change the skyrmion energetics in infinitely large helimagnetic thin films [40]. We repeat the simulations using the same method and model as above but ignoring the demagnetisation energy contribution (i.e. setting the demagnetisation energy density w_d in Eq. (3.1) artificially to zero). We then carry out the

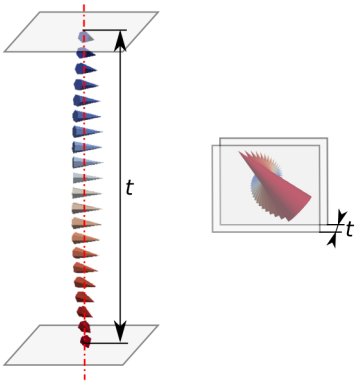

Figure 3.7: Translational variation of magnetisation in the out-of-film direction.

calculations (i) on a three-dimensional (3d) mesh (i.e. with spatial resolution in z direction) and (ii) on a two-dimensional (2d) mesh (i.e. with no spatial resolution in z direction, and thus not allowing a variation of the magnetisation along the z direction). The disk sample diameter d is changed between 40 nm and 180 nm in steps of $\Delta d = 5$ nm and the external magnetic field $\mu_0 H$ is changed systematically between 0 T and 0.5 T in steps of $\mu_0 \Delta H = 25$ mT. The two resulting phase diagrams are shown in Fig. 3.8, where subplots (a) and (c) show S_a as a function of d and H. Because the scalar value S_a does not provide enough contrast to determine the boundaries of the new Helical (H) ground state region, the skyrmion number S is plotted for the relevant phase diagram areas and shown in Fig. 3.8 (b) and Fig. 3.8 (d).

We demonstrate the importance of including demagnetisation effects into the model by comparing Fig. 3.8 (a) (without demagnetisation energy) and Fig. 3.4 (a) (with demagnetisation energy). In the absence of the demagnetisation energy, the isolated Skyrmion (Sk) configuration is not found as the ground state at zero applied field; instead, Helical (H) configurations have lower energies. At the same time, the external magnetic field at which the skyrmion configuration ground state disappears is reduced from about 0.7 T to about 0.44 T.

By comparing Fig. 3.8 (a) computed on a 3d mesh and Fig. 3.8 (c) computed on a 2d mesh, we can see the importance of spatial resolution in the out-of-plane direction of the thin film, and how it contributes to the stabilisation of isolated Skyrmion (Sk) state. In the 2d model, the field range over which skyrmions can be observed as the ground state is further reduced to approximately [0.05 T, 0.28 T]. In the 3d mesh model the Sk configuration can reduce its energy by twisting the magnetisation at the top of the disk relative to the bottom of the disk so that along the z direction the magnetisation starts to exhibit (a part of) the helix that arises from the competition between symmetric exchange and DMI energy terms, similar to the work by Rybakov et al. [40] A similar twist provides no energetic advantage to the helix configuration, thus the Sk state region

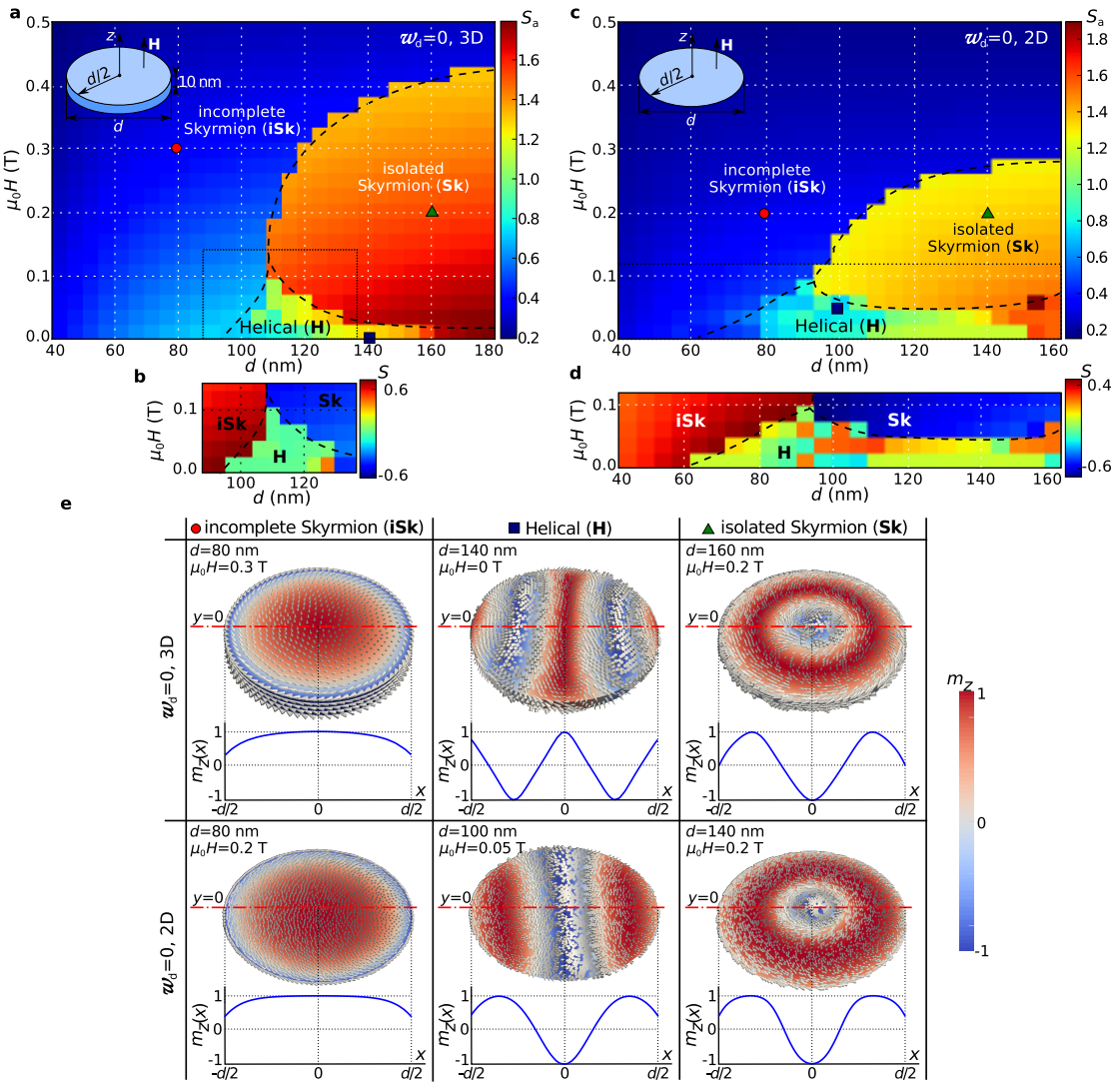

Figure 3.8: The scalar value S_a as a function of disk sample diameter d and external magnetic field H computed for the ground state at every phase space point in absence of demagnetisation energy contribution for (**a**) a 3d mesh and (**c**) for a 2d mesh. In order to better resolve the boundaries of the Helical (H) state region, the skyrmion number S is shown in (**b**) and (**d**). (**e**) The magnetisation configurations of three identified ground states as well as the out-of-plane magnetisation component $m_z(x)$ along the horizontal symmetry line.

in Fig. 3.8 (a) is significantly larger than the Sk state region in Fig. 3.8 (c) where the 2d mesh does not allow any variation of the magnetisation along the z direction and thus the partial helix cannot form.

While the isolated Skyrmion (Sk) configuration at zero field is a metastable state in the absence of demagnetisation energy, or in 2d models, it is not the ground state anymore as there are Helical (H) equilibrium configurations that have lower total energy. The demagnetisation energy appears to suppress these helical configurations which have a lower energy than the skyrmion. The variation of the magnetisation along the z direction stabilises the skyrmion configuration substantially. These findings demonstrate the subtle nature of competition between symmetric exchange, DM and demagnetisation interactions, and show that ignoring the demagnetisation energy or approximating the thin film helimagnetic samples using two-dimensional models is not generally justified.

3.7 Relaxation diagrams

In this section, we present the equilibrium states at all points in the d–H parameter space obtained by relaxing well-defined initial states, introduced in Sec. 3.2. More precisely, we compute the equilibrium states (local energy minima) that result from a particular initial condition. This allows us to provide a systematic overview of equilibrium states, and gain additional insight about the energy landscape of the studied system. We vary the sample diameter between 40 nm and 180 nm in steps of $\Delta d = 4\,\mathrm{nm}$ and the external magnetic field between $\mu_0 H = 0\,\mathrm{T}$ and $\mu_0 H = 1.2\,\mathrm{T}$ in steps of $\mu_0 \Delta H = 20\,\mathrm{mT}$. Relaxation diagrams are represented by plotting the scalar value S_a as a function of disk diameter d and applied field strength H, and Fig. 3.9 shows the relaxation diagrams for skyrmionic initial configurations A-E, and Fig. 3.11 shows the relaxation diagrams for helical H2, H3, H4, and uniform U initial configurations. These relaxation diagrams were used to create the phase diagram of equilibrium states, shown in Fig. 3.3 as a summary of the main results presented and discussed in this section. All equilibrium states we found by relaxing a set of initial states are shown in Fig. 3.10.

We now discuss each of relaxation diagrams in Fig. 3.9 and 3.11, where each subplot corresponds to one particular initial configuration. The scalar value S_a, as a function of disk sample diameter d and external magnetic field H, computed for the final relaxed equilibrium state, i.e. local or global energy minimum, we show in Fig. 3.9 (A) for the energy minimisation process that started from the skyrmionic initial configuration A (shown in Fig. 3.1). The "iSk↑" label refers to the incomplete Skyrmion (iSk) magnetisation configuration with the core magnetisation pointing in the positive z direction. An example of this state, marked with the same label, is shown in Fig. 3.10. From the Fig. 3.9 (A), we can see that for all examined diameters and external field values, the final relaxed configuration is the iSk↑ state. Now, this relaxation diagram is compared

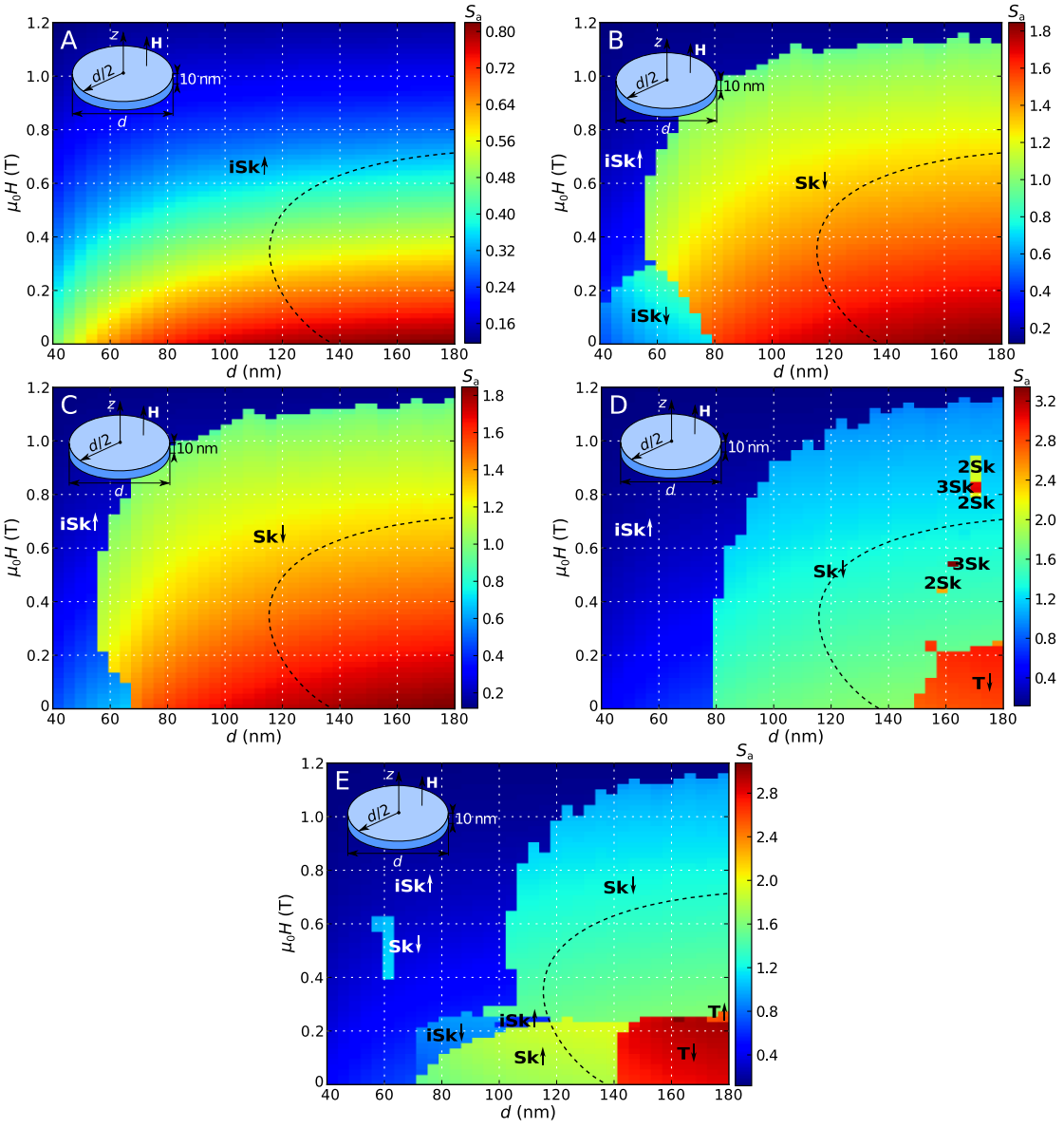

Figure 3.9: The relaxation diagrams obtained by relaxing skyrmionic initial state A-E. The initial states correspond to the first five solutions of the analytic model and the phase diagrams are marked A-E accordingly. The relaxation diagrams are represented as the dependence of scalar value S_a on the disk sample diameter d and an external field H (as shown in insets).

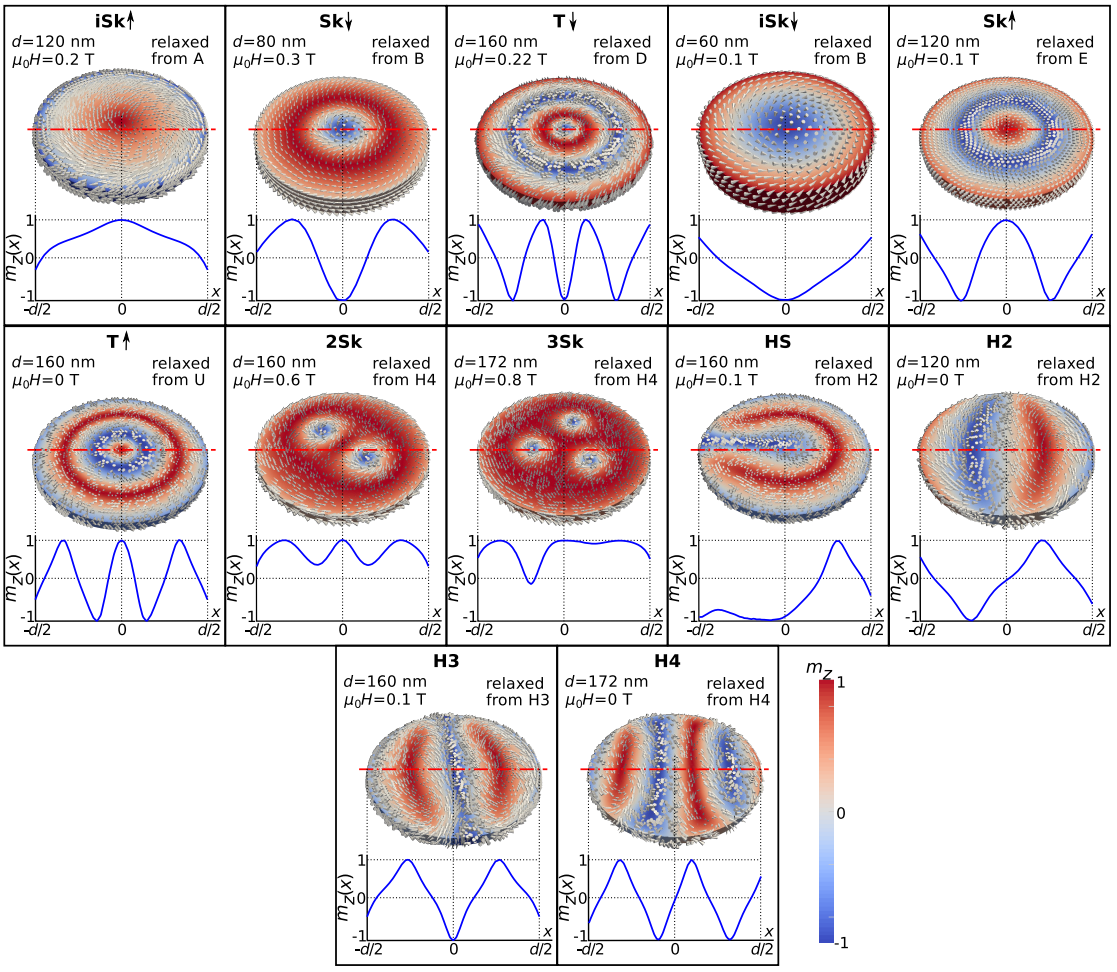

Figure 3.10: All identified equilibrium magnetisation configurations.

with the ground state phase diagram, shown in Fig. 3.4 (a), and the boundary between two ground state (iSk and Sk) regions is shown as the dashed line in the discussed relaxation diagram. We can see that the iSk is indeed the ground state (i.e. the global energy minimum) for $d < 140\,\text{nm}$, but for larger diameters the isolated Skyrmion (Sk) configuration has a lower energy, and thus the iSk configuration is only a local energy minimum.

Similarly, if the energy minimisation process is started from the initial configuration B, shown in Fig. 3.1 (B), the $S_\text{a}(d, H)$ for the final relaxed magnetisation state is obtained and shown in Fig. 3.9 (B). The vast majority of the final configurations ($d \geq 80\,\text{nm}$ and $\mu_0 H \lesssim 1.1\,\text{T}$), labelled as "Sk↓", correspond to the isolated skyrmion state with the core pointing in the negative z direction. An example of this state we show in Fig. 3.10, marked with the same label. By comparison with the ground state phase diagram shown in Fig. 3.4 (a), we can see that the Sk is the ground state for large diameters $d \geq 140\,\text{nm}$ and field values $\mu_0 H < 0.7\,\text{T}$. However, for smaller diameters the isolated skyrmion configuration is only metastable (as the iSk configuration is the ground state). We can see that in the vicinity of $d \approx 60\,\text{nm}$ and $\mu_0 H \approx 0.1\,\text{T}$ parameter space point, the

initial configuration B relaxes to the incomplete skyrmion state with core oriented in the negative z direction (iSk↓), but for larger field values, configuration B falls into the iSk↑ configuration (see Fig. 3.10 for detailed configurations of iSk↓ and iSk↑ states). The iSk↓ has a higher energy than the iSk↑ as the majority of the magnetisation is pointing in the direction opposite to the applied field. However, the initial configuration B is such that the core is pointing down, and there appears to be a direct energy minimisation path to the iSk↓ configuration for field values smaller than approximately 0.3 T. For larger fields, the Zeeman energy becomes so important that the initial configuration B leads to the the iSk↑ configuration.

The initial configuration C suppresses the iSk↓ state completely, as shown in Fig. 3.9 (C), but is otherwise similar to the case when relaxation is started from the initial state B. We note in particular that the Sk configuration cannot exist for $d < 60\,\text{nm}$ even if the relaxation is started from a Sk-like configuration B or C, i.e. there are no metastable isolated skyrmion states at the smallest diameters. If the system is relaxed from the initial state D, shown in Fig. 3.1 (D), a qualitative change from Fig. 3.9 (B) and (C) is evident as shown in Fig. 3.9 (D). In addition to the iSk↑ and Sk↓ states, there are now a number of, according to Fig. 3.5, higher energy metastable states emerging as 2 or 3 skyrmions in the disk (see Fig. 3.10 for detailed plots of 2Sk and 3Sk states). Furthermore, for small field values $\mu_0 H \lesssim 0.2\,\text{T}$ and large diameters $d \gtrsim 152\,\text{nm}$, the Target (T) equilibrium state with core orientation in the negative z direction (T↓) arises. The T↓ state is shown in Fig. 3.10. The scalar value $S_\text{a}(d, H)$ computed for final equilibrium configurations in Fig. 3.9 (E) we obtained by relaxing the initial configuration E shown in Fig. 3.1. The initial skyrmionic state E does not relax to 2 and 3 skyrmion configurations but allows the Sk↑ state to arise for small field values.

The $S_\text{a}(d, H)$ for starting configurations H2, H3 and H4 (as shown in Fig. 3.1) we show in Fig. 3.11 (H2), (H3), and (H4), respectively, . All three initial configurations result in the incomplete Skyrmion configuration with core pointing up (iSk↑) for the smallest diameters as well as for largest fields. The H3 initial configuration relaxes into a configuration with two Skyrmions in the disk (2Sk) for $d > 120\,\text{nm}$ and field values between 0.8 T and 1.1 T. These 2Sk configurations had appeared occasionally when starting from configuration D (see Fig. 3.9 (D)). The H4 initial configuration also encourages 3 skyrmions in the disk to arise as a metastable state. Fig. 3.10 (U) shows S_a for final configurations when the simulation starts from a uniform magnetisation, pointing up in the positive z direction. This results mostly in the incomplete Skyrmion configuration with core pointing up (iSk↑). However, we also find the Skyrmion with core pointing down Sk↓ and the Target configuration T↑ as the diameter increases and the field decreases. Fig. 3.9 (A) is interesting to compare with Fig. 3.11 (U): in the former, only the iSk↑ state results, presumably because from the initial state A, only the iSk↑ state is accessible in the relaxation. On the contrary, for the uniform configuration, the system finds the energy minimum for the isolated Skyrmion state Sk↓ and the Target

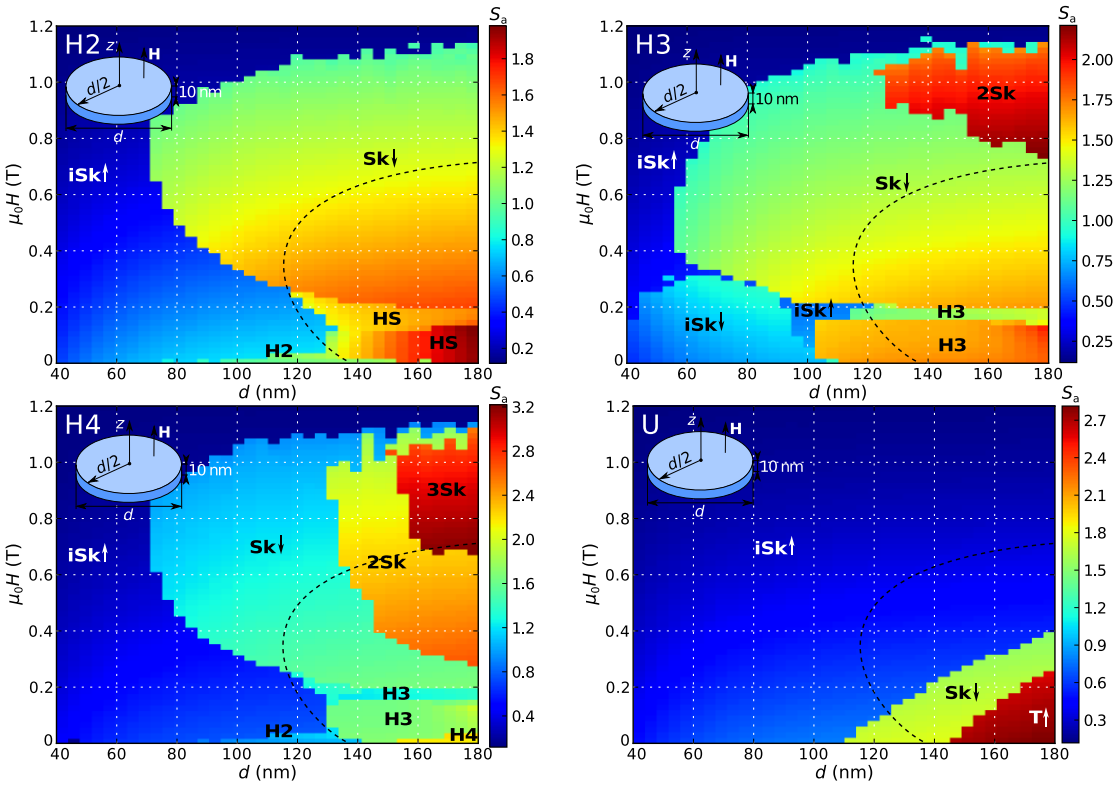

Figure 3.11: The relaxation diagrams obtained by relaxing helical and uniform initial state. The initial states correspond to the helical states H2, H3, and H4, as well as the uniform state U, and the relaxation diagrams are marked accordingly. The relaxation diagrams are represented as the dependence of scalar value S_a on the disk sample diameter d and an external field H (as shown in insets).

T↑ because other energy minima can be accessed from this initial state. Fig. 3.5 (a) shows the relative energies of the different metastable states for $H = 0$.

3.8 Higher ordering temperature material

The ordering temperature of simulated FeGe material, $T_C = 278.7\,\mathrm{K}$ [102], is lower than the room temperature, which means that this material cannot be used to fabricate a device operating at room temperature. Therefore, it is important to determine how our results regarding the identified lowest energy state would change for the material with higher ordering temperature. Because no high ordering temperature helical B20 material has been reported to this day, the best we can do is to artificially increase the ordering temperature, estimate new material parameters, and repeat the study of equilibrium states.

We increase the ordering temperature to $T_C = 350\,\mathrm{K}$, and calculate new values of exchange and Dzyaloshinskii-Moriya energy constants (following the estimation described

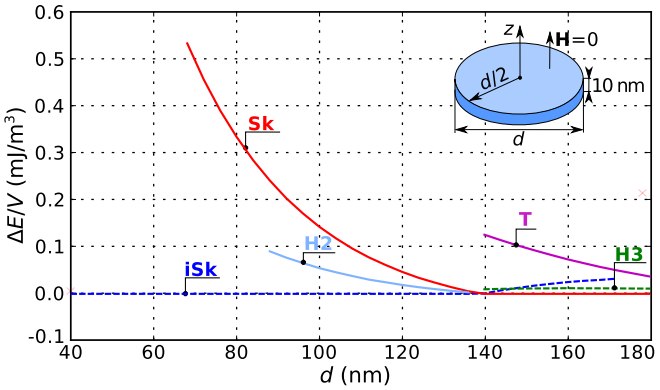

Figure 3.12: The energy density differences between all identified equilibrium states and corresponding lowest energy state as a function of disk sample diameter. A full set of initial state configurations are relaxed for different disk sample diameter values at zero external magnetic field. The helimagnetic material ordering temperature is artificially increased to $T_C = 350\,\mathrm{K}$ (above room temperature).

in Sec. 3.1.2) and obtain $A = 1.1 \times 10^{-11}\,\mathrm{J/m}$ and $D = 1.98 \times 10^{-3}\,\mathrm{J/m^2}$. Using these values, we relax the full set of initial magnetisation configurations at zero external magnetic field for different disk sample diameters. More precisely, we vary the disk sample diameter between 40 nm and 180 nm in steps of 4 nm and compute the energy density E/V of all identified relaxed equilibrium states, where V is the sample volume. After that, from the computed energy density, we subtract the energy density of the corresponding lowest energy state. We plot the calculated energy density differences of all equilibrium states as a function of disk sample diameter d and show them in Fig. 3.12.

By comparing the Fig. 3.12 for higher ordering temperature material with Fig. 3.5 (a), we conclude that the incomplete Skyrmion (iSk) state remains the lowest energy state for $d < 140\,\mathrm{nm}$, whereas the isolated Skyrmion (Sk) state is the lowest energy state for $d \geq 140\,\mathrm{nm}$. However, the iSk state is not an equilibrium state for disk sample diameters larger than 172 nm, which is in contrast to the FeGe material case where iSk is in an equilibrium for all examined d values. Another difference is that the metastable Target (T) state is the highest energy state for the whole d range where it is an equilibrium state. Finally, we do not observe H4 state (helical state with four half periods) for this high ordering temperature material.

3.9 Summary

In this section, we systematically relaxed a series of initial magnetisation configurations in a 10 nm thin film helimagnetic FeGe disk sample with diameter d using full three-dimensional micromagnetic simulations. An external magnetic field is applied uniformly and perpendicular to the sample in the positive z direction. By varying d and H, we

obtained equilibrium states that can emerge in the studied samples. After that, we compared the energies of all obtained equilibrium states at different parameter space points and selected the state with the lowest energy and refer to it as the ground state. The key results of this systematic study is that skyrmionic states in the form of incomplete Skyrmion (iSk) and isolated Skyrmion (Sk) states emerge as the ground state in confined helimagnetic nanostructures in absence of both external magnetic field and magnetocrystalline anisotropy. We also show that skyrmionic states are able to adapt their size in order to accommodate the hosting nanostructure which demonstrates their robustness which is required for their possible technological use. The emergence of skyrmionic states in thin film helimagnetic materials at zero external magnetic field and in absence of magnetocrystalline anisotropy is unexpected in comparison to the infinitely large thin films. Because of that, we also explored the possible mechanism that might be responsible for this stability. We found that neglecting the demagnetisation energy contribution and/or restricting the magnetisation variation in the out-of-film direction increases the energy of skyrmionic states with respect to the helical configurations. This results also shows that neglecting the demagnetisation energy or modelling thin film helimagnetic nanostructures using two-dimensional meshes in micromagnetic simulations is not always justified. Finally, we show that if the ordering temperature of the simulated material is artificially increased above the room temperature, both iSk and Sk states remain the ground state configurations at zero external magnetic field. A more detailed discussion of the stability of skyrmionic states can be found in Chapter 6. Since the publication of this work, an experimental study of skyrmionic states in confined helimagnetic FeGe nanostructures was published [111]. In that work, multiple skyrmion states, together with different helical configurations were observed in thin film disk samples with 270 nm diameter.

Chapter 4

Hysteretic behaviour and reversal mechanism

In the previous chapter we found that skyrmionic configurations emerge as the ground state in confined helimagnetic nanostructures in the form of incomplete Skyrmion (iSk) and isolated Skyrmion (Sk) states. Now, we show that bistable skyrmionic states undergo hysteretic behaviour between two energetically equivalent skyrmionic states with different core orientation. The hysteretic behaviour remains present even in the absence of both magnetocrystalline and demagnetisation-based shape anisotropies, suggesting the existence of novel Dzyaloshinskii-Moriya-based shape anisotropy. Finally, we show that the skyrmionic state core reversal dynamics is facilitated by the Bloch point occurrence and propagation, where the direction of its propagation strongly depends on the simulation parameters.

4.1 Methods

We simulate 10 nm thin film helimagnetic FeGe disk samples using the same micromagnetic model presented in the Sec. 3.1.1. The used FeGe material parameters are: magnetisation saturation $M_\mathrm{s} = 384\,\mathrm{kA\,m^{-1}}$, exchange energy constant $A = 8.78\,\mathrm{pJ\,m^{-1}}$, and Dzyaloshinskii-Moriya constant $|D| = 1.58\,\mathrm{mJ\,m^{-2}}$ and we show their estimation in Sec. 3.1.2. In order to support the discussion of presented results, we compute the skyrmion number S and injective scalar value S_a as defined in Sec. 3.1.3.

4.2 Hysteretic behaviour

The phase diagram in Fig. 3.4 (a) shows the regions in which incomplete Skyrmion (iSk) and isolated Skyrmion (Sk) configurations are the ground states. Intuitively, one can

assume that for every sample diameter d at zero external magnetic field, there are two possible skyrmionic magnetisation configurations of equivalent energy: core pointing up or core pointing down, suggesting that these states can be used for an information bit (0 or 1) encoding. We now investigate this hypothesis and study whether an external magnetic field can be used to switch the skyrmionic state orientation (crucial for data imprint) by simulating the hysteretic behaviour of ground state skyrmionic states.

We obtain the hysteresis loops in the usual way by evolving the system to an equilibrium state after changing the external magnetic field, and then using the resulting state as the starting point for a new evolution. In this way, a magnetisation loop takes into account the history of the magnetisation configuration. The external magnetic field $\mu_0\mathbf{H}$ is applied in the positive z direction and changed between $-0.5\,\mathrm{T}$ and $0.5\,\mathrm{T}$ in steps of $\mu_0\Delta H = 5\,\mathrm{mT}$. The hysteresis loops are represented as the dependence of the average out-of-plane magnetisation component $\langle m_z \rangle$ on the external magnetic field H. The hysteresis loop for a 10 nm thin film disk sample with $d = 80\,\mathrm{nm}$ diameter in which the incomplete Skyrmion (iSk) is the ground state is shown in Fig. 4.1 (a) as a solid line. Similarly, a solid line in Fig. 4.1 (b) shows the corresponding hysteresis loop for a larger disk sample with $d = 150\,\mathrm{nm}$ diameter in which the isolated Skyrmion (Sk) is the ground state. The hysteresis between two energetically equivalent skyrmionic magnetisation states with the opposite core orientation at zero external magnetic field, shown in Fig. 4.1 (c), is evident. Moreover, the system does not relax to any other equilibrium state at any point in the hysteresis loop, which demonstrates the bistability of skyrmionic states in studied system. The area of the open loop in the hysteresis curve is a measure of the work needed to reverse the core orientation by overcoming the energy barrier separating the two skyrmionic states with opposite core orientation.

As throughout this work, it is assumed that the simulated helimagnetic material is isotropic, and thus, the magnetocrystalline anisotropy energy contribution is neglected. Due to that, one might expect that the obtained hysteresis loops are the consequence of demagnetisation-based shape anisotropy. To address this, we simulate hysteresis using the same method, but this time in absence of the demagnetisation energy contribution. More precisely, the minimalistic energy model contains only the symmetric exchange and Dzyaloshinskii-Moriya interactions together with Zeeman coupling to an external magnetic field. We show the obtained hysteresis loops in Fig. 4.1 (a) and (b) as dashed lines. The hysteretic behaviour remains, although all energy terms that usually give rise to the hysteretic behaviour (magnetocrystalline anisotropy and demagnetisation energies) were neglected. This suggests the existence of a new magnetic anisotropy that we refer to as the Dzyaloshinskii-Moriya-based shape anisotropy.

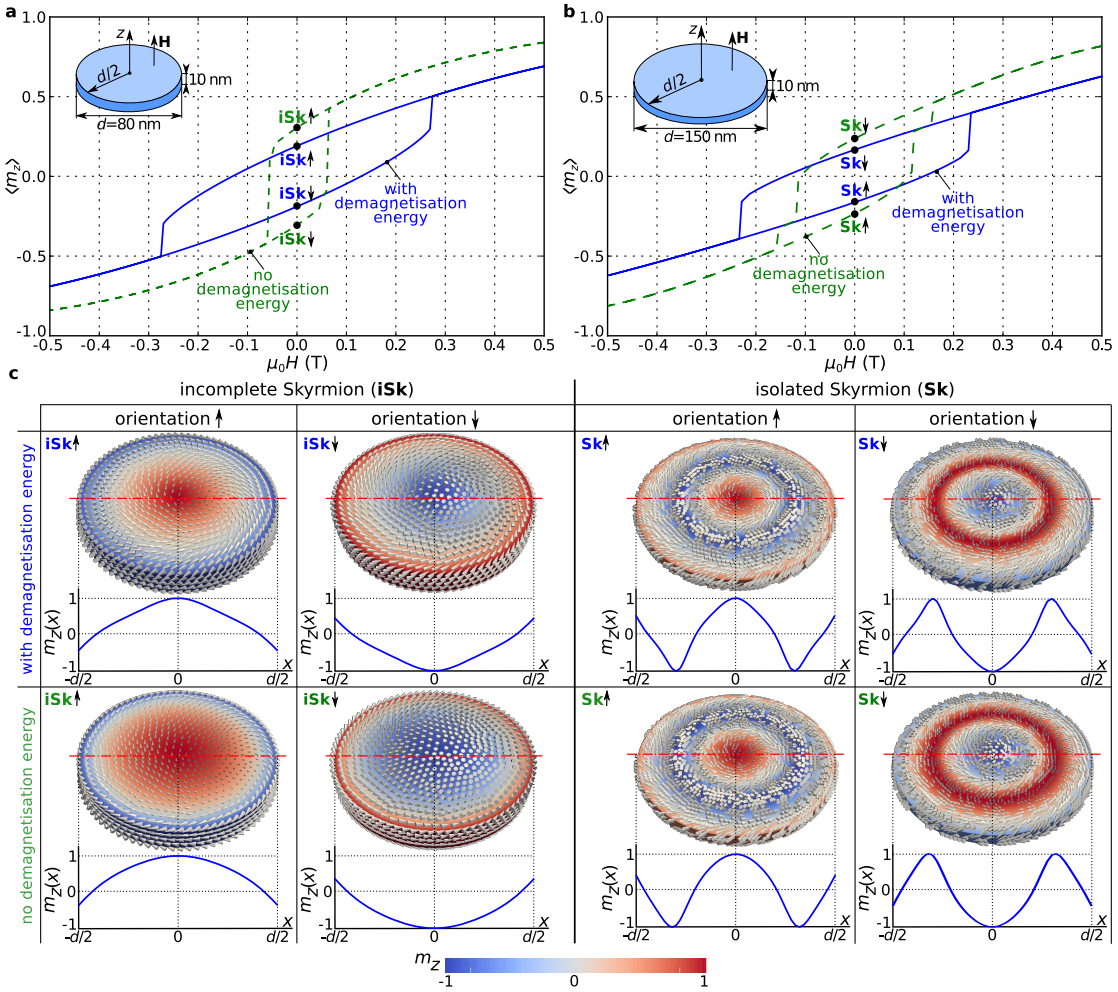

Figure 4.1: The average out-of-plane magnetisation component $\langle m_z \rangle$ hysteretic dependence on the external out-of-plane magnetic field H for 10 nm thin film disk samples for (**a**) incomplete Skyrmion (iSk) magnetisation configuration in $d = 80$ nm diameter sample and (**b**) isolated Skyrmion (Sk) magnetisation configuration in $d = 150$ nm diameter sample. (**c**) The magnetisation states and $m_z(x)$ profiles along the horizontal symmetry lines for positive and negative iSk and Sk core orientations from $H = 0$ in the hysteresis loop, both in presence and in absence of demagnetisation energy (demagnetisation-based shape anisotropy).

4.3 Reversal mechanism

The hysteresis loops in Fig. 4.1 show that skyrmionic states in confined thin film helimagnetic nanostructures undergo hysteretic behaviour and that an external magnetic field can be used to change their orientation from core pointing up to core pointing down and vice versa. In this section, we discuss the mechanism by which the skyrmionic state core orientation reversal occurs. We simulate a 150 nm diameter thin film FeGe disk sample with $t = 10$ nm thickness. The maximum spacing between two neighbouring

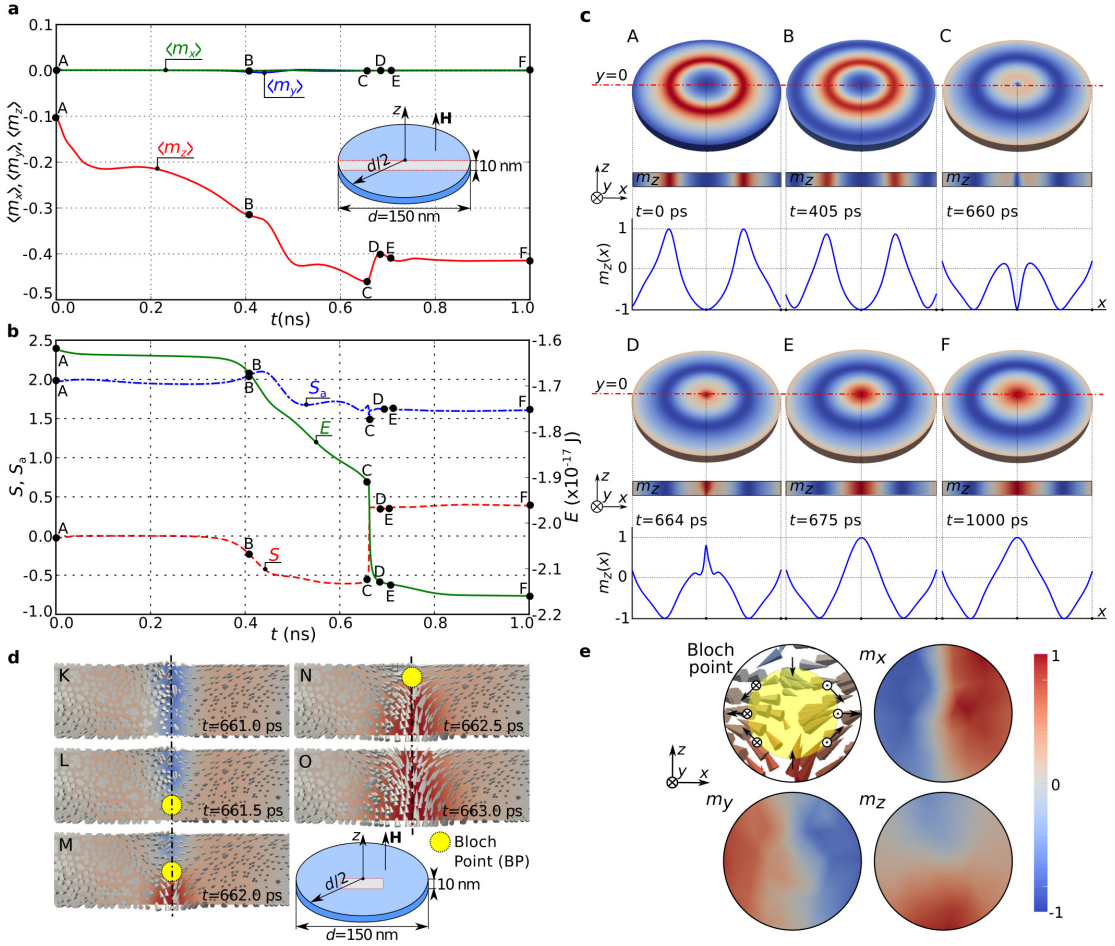

Figure 4.2: (**a**) The spatially averaged magnetisation components $\langle m_x \rangle$, $\langle m_y \rangle$, and $\langle m_z \rangle$ and (**b**) skyrmion number S, scalar value S_a, and total energy E time evolutions in the reversal process over 1 ns. The simulated sample is a 10 nm thin film disk with 150 nm diameter. (**c**) The magnetisation states at different instances of time (points A to F) together with m_z colourmap in the xz cross section and $m_z(x)$ profiles along the horizontal symmetry line. (**d**) The m_z colourmap and magnetisation field in the central part of xz cross section as shown in an inset together with the position of Bloch point (BP). (**e**) The BP structure along with colourmaps of magnetisation components which shows that the magnetisation covers the closed surface (sphere surrounding the BP) exactly once.

finite element mesh nodes is reduced to 1.5 nm in order to better resolve the magnetisation. According to the hysteresis loop in Fig. 4.1 (b), the switching field H_s of the isolated skyrmion state in this geometry from core orientation down to core orientation up is $\mu_0 H_\mathrm{s} \approx -235\,\mathrm{mT}$. Therefore, we first relax the system at $-210\,\mathrm{mT}$ external magnetic field and then decrease it abruptly to $-250\,\mathrm{mT}$. We simulate the magnetisation dynamics for 1 ns, governed by a dissipative LLG equation [79] with Gilbert damping $\alpha = 0.3$ [39], and record it every $\Delta t = 0.5\,\mathrm{ps}$.

We now look at how certain magnetisation configuration parameters evolve during the

reversal process. We show the time-dependent average magnetisation components $\langle m_x \rangle$, $\langle m_y \rangle$, and $\langle m_z \rangle$ in Fig. 4.2 (a), and on the same time axis, the skyrmion number S, scalar value S_a and total energy E in Fig. 4.2 (b). The initial magnetisation configuration at $t = 0\,\mathrm{ns}$ is denoted as A and the final relaxed magnetisation at $t = 1\,\mathrm{ns}$ as F. We show in Fig. 4.2 (c) the out-of-plane magnetisation field component m_z in the whole sample, in the xz cross section, as well as along the horizontal symmetry line. At approximately 662 ps the skyrmionic core reversal occurs and Fig. 4.2 (b) shows an abrupt change both in skyrmion number S and total energy E. We summarise the reversal process with the help of six snapshots shown in Fig. 4.2 (c). Firstly, in (A-B), the isolated skyrmion core shrinks. At some point the maximum m_z value lowers from 1 to approximately 0.1 (C). After that, the core reverses its direction (D) and an isolated skyrmion of different orientation is formed (E). From that time onwards, the core expands in order to accommodate the size of hosting nanostructure, until the final state (F) is reached.

In order to better understand the actual reversal of the skyrmionic state core between $t_1 \approx 661\,\mathrm{ps}$ and $t_2 \approx 663\,\mathrm{ps}$, we show additional snapshots of the magnetisation vector field and m_z colourmap in the xz cross section in Fig. 4.2 (d). The location marked by a circle in subplots L, M, and N identifies a Bloch Point (BP): a noncontinuous singularity in the magnetisation pattern where the magnetisation magnitude vanishes to zero [112, 113]. Because micromagnetic models assume constant magnetisation magnitude, the precise magnetisation configuration at the BP cannot be obtained using micromagnetic simulations [114]. However, it is known how to identify the signature of the BP in such situations: the magnetisation direction covers any sufficiently small closed surface surrounding the BP exactly once [115, 116]. We illustrate this property in Fig. 4.2 (e) using a vector plot together with m_x, m_y, and m_z colour plots that show the structure of a Bloch point. We conclude that the isolated skyrmion core reversal occurs via Bloch Point (BP) occurrence and propagation. Firstly, at $t \approx 661.5\,\mathrm{ps}$ the BP enters the sample at the bottom boundary and propagates upwards until $t \approx 663\,\mathrm{ps}$ when it leaves the sample at the top boundary.

One could ask whether we can get a better resolution of Bloch point configuration by reducing the maximum spacing between two neighbouring nodes l_max in the finite element mesh. However, reducing l_max would also reduce the size of Bloch point which would further increase the energy of magnetisation configuration containing the BP. In order to illustrate this, let us assume a hedgehog type of Bloch point [116, 117], where the magnetisation on a sphere surrounding the BP points in the direction from the sphere's centre. Along any sphere diameter, there are two points on the sphere at which magnetisation vectors point in the opposite direction. Accordingly, the exchange energy between them is large and increases by reducing their distance (diameter). Therefore, by reducing the sphere diameter (mesh discretisation l_max), the exchange energy increases. When the BP energy becomes too high in the skyrmionic state core reversal, the system would probably choose a different transition path instead of the one containing the BP.

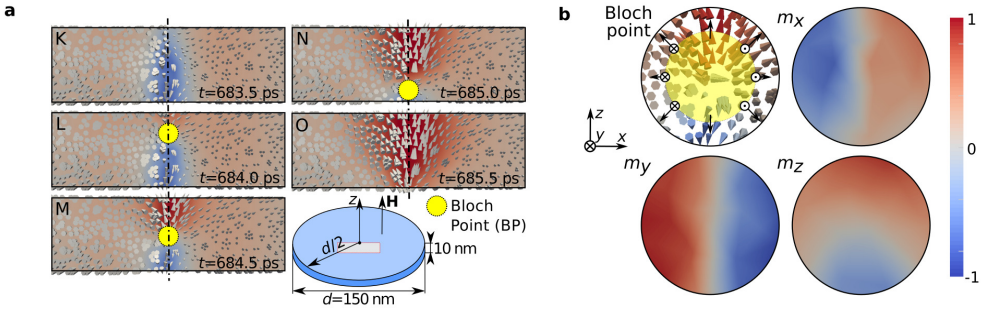

Figure 4.3: The isolated skyrmion orientation reversal in confined three-dimensional helimagnetic nanostructure with downwards Bloch point propagation direction. (**a**) The m_z colourmap and magnetisation field in the central part of xz cross section as shown in an inset together with the position of Bloch Point (BP). (**b**) The BP structure along with colourmaps of magnetisation components which shows that the magnetisation covers the closed surface (sphere surrounding the BP) exactly once.

Because of that, although the continuous micromagnetic simulations give us enough information to determine whether a BP is present in the sample, the only appropriate way of determining its configuration by using discrete spin lattice models [114].

4.3.1 Different Bloch point propagation direction

We note that the Bloch point moves upwards in Fig. 4.2 (d) but one may ask whether an opposite propagation direction can occur and how the Bloch point structure is going to change. We hypothesise that both reversal paths (Bloch point moving upwards or downwards) exhibit the same energy barriers and that the choice of path is a stochastic process. In order to illustrate a different direction of the Bloch Point (BP) propagation, we show a result from another skyrmion reversal. The simulation parameters are the same as in Fig. 4.2, except that the Gilbert damping α is increased from 0.3 to 0.35. We show the results of isolated skyrmion core orientation reversal dynamics with modified Gilbert damping in Fig. 4.3.

Now, the obtained reversal dynamics is compared with the reversal dynamics shown in Fig. 4.2. From the Fig. 4.3 (a), we can see that the Bloch point enters the sample at the top boundary at approximately 684 ps, then propagates downwards to the bottom boundary, where it leaves the sample at approximately 685 ps. Because of the opposite BP propagation direction, the structure of the Bloch Point changes (compare Fig. 4.2 (e) with Fig. 4.3 (b)). More precisely, the out-of-plane magnetisation component m_z field in the vicinity of BP is changed so that for the upper half of BP $m_z > 0$, whereas in the lower half $m_z < 0$.

In this study, there can be several different factors which could affect the direction of Bloch point propagation in the skyrmionic core reversal process. Firstly, the finite

element mesh used to model the disk sample geometry is generated so that the only condition in mesh generation is that the distance between two neighbouring mesh nodes is always less than $l_{\max} = 3\,\mathrm{nm}$. This means that in mesh generation no regularity or symmetry in the mesh structure is guaranteed. Secondly, using different Gilbert damping values and relaxing the system with the same stopping criteria would also result in somewhat different relaxed configurations. Both of them are within acceptable tolerances, but their subtle difference could be the cause of what path in the energy landscape the system is going to take and, consequently, in what direction Bloch point is going to propagate.

4.4 Summary

Because in the previous chapter we demonstrated that skyrmionic states (incomplete and isolated skyrmions) are the ground states in helimagnetic nanostructures at zero external magnetic field, it is expected that two energetically equivalent states with different core orientation exist. Consequently, we studied whether it is possible to change the orientation of the skyrmionic state using an external magnetic field by simulating their hysteretic behaviour. We demonstrated that it is possible to change the orientation using an external magnetic field, which is crucial for data imprint. Since throughout this work we assumed that the simulated material is isotropic, and accordingly, the magnetocrystalline anisotropy is neglected, one might expect that the hysteretic behaviour is a consequence of demagnetisation-based shape anisotropy. However, when we repeated the hysteresis simulations in absence of demagnetisation energy contribution, the presence of hysteretic behaviour remains, which suggests the existence of novel Dzyaloshinskii-Moriya based shape anisotropy. Finally, we explore the reversal mechanism of skyrmionic states and show that it occurs via Bloch point occurrence and propagation. The direction of Bloch point propagation is stochastic and strongly depends on the simulation parameters, which we showed by repeating the reversal simulations with increased Gilbert damping parameter. In addition, we discuss how the finite element mesh asymmetry and different relaxed state configurations could be the cause of different Bloch point propagation direction. Further discussion of the hysteretic behaviour and reversal mechanism of skyrmionic states can be found in Chapter 6.

Chapter 5

Dynamics

In Chapter 3, a systematic study of equilibrium states in confined helimagnetic nanostructures demonstrated that skyrmionic states, in the form of incomplete and isolated skyrmion states, can be the ground state in absence of both external magnetic field and magnetocrystalline anisotropy, whereas the higher order target skyrmionic configuration emerges as a metastable state. An understanding of dynamic properties of skyrmionic states in confined helimagnetic nanostructures is of importance both from the aspect of fundamental physics as well as for their manipulation. In this chapter, we study the dynamic properties (resonance frequencies and corresponding eigenmodes) of these three skyrmionic equilibrium magnetisation states in thin film FeGe disk samples. We employ two different methods in finite-element based micromagnetic simulation: eigenvalue and ringdown method. The eigenvalue method allows us to identify all resonance frequencies and corresponding eigenmodes that can exist in the simulated system. However, using a particular experimentally feasible excitation can excite only a limited set of eigenmodes. Because of that, we perform and report ringdown simulations that resemble the experimental setup using both an in-plane and an out-of-plane excitations. In addition, we report the nonlinear dependence of resonance frequencies on the external magnetic bias field and disk sample diameter and report the possible reversal mode of skyrmionic states. We obtain experimentally the FeGe Gilbert damping value and repeat simulations in order to determine what eigenmodes can be expected to be observed in experiments. Finally, we show that neglecting the demagnetisation energy contribution or ignoring the magnetisation variation in the out-of-film direction – although not changing the eigenmodes magnetisation dynamics significantly – changes their resonance frequencies substantially. This systematic work is of interest to both fundamental physics studies and to guide experimental identification of skyrmionic states in confined helimagnetic disks.

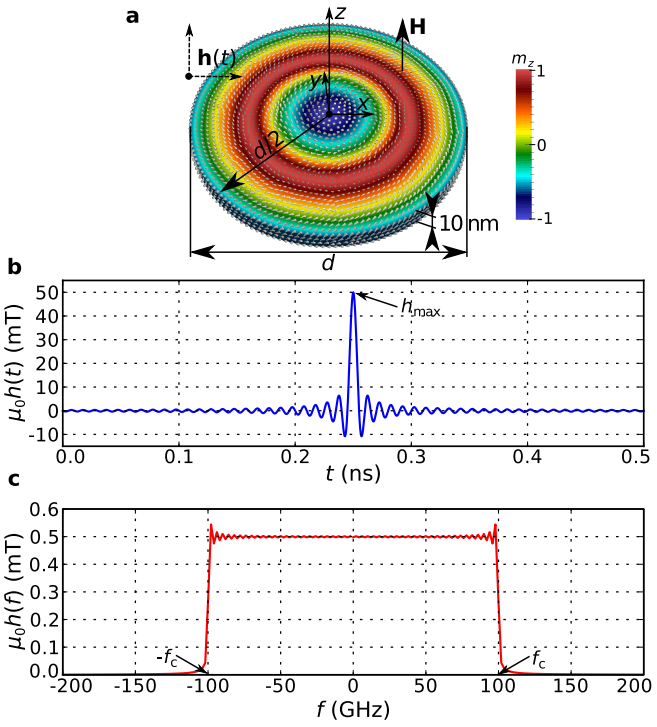

Figure 5.1: (**a**) A thin film FeGe disk sample with 10 nm thickness and diameter d. An external magnetic bias field $\mathbf{H}$ is applied uniformly and perpendicular to the sample (in the positive z direction). (**b**) A "sinc" excitation magnetic field $\mathbf{h}(t)$, used in the ringdown method, is applied for 0.5 ns in either in-plane ($\hat{\mathbf{x}}$) or out-of-plane ($\hat{\mathbf{z}}$) direction. (**c**) The Fourier transform of excitation field $h(t)$ shows that all eigenmodes (allowed by the used excitation direction) with frequencies lower than $f_\mathrm{c} = 100$ GHz are excited approximately equally.

5.1 Methods

5.1.1 Micromagnetic model

We simulate a thin film helimagnetic cubic B20 FeGe disk with 10 nm thickness and diameter d, as shown in Fig. 5.1 (a). The thin film sample is in the xy plane and perpendicular to the z axis. An external magnetic bias field $\mathbf{H}$ is applied uniformly and perpendicular to the sample (in the positive z direction).

The total energy of the system we simulate contains several energy contributions and can be written as

$$E = \int \left[w_\mathrm{ex} + w_\mathrm{dmi} + w_\mathrm{z} + w_\mathrm{d} + w_\mathrm{a} \right] \mathrm{d}^3 r. \tag{5.1}$$

The first term $w_\mathrm{ex} = A\left[(\nabla m_x)^2 + (\nabla m_y)^2 + (\nabla m_z)^2\right]$ is the symmetric exchange energy density with material parameter A. The unit vector field $\mathbf{m} = \mathbf{m}(\mathbf{r}, t)$, with Cartesian components m_x, m_y, and m_z, represents the magnetisation field $\mathbf{M}(\mathbf{r}, t) = M_\mathrm{s}\mathbf{m}(\mathbf{r}, t)$, where M_s is the saturation magnetisation. The second term $w_\mathrm{dmi} = D\mathbf{m} \cdot (\nabla \times \mathbf{m})$ is the Dzyaloshinskii-Moriya energy density with material parameter D, which is obtained

by including Lifshitz invariants suitable for materials of the crystallographic class T, such as the cubic B20 FeGe ($P2_13$ space group) used in this study. The coupling of magnetisation to an external magnetic field $\mathbf{H}$ is defined by the Zeeman energy density term $w_z = -\mu_0 M_s \mathbf{H} \cdot \mathbf{m}$, with μ_0 being the magnetic constant. The w_d term is the demagnetisation (magnetostatic) energy density. Because w_d is crucial for the stability of skyrmionic states in confined helimagnetic nanostructures as we have shown in Sec. 3.6, we include its contribution in all subsequent simulations. The last term is the magnetocrystalline anisotropy energy density w_a, and because it does not play an important role in the stability of skyrmionic states in the studied system, we assume the simulated material is isotropic and neglect the magnetocrystalline anisotropy energy contribution. The FeGe material parameters we use are: saturation magnetisation $M_s = 384\,\mathrm{kA\,m^{-1}}$, exchange energy constant $A = 8.78\,\mathrm{pJ\,m^{-1}}$, and Dzyaloshinskii-Moriya energy constant $D = 1.58\,\mathrm{mJ\,m^{-2}}$. The estimation of FeGe material parameters can be found in Sec. 3.1.2. In our model, we do not assume any translational invariance of magnetisation in the out-of-film direction which significantly changes the energy landscape both in infinitely large thin films [40] and in confined thin film nanostructures. The relevant lengthscales in the simulated system are: exchange length $l_{ex} = \sqrt{2A/\mu_0 M_s^2} = 9.73\,\mathrm{nm}$ and helical length $L_D = 4\pi A/D = 70\,\mathrm{nm}$. Consequently, we choose the finite element mesh discretisation so that the maximum spacing between two neighbouring mesh nodes is below $l_{max} = 3\,\mathrm{nm}$.

The magnetisation dynamics is governed by the Landau-Lifshitz-Gilbert (LLG) equation [78, 79]

$$\frac{\partial \mathbf{m}}{\partial t} = -\gamma_0^* \mathbf{m} \times \mathbf{H}_{\mathrm{eff}} + \alpha \mathbf{m} \times \frac{\partial \mathbf{m}}{\partial t}, \tag{5.2}$$

where $\gamma_0^* = \gamma_0(1+\alpha^2)$, with $\gamma_0 = 2.21 \times 10^5\,\mathrm{m\,A^{-1}s^{-1}}$ and $\alpha \geq 0$ is the Gilbert damping. We compute the effective magnetic field $\mathbf{H}_{\mathrm{eff}}$ using

$$\mathbf{H}_{\mathrm{eff}} = -\frac{1}{\mu_0 M_s} \frac{\delta E[\mathbf{m}]}{\delta \mathbf{m}}, \tag{5.3}$$

where $E[\mathbf{m}]$ is the total energy density functional, given by Eq. (5.1). We validated the boundary conditions by running a series of simulations and reproducing the results reported by Rohart and Thiaville [41].

5.1.2 Dynamics simulations

We study the dynamic properties of skyrmionic states using two different methods: eigenvalue method [59] and ringdown method [60]. In both eigenvalue and ringdown methods, we firstly compute an equilibrium magnetisation configuration $\mathbf{m}_0$ by integrating a set of dissipative time-dependent equations, starting from a specific initial magnetisation configuration, until the condition of minimum torque ($\mathbf{m} \times \mathbf{H}_{\mathrm{eff}}$) is satisfied. The details on selecting the initial magnetisation configurations can be found

in Sec. 3.2. We perform all relaxations in this work down to the maximum precision limited by the unavoidable numerical noise. Because the magnetisation dynamics is not of interest in the relaxation process, we set the Gilbert damping in this stage to $\alpha = 1$.

5.1.2.1 Eigenvalue method

We perform the eigenvalue method computations in a finite element framework, motivated by the analytic procedure implemented using finite difference method by d'Aquino et al. [59] The perturbation of system's magnetisation from its equilibrium state $\mathbf{m}_0$ can be written as $\mathbf{m}(t) = \mathbf{m}_0 + \varepsilon\mathbf{v}(t)$, where $\varepsilon > 0$ and $\mathbf{v}(t) \perp \mathbf{m}_0$ because of the imposed micromagnetic condition $|\mathbf{m}| = 1$. If this perturbation expression is inserted into the undamped LLG equation, we obtain

$$\frac{\partial}{\partial t}(\mathbf{m}_0 + \varepsilon\mathbf{v}(t)) = -\gamma_0^*(\mathbf{m}_0 + \varepsilon\mathbf{v}(t)) \times \mathbf{H}_{\text{eff}}(\mathbf{m}_0 + \varepsilon\mathbf{v}(t)). \tag{5.4}$$

Now, by expanding $\mathbf{H}_{\text{eff}}(\mathbf{m}_0 + \varepsilon\mathbf{v}(t)) = \mathbf{H}_0 + \varepsilon\mathbf{H}'_{\text{eff}}(\mathbf{m}_0) \cdot \mathbf{v}(t) + \mathcal{O}(\varepsilon^2)$, where $\mathbf{H}_0 = \mathbf{H}_{\text{eff}}(\mathbf{m}_0)$, and knowing that $\partial\mathbf{m}_0/\partial t = 0$ and $\mathbf{m}_0 \times \mathbf{H}_0 = 0$, we get

$$\frac{\partial}{\partial t}\mathbf{v}(t) = -\gamma_0^* \left[\mathbf{v}(t) \times \mathbf{H}_0 + \mathbf{m}_0 \times (\mathbf{H}'_{\text{eff}}(\mathbf{m}_0) \cdot \mathbf{v}(t))\right], \tag{5.5}$$

where all $\mathcal{O}(\varepsilon^2)$ terms and higher are neglected. When the system is in its equilibrium, because $\mathbf{H}_{\text{eff}}(\mathbf{m}_0) \parallel \mathbf{m}_0$ and $|\mathbf{m}_0| = 1$, the equilibrium effective field can be written as $\mathbf{H}_0 = h_0\mathbf{m}_0$, where $h_0 = |\mathbf{H}_0|$. Now, if all vector fields are discretised on the finite elements mesh, Eq. (5.5) becomes

$$\frac{\partial}{\partial t}\mathbf{v}(t) = \gamma_0^*\mathbf{m}_0 \times \left[(h_0\mathbb{1} - \mathbf{H}'_{\text{eff}}(\mathbf{m}_0)) \cdot \mathbf{v}(t)\right]. \tag{5.6}$$

Using the matrix $\Lambda(\mathbf{m}_0)$ with property $\mathbf{m}_0 \times \mathbf{x} = \Lambda(\mathbf{m}_0) \cdot \mathbf{x}$, Eq. (5.6) can be written as

$$\frac{\partial}{\partial t}\mathbf{v}(t) = A \cdot \mathbf{v}(t), \tag{5.7}$$

where $A = \gamma_0^*\Lambda(\mathbf{m}_0)\left[h_0\mathbb{1} - \mathbf{H}'_{\text{eff}}(\mathbf{m}_0)\right]$. This linear differential equation has a full set of solutions that can be expressed as $\mathbf{v}(t) = \tilde{\mathbf{v}}\mathrm{e}^{i2\pi ft}$. Using this ansatz, Eq. (5.7) becomes the eigenvalue problem

$$i2\pi f\tilde{\mathbf{v}} = A\tilde{\mathbf{v}}. \tag{5.8}$$

We solve this eigenvalue problem using the SciPy [118, 119] package, which results in the set of resonant frequencies f and eigenvectors $\tilde{\mathbf{v}}$ from which we express the magnetisation dynamics as $\mathbf{m}(t) = \mathbf{m}_0 + \tilde{\mathbf{v}}\mathrm{e}^{i2\pi ft}$.

5.1.2.2 Ringdown method

In the ringdown method, similar to the eigenvalue method, we firstly relax the system to its equilibrium magnetisation state $\mathbf{m}_0$. After that, we perturb the system from its equilibrium by applying a time-dependent $\mathbf{h}(t) = h_{\max}\,\mathrm{sinc}(2\pi f_c t)\hat{\mathbf{e}}$ external magnetic field excitation [49, 120] over $t_{\mathrm{exc}} = 0.5\,\mathrm{ns}$, where $h_{\max}$ is the maximum excitation field value, $f_c = 100\,\mathrm{GHz}$ is the cut-off frequency, $\hat{\mathbf{e}}$ is the direction in which the excitation is applied, and $\mathrm{sinc}(2\pi f_c t)$ is the unnormalised cardinal sine function

$$\mathrm{sinc}(2\pi f_c t) = \begin{cases} \frac{\sin(2\pi f_c t)}{2\pi f_c t}, & \text{for } t \neq 0 \\ 1, & \text{for } t = 0. \end{cases} \tag{5.9}$$

The time-dependence of the used excitation $h(t)$ is shown in Fig. 5.1 (b). Computing the Fourier transform of $h(t)$ shows that using this excitation enables us to excite all eigenmodes (which are allowed by the direction of excitation $\hat{\mathbf{e}}$) in the $[0, f_c]$ range approximately equally, as demonstrated in Fig. 5.1 (c). We compute the $h_{\max}$ value so that $H^f = 0.5\,\mathrm{mT}$ is the excitation amplitude at any frequency. [49] More precisely, the maximum value of the cardinal sine wave excitation is $h_{\max} = 2 f_c t_{\mathrm{exc}} H^f = 50\,\mathrm{mT}$. We apply the excitation in two experimentally feasible directions: (i) in-plane $\hat{\mathbf{e}} = \hat{\mathbf{x}}$ and (ii) out-of-plane $\hat{\mathbf{e}} = \hat{\mathbf{z}}$. After the system is perturbed from its equilibrium state, we simulate the magnetisation dynamics for $t_{\mathrm{sim}} = 20\,\mathrm{ns}$ and sample the magnetisation field $\mathbf{m}(\mathbf{r}_i, t_j)$ at all mesh nodes $\mathbf{r}_i$ at uniform time steps $t_j = j\Delta t$ ($\Delta t = 5\,\mathrm{ps}$). Although the excitation is sufficiently small so that the perturbation from the equilibrium state can be approximated linearly, in order to make sure we do not introduce any nonlinearities to the system's dynamics with excitation, we delay sampling by 2 ns after the excitation field is removed.

Finally, we analyse the recorded magnetisation dynamics $\mathbf{m}(\mathbf{r}_i, t_j)$ using: (i) spatially averaged and (ii) spatially resolved methods [121]. We subtract the time-independent equilibrium magnetisation configuration $\mathbf{m}_0(\mathbf{r}_i)$ from the recorded magnetisation dynamics and perform the Fourier analysis only on the time-dependent part $\Delta\mathbf{m}(\mathbf{r}_i, t_j) = \mathbf{m}(\mathbf{r}_i, t_j) - \mathbf{m}_0(\mathbf{r}_i)$. In the spatially averaged analysis, we compute all three spatially averaged magnetisation components $\langle \Delta m_k(t_j) \rangle$, $k = x, y, z$ at all time steps t_j. After that, we apply a discrete Fourier transform and sum their squared Fourier coefficient moduli (which are proportional to power) to obtain the Power Spectral Density (PSD):

$$P_{\mathrm{sa}}(f) = \sum_{k=x,y,z} \Big| \sum_{j=1}^{n} \langle \Delta m_k(t_j) \rangle \, \mathrm{e}^{-i2\pi f t_j} \Big|^2, \tag{5.10}$$

where n is the number of time steps at which the magnetisation dynamics was sampled. On the other hand, in the spatially resolved analysis, we firstly compute the discrete Fourier transform at all mesh nodes (separately for all three magnetisation components)

and then compute the PSD as the spatial average of squared Fourier coefficient moduli [60]:

$$P_{\mathrm{sr}}(f) = \sum_{k=x,y,z} \frac{1}{N} \sum_{i=1}^{N} \Big| \sum_{j=1}^{n} m_k(\mathbf{r}_i, t_j) e^{-i2\pi f t_j} \Big|^2, \tag{5.11}$$

where N is the number of finite element mesh nodes. Because the power values in PSD are in arbitrary units (a.u.), we normalise all PSDs in this work so that $\int_0^{f_{\max}} P(f)\,\mathrm{d}f = 1$, where $f_{\max} = 50\,\mathrm{GHz}$, and show them in the logarithmic scale. Although, the frequency resolution in the eigenvalue method is determined by the machine precision, the frequency resolution for the ringdown method is $\Delta f = (n\Delta t)^{-1} \approx {t_{\mathrm{sim}}}^{-1} = 0.05\,\mathrm{GHz}$, where $n = t_{\mathrm{sim}}/\Delta t + 1$ is the number of sampling points during the sampling simulation stage.

We normalise and show only the first half $[0, 50\,\mathrm{GHz}]$ of the Power Spectral Density (PSD) frequency range in order to avoid the presence of artefact peaks in PSDs for frequencies higher than 100 GHz, due to the aliasing effect [122] as a consequence of discrete time sampling limitations. In order to illustrate this effect, let us define a simple periodic signal as

$$s(t) = \sin(2\pi f t), \tag{5.12}$$

with f being its frequency. We vary the signal's frequency between 0 GHz and 200 GHz in steps of $\Delta f = 0.5\,\mathrm{GHz}$ and keep the sampling period to be 5 ps at any frequency f. The sampling frequency $f_{\mathrm{s}} = (\Delta t)^{-1} = 200\,\mathrm{GHz}$ implies that in the Fourier transform we expect not to observe any harmonics above the Nyquist frequency $f_{\mathrm{N}} = f_{\mathrm{s}}/2 = 100\,\mathrm{GHz}$. Now, we compute a discrete Fourier transform of the signal $s(t)$ at all frequencies and show a Fourier transform dependence on signal's frequency f in Fig. 5.2. Although we did not expect to observe any peaks in Fourier transforms for signal frequencies $f > f_{\mathrm{N}}$, we observe them at

$$f_{\mathrm{peak}} = \begin{cases} f, & \text{for } f \leq f_{\mathrm{N}} \\ 2f_{\mathrm{N}} - f, & \text{for } f > f_{\mathrm{N}}. \end{cases} \tag{5.13}$$

Therefore, in order to avoid the artefact peaks in PSDs caused by the aliasing of frequencies larger than f_{N}, we limit our analysis of skyrmionic states dynamics to $[0, f_{\mathrm{N}}/2]$ range. As an alternative, we could have limited the cut-off frequency f_{c} of cardinal sine wave excitation defined in the main text to be 50 GHz, but this would introduce irregular excitations at the frequency band edges due to the limited excitation duration.

Although we base this study on the specific helimagnetic material FeGe, in order to make this study relevant to any helimagnetic material, we need to determine as many as possible resonance frequencies that can be detected using a specific excitation. Because of that we need to reduce the linewidth and allow sufficient separation between peaks in the power spectral density (computed from the ringdown method). Consequently, in the first part of this work, we use the Gilbert damping [49] $\alpha' = 0.002$. After we identify all resonance frequencies and corresponding eigenmodes using α', we experimentally

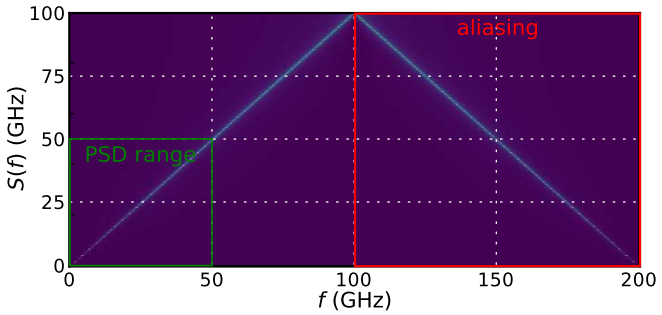

Figure 5.2: The dependence of Fourier transform on signal's frequency for a simple periodic signal $s(t) = \sin(2\pi f t)$ with varying frequency f between 0 GHz and 200 GHz in steps of $\Delta f = 0.5$ GHz, illustrating the aliasing of harmonics above the Nyquist frequency $f_{\mathrm{N}} = 100$ GHz.

measure the real value of FeGe Gilbert damping and use it to determine which (out of all previously identified eigenmodes) can be experimentally detected in the FeGe sample.

5.2 Dynamics of skyrmionic states

We study the dynamics of all three equilibrium skyrmionic states that can be observed at zero external magnetic field in confined thin film helimagnetic disk samples with diameters $d \leq 180$ nm. More precisely, we explore the resonance frequencies and corresponding eigenmode magnetisation dynamics of ground state incomplete Skyrmion (iSk) and isolated Skyrmion (Sk) states, as well as the metastable Target (T) configuration. The difference between these states is in how many times the magnetisation configuration covers the sphere, and consequently, the scalar value S_{a}.

Using the eigenvalue method, we find all existing eigenmodes by computing their resonance frequencies and magnetisation dynamics. However, this method does not allow us to determine what eigenmodes can be excited using a particular excitation. Therefore, we employ the ringdown method for an in-plane and an out-of-plane excitation and overlay the resulting spatially averaged and spatially resolved Power Spectral Densities (PSDs) with the resonance frequencies obtained from the eigenvalue method. If the eigenvalue method resonance frequency coincides with the PSD peak, this implies that the corresponding eigenmode can be "activated" using a specific excitation and we mark it using a triangle ($\triangle$) symbol. All other eigenmodes, that cannot be activated using a particular excitation, we mark with a circle ($\circ$) symbol. Throughout this work, we study the magnetisation dynamics below 50 GHz.

5.2.1 Incomplete Skyrmion (iSk) state

The first magnetisation configuration that we study is the incomplete Skyrmion (iSk) state. The magnetisation component m_z of the iSk state, along the sample diameter, does not cover the whole $[-1, 1]$ range, which is required for the skyrmion configuration to be present in the sample, and because of that, the scalar value S_a is in the $[0, 1]$ range. In other works, this state is called either the quasi-ferromagnetic [39, 41] or the edged vortex [44, 42] state. The incomplete skyrmion state is in an equilibrium for all studied disk sample diameters $40\,\text{nm} \leq d \leq 180\,\text{nm}$ and at all external magnetic bias field values. We explore the resonance frequencies and corresponding eigenmode magnetisation dynamics in a 80 nm diameter disk sample at zero external magnetic field, where the iSk state is not only in an equilibrium, but is also the ground state (global energy minimum).

Firstly, we compute all existing eigenmodes using the eigenvalue method and show the schematic representations in Appendix A. Then, we excite the system using an in-plane excitation and show the Spatially Averaged (SA) and Spatially Resolved (SR) Power Spectral Densities (PSDs) overlaid with the eigenvalue method resonant frequencies in Fig. 5.3 (a) and (b), respectively. In these two PSDs, we identify five peaks (A, D, E, F, and H) and schematically represent their corresponding eigenmode magnetisation dynamics in Fig. 5.3 (e). The lowest frequency and the most dominant eigenmode A at 2.35 GHz consists of a dislocated incomplete skyrmion state core (where $m_z = 1$) revolving (gyrating) around its equilibrium position in the ClockWise (CW) direction. Schematically, we represent the skyrmionic state core with a circle symbol, together with a directed loop if it gyrates around its equilibrium position. Consequently, we classify the eigenmode A as the gyrotropic (translational) mode. The eigenmode F at 23.04 GHz is the second most dominant eigenmode. Its magnetisation dynamics consists of a ring contour, defined by the constant magnetisation z component distribution, revolving around the sample centre in the CounterClockWise (CCW) direction. This eigenmode is not gyrotropic because the iSk state core remains at its equilibrium position. The eigenmode H at 41.65 GHz, present in both SA and SR PSDs, is composed of the iSk state core together with two m_z contour rings revolving in the CW direction. However, the inner contour revolves out-of-phase with respect to both the outer contour and the iSk state core. Because of that, we depict the inner contour ring using a dashed line and both the iSk state core loop and the outer contour ring using a solid line as a way of visualising the mutually out-of-phase dynamics. The eigenmode D is present only in the SR PSD at 13.83 GHz and consists of the iSk state core and a contour ring revolving in the CW direction, but mutually out-of-phase. So far, all identified eigenmodes are lateral, but in the SA PSD at 14.49 GHz, we also identify a very weak eigenmode E with radially symmetric magnetisation dynamics. Although we expect that all eigenmodes present in SA PSD are also present in SR PSD, this is not the case for eigenmode E. We believe this is the case because this breathing eigenmode cannot be excited with

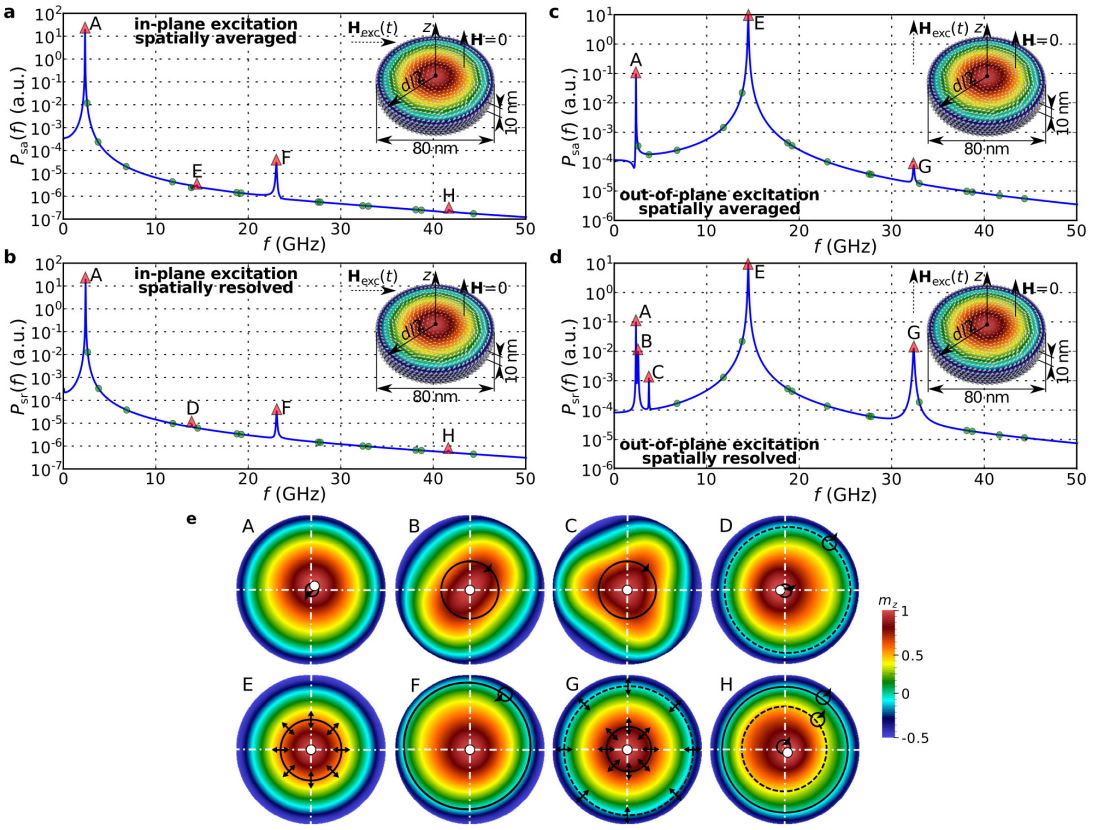

Figure 5.3: The Power Spectral Densities (PSDs) of an incomplete Skyrmion (iSk) ground state at zero external magnetic field in a 80 nm diameter FeGe disk sample with 10 nm thickness. (**a**) Spatially averaged and (**b**) spatially resolved PSDs for an in-plane excitation, together with overlaid resonance frequencies computed using the eigenvalue method. The resonant frequencies obtained using the eigenvalue method are marked with a triangle symbol (△) if they can be activated using a particular excitation and with a circle symbol (○) otherwise. (**c**) Spatially averaged and (**d**) spatially resolved PSDs for an out-of-plane excitation. (**e**) Schematic representations of magnetisation dynamics associated with the identified eigenmodes. Schematically, we represent the skyrmionic state core with a circle symbol, together with a directed loop if it gyrates around its equilibrium position. Contour rings represented using dashed lines revolve/breathe out-of-phase with respect to the those marked with solid lines. The schematic representations of all identified eigenmodes are provided in Appendix A.

an in-plane excitation, but emerges in simulations due to the numerical noise, which is consistent with its small amplitude. This eigenmode, together with other breathing eigenmodes, will be discussed subsequently when we excite the iSk state using an out-of-plane excitation.

Now, we perturb the incomplete skyrmion state from its equilibrium using an out-of-plane excitation and show the Spatially Averaged (SA) and Spatially Resolved (SR) Power Spectral Densities (PSDs) in Fig. 5.3 (c) and Fig. 5.3 (d), respectively. Using this excitation, we identify five eigenmodes (A, B, C, E, and G) and schematically represent their magnetisation dynamics in Fig. 5.3 (e). The most dominant eigenmode E

is present in both SA and SR PSDs at 13.83 GHz. Its magnetisation dynamics consists of a m_z contour ring that shrinks and expands periodically, while the overall magnetisation configuration remains radially symmetric. Because of that, we classify this eigenmode as a breathing mode. The second most dominant eigenmode is the gyrotropic mode A, which was also observed when the system was excited using an in-plane excitation, suggesting that it can be experimentally detected independent of the used excitation direction. The last eigenmode G present in both SA and SR PSDs at 32.37 GHz consists of two contour rings breathing mutually out-of-phase. More precisely, when one contour shrinks, another one expands, and vice versa. We schematically illustrate this out-of-phase breathing using dashed and solid lines depicting the contours. Finally, the eigenmodes B and C, visible only in the SR PSD at 2.57 GHz and 3.76 GHz, respectively, can be understood as a particular magnetisation configuration rotating in the sample in the CW direction without dislocating their core, as shown in Fig. 5.3 (e).

After analysing the incomplete skyrmion power spectral densities for $d = 80\,\text{nm}$ and $H = 0$, we now explore how the resonance frequencies depend on the external magnetic bias field H and the disk sample diameter d for both an in-plane and an out-of-plane excitation. Firstly, we fix the disk sample diameter at 80 nm and vary the external magnetic field between $-0.5\,\text{T}$ and $1.2\,\text{T}$ in steps of 10 mT and show the resulting H-dependent Power Spectral Density (PSD) maps for an in-plane and an out-of-plane excitation in Fig. 5.4 (a) and Fig. 5.4 (b), respectively. In these H-dependent PSD maps, a discontinuity in resonance frequencies at $-0.26\,\text{T}$ is evident. This is the case because for $d = 80\,\text{nm}$ and $-0.26\,\text{T} \leq \mu_0 H \leq 1.2\,\text{T}$, the iSk state with positive ($m_z = 1$) core orientation (iSk↑) is in an equilibrium. However, for $\mu_0 H < -0.26\,\text{T}$, the iSk↑ is not in an equilibrium anymore and the iSk state reverses its orientation to the negative ($m_z = -1$) direction (iSk↓) in order to reduce its Zeeman energy. This is consistent with the incomplete skyrmion hysteretic behaviour study reported in Sec. 4.2. Secondly, we change the disk sample diameter d between 40 nm and 180 nm in steps of 2 nm at zero external magnetic bias field and show in Fig. 5.4 (c) and Fig. 5.4 (d) the d-dependent PSD maps for an in-plane and an out-of-plane excitation, respectively. In PSD maps, we show the spatially resolved PSDs, computed using Eq. (5.11), because in comparison to the spatially averaged PSDs, they exhibit more resonance peaks [60]. We show two plots for every PSD map: one for the complete studied frequency range ($0 - 50\,\text{GHz}$) and another plot in order to better resolve the low-frequency ($0 - 10\,\text{GHz}$) part of the PSD map.

In the case of an in-plane excitation, three lateral eigenmodes (A, D, and F) are visible in the H-dependent PSD map, shown in Fig. 5.4 (a), and in the iSk↑ range their frequencies nonlinearly and monotonically increase with H. Eigenmodes D and F are not as dominant as eigenmode A in the PSD map below approximately 0.3 T, which results in the lack of sufficient contrast for them to be visible. Now, if we change the direction of excitation, five eigenmodes (A, B, C, E, and G) are visible in the H-dependent PSD

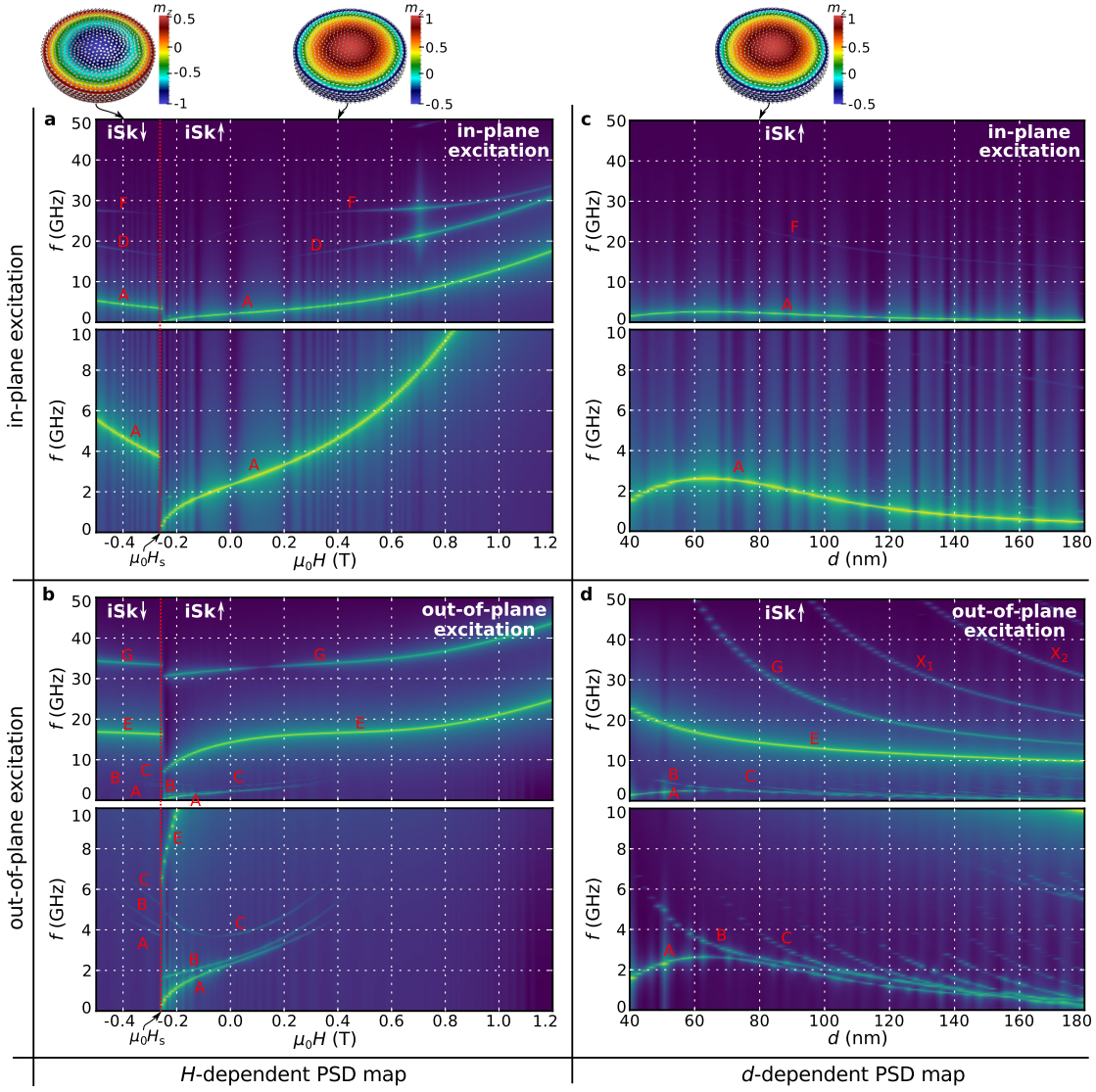

Figure 5.4: Power Spectral Density (PSD) maps showing the dependence of incomplete Skyrmion (iSk) state resonant frequencies on the external magnetic bias field changed between $-0.5\,\mathrm{T}$ and $1.2\,\mathrm{T}$ in steps of $10\,\mathrm{mT}$ for $d = 80\,\mathrm{nm}$ when the system is excited using (**a**) in-plane and (**b**) out-of-plane excitation. The dependence of resonance frequencies on the disk sample diameter varied between $40\,\mathrm{nm}$ and $180\,\mathrm{nm}$ in steps of $2\,\mathrm{nm}$ at zero external magnetic field for (**c**) in-plane and (**d**) out-of-plane excitation. We show two plots for every PSD map: one for the complete studied frequency range ($0 - 50\,\mathrm{GHz}$) and another plot in order to better resolve the low-frequency ($0 - 10\,\mathrm{GHz}$) part of the PSD map.

map, as shown in Fig. 5.4 (b). In the iSk↑ range, eigenmodes A, B, and C are visible only between H_s and approximately 0.4 T. In Fig. 5.3 (d), at zero external magnetic field, eigenmodes A, B, and C have very similar frequencies which makes it difficult for the experimentalists to determine which eigenmode the resonance frequency they measure belongs to. From the out-of-plane H-dependent PSD map in Fig. 5.4 (b), we observe that this can be resolved by reducing the external magnetic field towards the switching field. More precisely, the frequencies of eigenmodes A and B both decrease, but only the frequency of eigenmode A approaches zero. On the other hand, the frequency of eigenmode C increases by reducing external magnetic field. In addition, both increasing and decreasing H improves the separation of these eigenmodes. The dependence of their frequencies at high external magnetic field we show in Fig. 5.5 using the eigenvalue method and demonstrate that no eigenmode crossing occurs. The eigenmodes E and G are visible in the whole examined range of H, and their frequencies increase nonlinearly and monotonically with external magnetic bias field. Interestingly, the frequency of eigenmode A approaches zero near the switching field $\mu_0 H_s = -0.26\,\mathrm{T}$, suggesting that this gyrotropic eigenmode might be the reversal (zero) mode of the incomplete skyrmion state in the studied sample.

By varying the disk sample diameter d, for an in-plane excitation, we observe the gyrotropic eigenmode A frequency increasing between 40 nm and 64 nm (where it reaches its maximum), and then decreasing with d, as shown in Fig. 5.4 (c). Another visible eigenmode in the PSD map above approximately 74 nm, for an in-plane excitation, is the eigenmode F whose frequency monotonically decreases with d. In the case of an out-of-plane excitation, we identify seven (A, B, C, E, G, X_1, and X_2) eigenmodes in the PSD map shown in Fig. 5.4 (d). The magnetisation dynamics of all these eigenmodes was discussed before, except X_1 and X_2, because they were not present in the PSDs below the maximum studied frequency 50 GHz for $d = 80$ nm. The eigenmode A frequency dependence is the same as for an in-plane excitation and another six eigenmodes (B, C, E, G, X_1, and X_2) frequencies monotonically decrease with the disk sample diameter.

For every ringdown simulation in our study, we also carried out the eigenvalue computation. In Power Spectral Density (PSD) maps we discussed, some of the eigenmodes become invisible at certain values of external magnetic field H and disk sample diameter d due to their small amplitude. We show the dependences of incomplete Skyrmion (iSk) resonance frequencies on H and d in Fig. 5.5 (a) and Fig. 5.5 (b), respectively. We represent discrete eigenvalue computed resonance frequencies using a circle (∘) symbol and emphasise the dependences of eigenmodes identified in the main text using a solid line. We find a perfect agreement between eigenvalue and ringdown methods in d and H ranges where eigenmodes are visible in PSD maps.

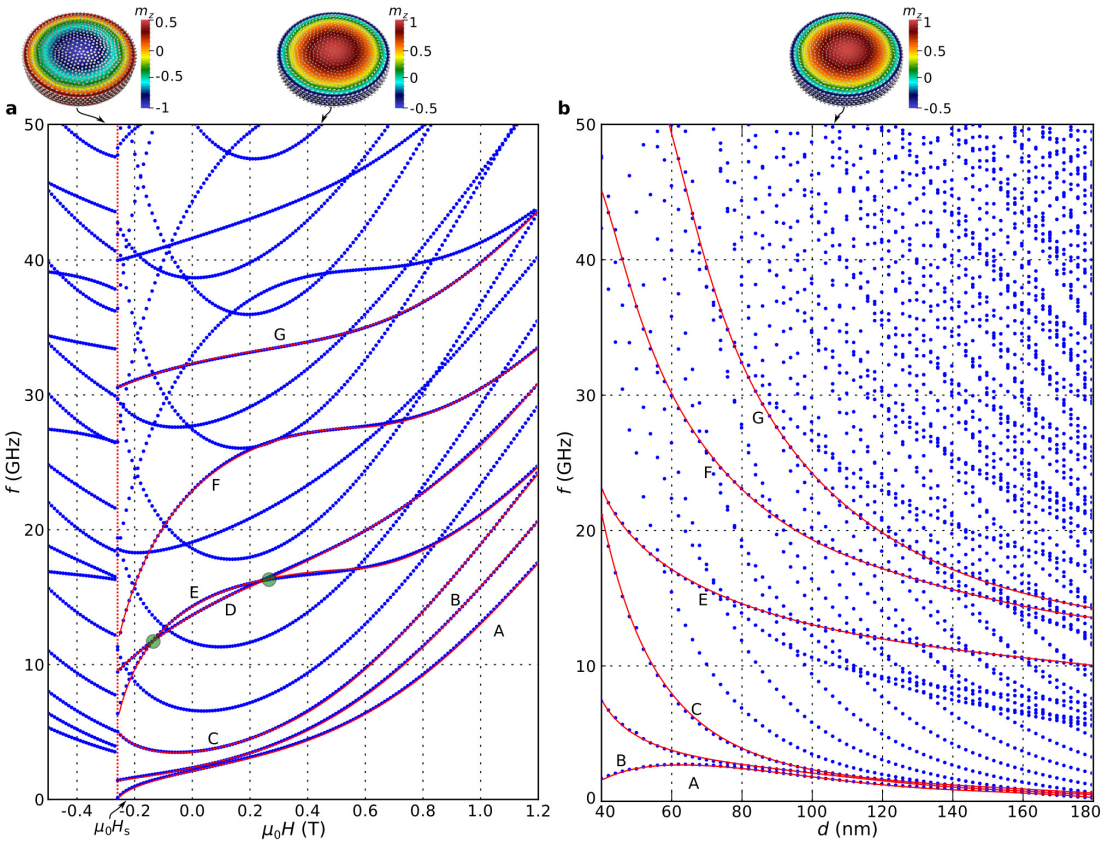

Figure 5.5: The external magnetic field H and disk sample diameter d dependence of incomplete Skyrmion (iSk) state resonance frequencies computed using the eigenvalue method. Discrete eigenvalue computed resonance frequencies are represented using a circle (○) symbol and the dependences of eigenmodes identified in the main text are emphasised using a solid line.

5.2.2 Isolated Skyrmion (Sk) state

In this section, we explore the dynamics of an isolated Skyrmion (Sk) state, for which the magnetisation z component covers the $[-1, 1]$ range once (plus the additional magnetisation tilting at the boundaries due to the specific boundary conditions [41]) along the disk sample diameter, and consequently, the scalar value S_a is in the $[1, 2]$ range. The Sk state is in an equilibrium for $d \geq 70\,\text{nm}$ and $\mu_0 H \leq 1.1\,\text{T}$. We study the Sk state dynamics for a 150 nm diameter disk sample at zero external magnetic bias field, where the Sk state is not only in an equilibrium, but is also the ground state.

After we perform the eigenvalue method computations, we excite the system using an in-plane excitation and show the Spatially Averaged (SA) and Spatially Resolved (SR) Power Spectral Densities (PSDs) in Fig. 5.6 (a) and Fig. 5.6 (b), respectively. The schematic representations of all identified eigenmodes are provided in Appendix A. In both SA and SR PSDs, we identify nine peaks (eigenmodes A, B, D, E, G, I, J, L, and M), and show their schematic representations in Fig. 5.6 (e). The lowest frequency eigenmode

at 0.67 GHz is the gyrotropic eigenmode A. Its magnetisation dynamics consists of a dislocated Sk state core (where $m_z = -1$) gyrating around its equilibrium position in the CCW direction. In both PSDs, the eigenmode B at 1.91 GHz is the most dominant one, and consists of a contour ring (defined as a constant magnetisation z component distribution) revolving in the CW direction. The eigenmode D at 7.61 GHz is composed of both the Sk state core and a magnetisation contour ring revolving in the CCW direction, but mutually out-of-phase. At 14.54 GHz, we identify an eigenmode E with two magnetisation contour rings revolving mutually out-of-phase in the CW direction. Similarly, the eigenmode G at 18.89 GHz also consists of two contour rings revolving mutually out-of-phase, but now in the CCW direction. The four remaining eigenmodes (I, J, L, and M) are significantly weaker in both PSDs when compared to the power of previously discussed eigenmodes. Their magnetisation dynamics, shown in Fig. 5.6 (e), are all lateral and contain different combinations of revolving contour rings and the Sk state core.

Now, we change the excitation to be in the out-of-plane direction. The computed spatially averaged and spatially resolved power spectral densities, overlaid with the resonance frequencies obtained from the eigenvalue method, are shown in Fig. 5.6 (c) and Fig. 5.6 (d), respectively. In this case, we observe five peaks (eigenmodes A, C, F, H, and K) in both PSDs, and a significantly weaker lateral eigenmode G (previously discussed) in SA PSD. We show the schematic representation of their magnetisation dynamics in Fig. 5.6 (e). Similarly to the incomplete skyrmion state, the gyrotropic eigenmode A can also be activated with an out-of-plane excitation. The lowest frequency breathing eigenmode C at 2.00 GHz consists of a single contour ring that shrinks and expands periodically. An eigenmode F at 16.12 GHz is composed of two contour rings breathing mutually out-of-phase. Similarly to the eigenmode C, the eigenmode H at 25.22 GHz consists of a single breathing contour, but now with a smaller contour diameter (larger m_z). At 39.25 GHz, we identify the highest frequency breathing eigenmode K in the studied frequency range, which contains three breathing contours, where the inner and the outer contours breathe out-of-phase with respect to the middle one.

So far, we analysed the isolated skyrmion state dynamics for $d = 150\,\text{nm}$ and $H = 0$. Now, we explore how the resonance frequencies change when H and d are varied. Firstly, we fix the disk sample diameter at $d = 150\,\text{nm}$ and vary the external magnetic bias field between $-0.5\,\text{T}$ and $1.2\,\text{T}$ in steps of $10\,\text{mT}$. We show the H-dependent PSD maps for an in-plane and an out-of-plane excitation in Fig. 5.7 (a) and Fig. 5.7 (b), respectively. In these PSD maps, two discontinuities in resonant frequencies at $-0.24\,\text{T}$ and $1.12\,\text{T}$ are present. The first discontinuity occurs because decreasing H causes the Sk state core with negative ($m_z = -1$) orientation (Sk$\downarrow$) to switch to the positive ($m_z = 1$) direction (Sk$\uparrow$) at the switching field $\mu_0 H_\text{s} = -0.24\,\text{T}$. On the other hand, the discontinuity at $1.12\,\text{T}$ occurs because, above this value, the Sk$\downarrow$ is not in an equilibrium anymore and the system relaxes to the incomplete skyrmion state with positive core orientation

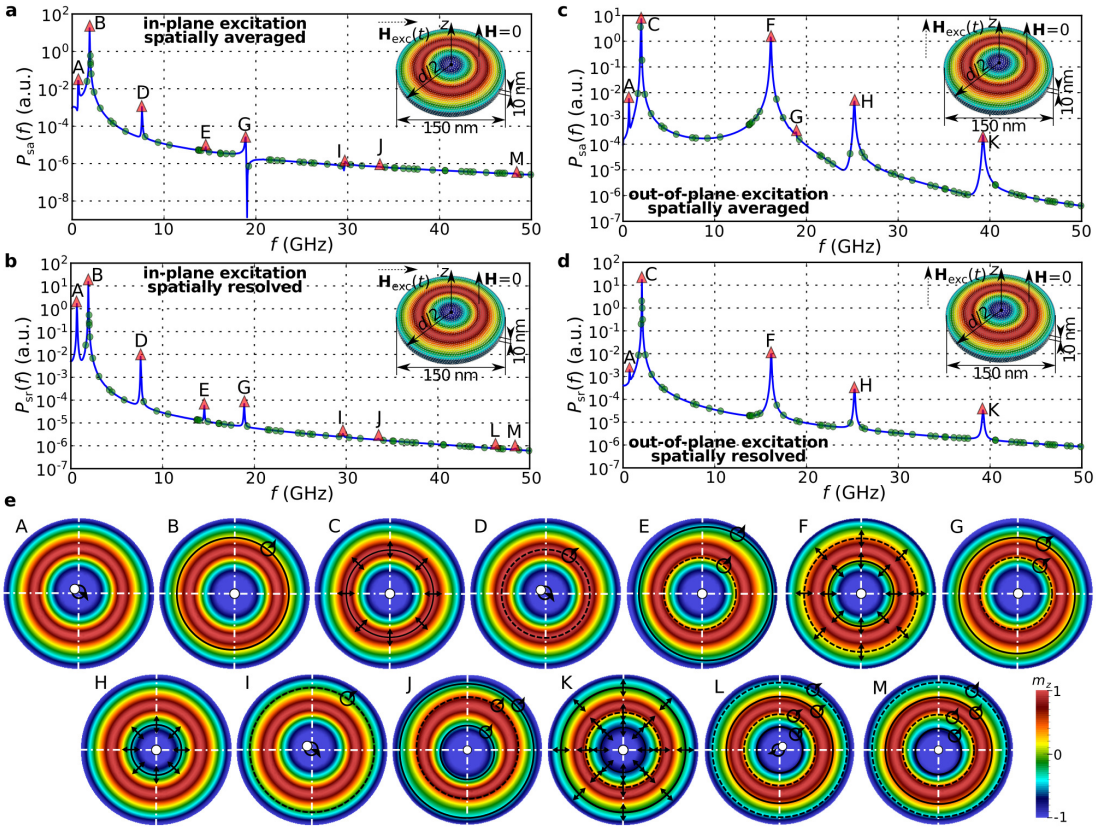

Figure 5.6: The Power Spectral Densities (PSDs) of an isolated Skyrmion (Sk) ground state in a 150 nm diameter FeGe disk sample with 10 nm thickness at zero external magnetic bias field. (**a**) Spatially averaged and (**b**) spatially resolved PSDs for an in-plane excitation, together with overlaid resonance frequencies computed using the eigenvalue method. The resonant frequencies obtained using the eigenvalue method are marked with a triangle symbol (△) if they can be activated using a particular excitation and with a circle symbol (○) otherwise. (**c**) Spatially averaged and (**d**) spatially resolved PSDs computed when the Sk state is perturbed from its equilibrium with an out-of-plane excitation. (**e**) Schematic representations of magnetisation dynamics associated with the identified eigenmodes. Schematically, we represent the skyrmionic state core with a circle symbol, together with a directed loop if it gyrates around its equilibrium position. Contour rings represented using dashed lines revolve/breathe out-of-phase with respect to the those marked with solid lines. The schematic representations of all identified eigenmodes are provided in Appendix A.

(iSk↑). Secondly, at $H = 0$, we vary d between 40 nm and 180 nm in steps of 2 nm and show the d-dependent PSD maps in Fig. 5.7 (c) and Fig. 5.7 (d) for an in-plane and an out-of-plane excitation, respectively. Now, a single discontinuity in resonance frequencies is present at 70 nm, below which the disk sample diameter becomes too small to accommodate the full magnetisation rotation and the iSk state emerges. The external magnetic bias field and disk sample diameter values at which the discontinuities occur are consistent with the equilibrium and hysteretic behaviour studies reported in Sec. 4.2 and Sec. 3.3.

For an in-plane excitation, in the H-dependent PSD map, shown in Fig. 5.7 (a), five previously discussed eigenmodes (A, B, D, E, and G) are visible in the H range where the Sk↓ state is in an equilibrium. The frequency of gyrotropic eigenmode A firstly increases, reaches its maximum at approximately 0.15 T, and then decreases down to its minimum at approximately 0.9 T, after which it keeps increasing with H. In comparison to the other eigenmodes, its frequency varies over a much smaller range (less than 1 GHz) over the entire H range where the Sk↓ state is in an equilibrium. Similar to the incomplete skyrmion state, the frequency of gyrotropic eigenmode A approaches zero near the switching field $\mu_0 H_\mathrm{s} = -0.24\,\mathrm{T}$, suggesting that this eigenmode might govern the isolated skyrmion reversal process. The eigenmode B frequency increases approximately linearly up to 0.6 T, after which it continues increasing nonlinearly. The frequency of eigenmode D, firstly decreases, reaches its minimum at approximately 0.22 T, and then continues increasing nonlinearly with H. The frequencies of eigenmodes E and G exhibit more complicated behaviour where two extremes (maximum and minimum) are present in their H-dependences. When an out-of-plane excitation is used, we observe five previously discussed eigenmodes (A, C, F, H, and J) in the H-dependent PSD map, shown in Fig. 5.7 (b). The eigenmode A now becomes invisible in the PSD map below 0.2 T. The breathing eigenmode C frequency increases monotonically over the entire Sk↓ field range. The frequency dependences of eigenmodes F, H, and J, exhibit more complicated behaviour having both local maximum and minimum in their H-dependences.

In the d-dependent PSD map, shown in Fig. 5.7 (c), obtained when an in-plane excitation is used, five previously discussed eigenmodes (A, B, D, E, and G) are present. In contrast to the frequencies of eigenmodes D, E, and G that monotonically decrease with d over a wide range of frequencies, the eigenmodes A and B frequencies vary in a much smaller (less than 1 GHz) range over entire studied d range. Eigenmodes D, E, and G become invisible in the PSD map below approximately 120 nm. In Fig. 5.7 (d), we show the d-dependent PSD map for an out-of-plane excitation, where five eigenmodes (A, C, F, H, and J) are visible. Similarly to the eigenmodes A and B, the lowest frequency breathing eigenmode frequency changes over a much smaller range than the frequencies of eigenmodes F, H, and J, when the disk sample diameter is changed.

Similar to the incomplete Skyrmion (iSk) state, for every ringdown simulation, we also carried out the eigenvalue computation. Eigenvalue method allows us to determine how

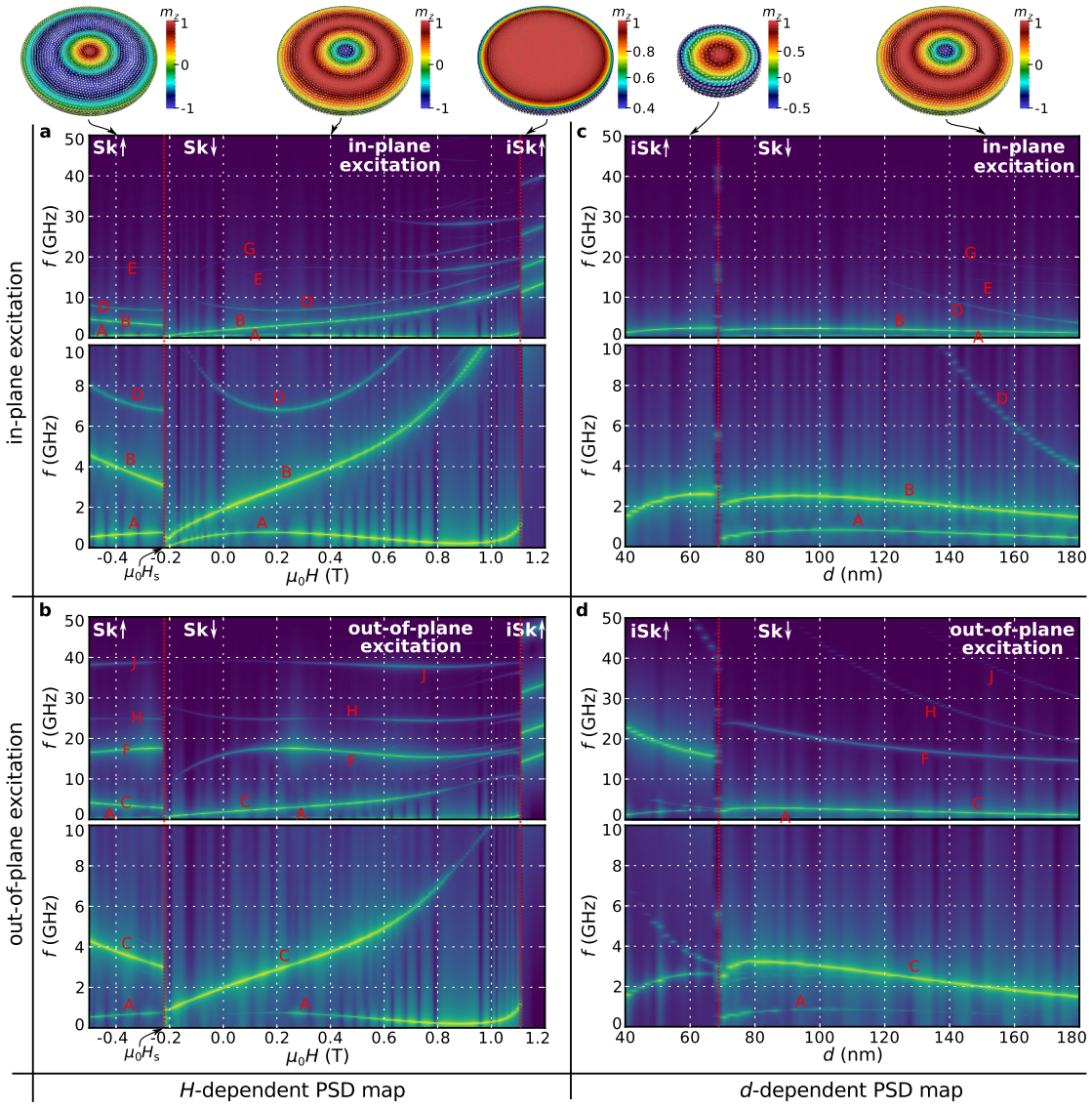

Figure 5.7: Power Spectral Density (PSD) maps showing the dependence of isolated Skyrmion (Sk) state resonant frequencies on the external magnetic bias field changed between $-0.5\,\mathrm{T}$ and $1.2\,\mathrm{T}$ in steps of $10\,\mathrm{mT}$ for $d = 80\,\mathrm{nm}$ when the system is excited using (**a**) in-plane and (**b**) out-of-plane excitation. The dependence of resonance frequencies on the disk sample diameter varied between $40\,\mathrm{nm}$ and $180\,\mathrm{nm}$ in steps of $2\,\mathrm{nm}$ at zero external magnetic field for (**c**) in-plane and (**d**) out-of-plane excitation. We show two plots for every PSD map: one for the complete studied frequency range ($0 - 50\,\mathrm{GHz}$) and another plot in order to better resolve the low-frequency ($0 - 10\,\mathrm{GHz}$) part of the PSD map.

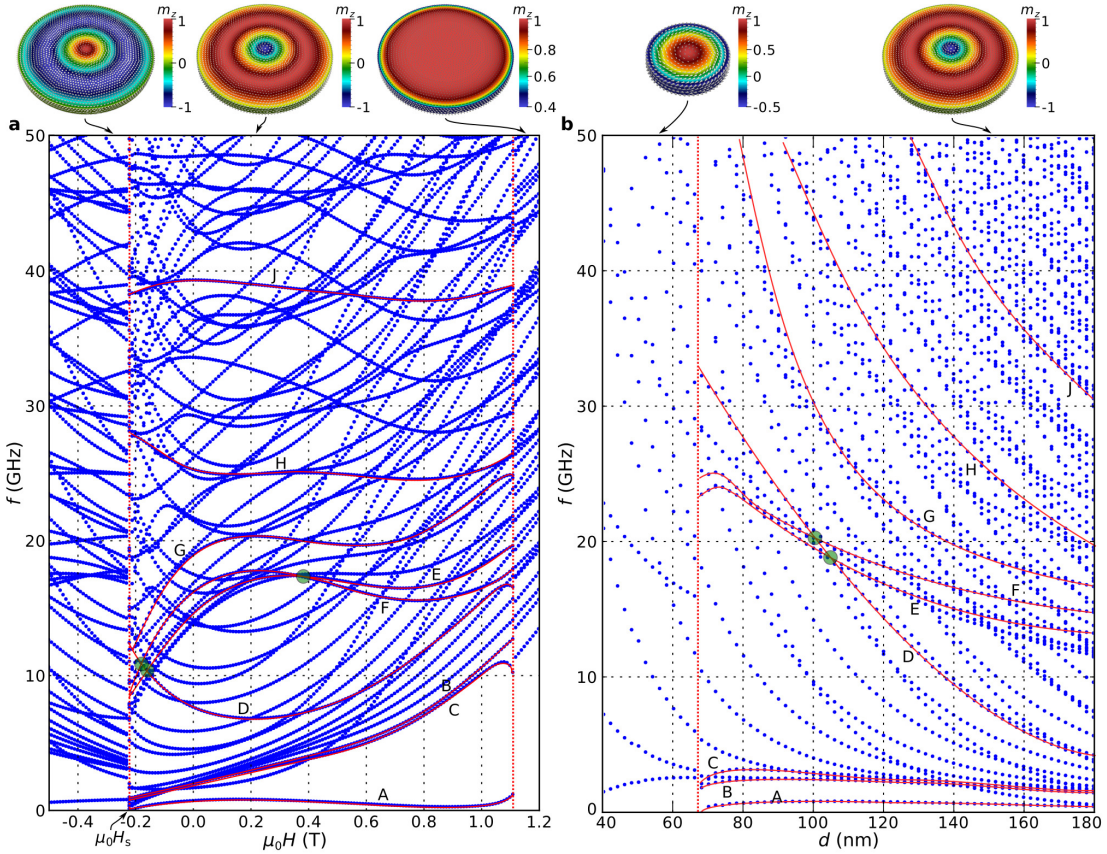

Figure 5.8: The external magnetic field H and disk sample diameter d dependence of isolated Skyrmion (Sk) state resonance frequencies computed using the eigenvalue method. Discrete eigenvalue computed resonance frequencies are represented using a circle (∘) symbol and the dependences of eigenmodes identified in the main text are emphasised using a solid line.

the resonance frequencies of particular eigenmodes change with external magnetic field H and disk sample diameter d over the entire range of studied d and H values. We show the dependences of isolated Skyrmion (Sk) resonance frequencies on H and d in Fig. 5.8 (a) and Fig. 5.8 (b), respectively. We represent discrete eigenvalue computed resonance frequencies using a circle (∘) symbol and emphasise the dependences of eigenmodes identified in the main text using a solid line. We find a perfect agreement between eigenvalue and ringdown methods in d and H ranges where eigenmodes are visible in PSD maps.

5.2.3 Target (T) state

In this section, we study the dynamics of the Target (T) state. This state is characterised by the scalar value S_a being in the $[1, 2]$ range, because the magnetisation component m_z covers the $[-1, 1]$ range twice, plus an additional magnetisation tilting at the boundary due to the specific boundary conditions [41]. Although the T state is never the ground state (global energy minimum) in the studied system, it is in an equilibrium for the

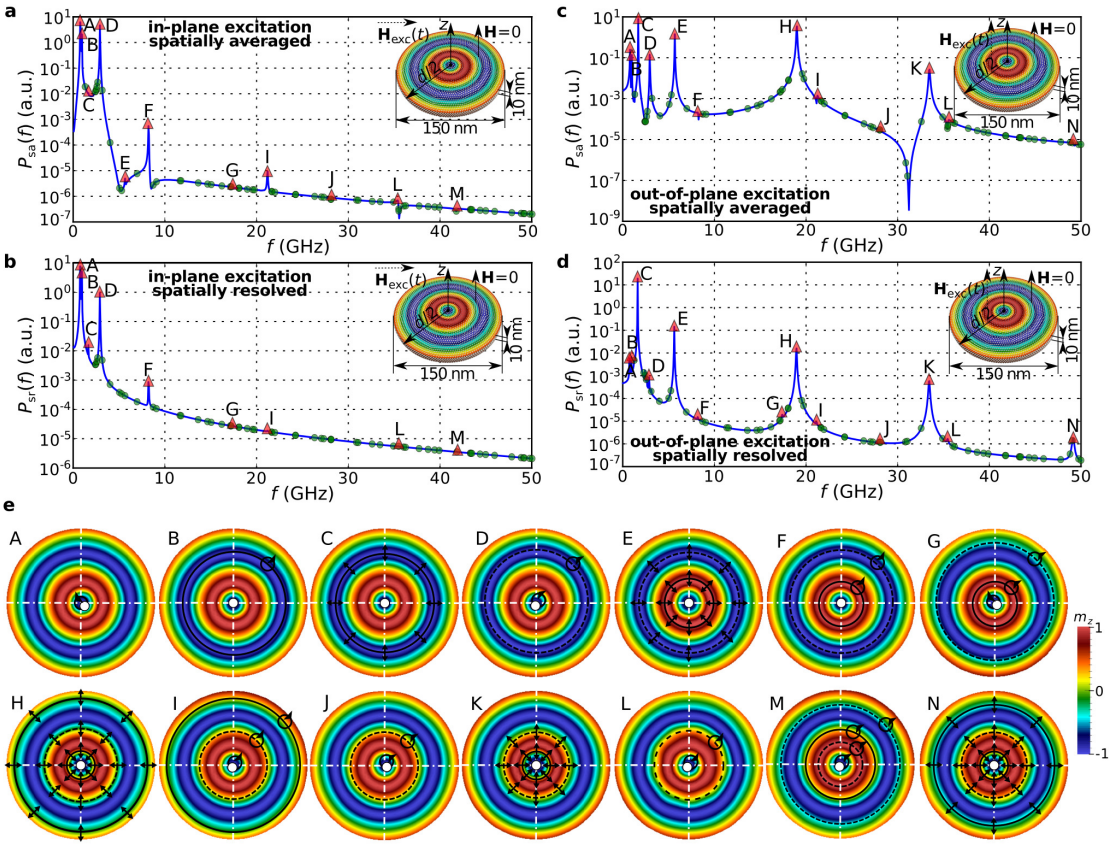

Figure 5.9: The Power Spectral Densities (PSDs) of a Target (T) equilibrium state in a 160 nm diameter FeGe disk sample with 10 nm thickness at zero external magnetic bias field. (**a**) Spatially averaged and (**b**) spatially resolved PSDs for an in-plane excitation, together with overlaid resonance frequencies computed using the eigenvalue method. The resonant frequencies obtained using the eigenvalue method are marked with a triangle symbol (△) if they can be activated using a particular excitation and with a circle symbol (○) otherwise. (**c**) Spatially averaged and (**d**) spatially resolved PSDs computed when the target state is perturbed from its equilibrium with an out-of-plane excitation. (**e**) Schematic representations of magnetisation dynamics associated with the identified eigenmodes. Schematically, we represent the target state core with a circle symbol, together with a directed loop if it gyrates around its equilibrium position. Contour rings represented using dashed lines revolve/breathe out-of-phase with respect to the those marked with solid lines. The schematic representations of all identified eigenmodes are provided in Appendix A.

disk sample diameters 144 nm $\leq d \leq$ 180 nm and the external magnetic bias field $\mu_0 H \leq$ 0.24 T. More precisely, for these d and H values, target state is in the local and not global energy minimum state. We explore the target state dynamics in a 160 nm diameter disk sample with 10 nm thickness at zero external magnetic bias field. In order to obtain the target state in the sample, the magnetisation is initialised with a state having similar configuration as explained in Sec. 3.2.

In the first step, we compute all existing eigenmodes below 50 GHz and show their

schematic representations in Appendix A. Using the ringdown method, we compute the Spatially Averaged (SA) and Spatially Resolved (SR) Power Spectral Densities (PSDs) for an in-plane excitation, overlaid with the eigenvalue results, and show them in Fig. 5.9 (a) and Fig. 5.9 (b), respectively. In these power spectral densities, we observe eleven peaks (eigenmodes A, B, C, D, E, F, G, I, J, L, and M) and show their schematic representations in Fig. 5.9 (e). We identify the two lowest frequency peaks at 0.72 GHz and 0.89 GHz, which correspond to the gyrotropic eigenmode A and lateral eigenmode B, respectively. Similar to the incomplete skyrmion and isolated skyrmion states, the gyrotropic eigenmode A magnetisation dynamics consists of a target state core (where $m_z = -1$) gyrating around its equilibrium position in the CounterClockWise (CCW) direction. The magnetisation dynamics of eigenmode B is composed of a magnetisation z component contour ring revolving in the ClockWise (CW) direction around the sample centre. At 2.86 GHz, we identify another dominant eigenmode D, which consists of a T state core and a contour ring rotating in the CCW direction, but mutually out-of-phase. In the case of the eigenmode F at 8.17 GHz, the T state core is static, but two magnetisation contour rings revolve mutually out-of-phase in the CW direction. The magnetisation dynamics of all other eigenmodes (G, I, J, L, and M) present in the in-plane power spectral densities have significantly lower power. They are all lateral and consist of different combinations of revolving contour rings and the T state core, and we show their schematic representations in Fig. 5.9 (e). All discussed eigenmodes so far are lateral (in-plane), but in the discussed in-plane PSDs, two breathing eigenmodes C and E are also present with significantly lower power and we will discuss them subsequently when an out-of-plane excitation is used to perturb the system.

Now, we excite the system with an out-of-plane excitation, compute the SA and SR PSDs, and show them in Fig. 5.9 (c) and Fig. 5.9 (d), respectively. In this case, we observe five dominant breathing eigenmodes (C, E, H, K, and N) and significantly weaker lateral eigenmodes (A, B, D, F, G, I, J, and L) discussed previously. The lowest frequency breathing eigenmode C at 1.60 GHz contains a single magnetisation z component contour ring that shrinks and expands periodically. Another two dominant peaks in these PSDs correspond to eigenmodes E and H at 5.59 GHz and 18.93 GHz, respectively. The eigenmode E magnetisation dynamics consists of two contour rings breathing mutually out-of-phase. Similarly, the magnetisation dynamics of the eigenmode H consists of three breathing contour rings where the middle contour ring breathes out-of-phase with respect to the inner and the outer one. The eigenmodes K and N magnetisation dynamics consist of different combinations of breathing contours and we show their schematic representations in Fig. 5.9 (e).

5.2.4 Comparison of incomplete skyrmion and isolated skyrmion power spectral densities

One of the challenges in the study of skyrmionic states in confined helimagnetic nanostructures is the detection of what state emerged in the studied sample. In this subsection we discuss how measuring resonance frequencies can contribute to the identification of the emerged state. Previously, in Sections 5.2.1 and 5.2.2, we studied the dynamics of both incomplete Skyrmion (iSk) and isolated Skyrmion (Sk) states in disk samples with diameters for which these states were the ground states. Now, we compare the Power Spectral Densities (PSDs) of iSk and Sk states in a 100 nm diameter disk sample with 10 nm thickness at different external magnetic field values $\mu_0 H$ (between 0 T and 1 T in steps of 0.25 T). In this sample size and at all simulated external magnetic field values, both iSk and Sk states are in equilibrium. More specifically, the Sk state is metastable and the iSk state is the ground state [123]. We show the comparison of spatially resolved iSk and Sk PSDs at different external magnetic field values for an in-plane and an out-of-plane excitation in Fig. 5.10. Because in a 100 nm diameter disk sample there are no dominant iSk and Sk eigenmodes that can be easily detected in experiments above 30 GHz, we now limit our discussion of PSDs below 30 GHz in order to better resolve the key differences, that can contribute to the identification of the present state.

Firstly, in the case of an in-plane excitation (left column in Fig. 5.10), the frequency of iSk gyrotropic eigenmode A (the lowest frequency iSk eigenmode), increases with H. On the contrary, the Sk gyrotropic eigenmode A (again the lowest frequency Sk eigenmode) frequency remains approximately the same. Furthermore, by increasing the external magnetic field the Sk eigenmode B frequency increases, and consequently, the frequency difference between two lowest frequency Sk eigenmodes Δ_{AB} increases in a wide range of frequencies. In contrast, the frequencies of two lowest frequency iSk eigenmodes A and D both increase with H, so that the frequency difference Δ_{AD} between them changes over a small range of frequencies (remains approximately the same). However, at low values of external magnetic field, it could be difficult to measure the iSk eigenmode D due to its relatively small amplitude. In that case, between 0.25 T and 0.75 T, the frequency of dominant iSk eigenmode F does not change, so the $\Delta_{\mathrm{AF}} = \Delta_{\mathrm{AD}} + \Delta_{\mathrm{DF}}$ difference reduces with H for about 5 GHz.

When we excite the system using an out-of-plane excitation (right column in Fig. 5.10), at $H = 0$, several resonance frequencies below 5 GHz are present, which does not allow a clear identification of the emerged state by measuring resonance frequencies in that region. However, by increasing the external magnetic field, the low frequency part of PSDs simplifies. More specifically, the Sk eigenmode A frequency again does not change, while the Sk breathing eigenmode C, and therefore the difference Δ_{AC}, increase with H. In addition, for a Sk state above 0.25 T, the frequency of eigenmode F remains approximately the same, and therefore, the difference Δ_{CF} decreases with H. On the

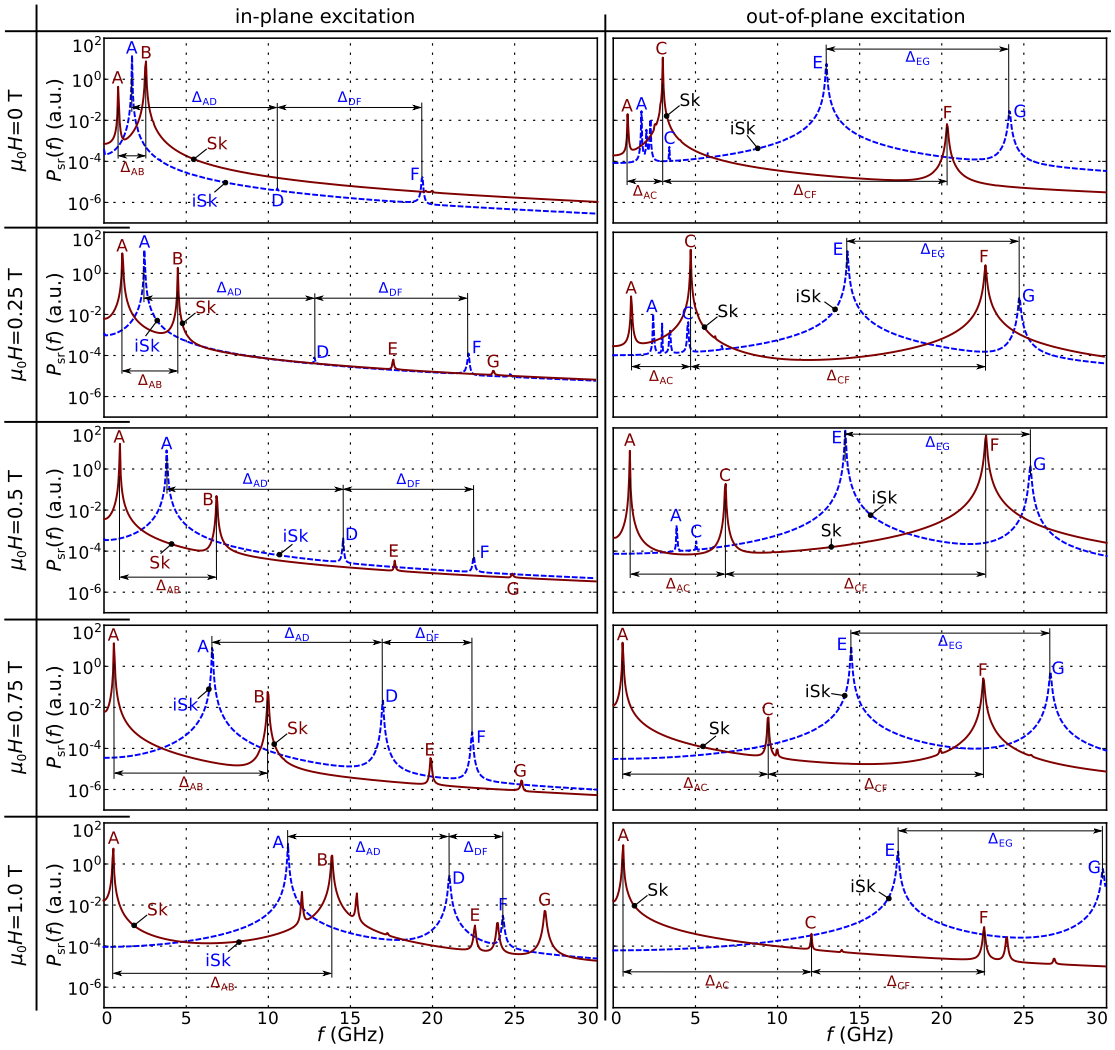

Figure 5.10: Comparisons of Power Spectral Densities (PSDs) of ground incomplete Skyrmion (iSk) state (solid red line) and metastable isolated Skyrmion (Sk) state (dashed blue line) in a 100 nm disk sample with 10 nm thickness at different values of external magnetic field H, computed for an in-plane (left column) and an out-of-plane (right column) excitation.

contrary, iSk eigenmodes A, B, and C disappear from the PSD after $\mu_0 H = 0.5\,\mathrm{T}$, whereas the frequency difference Δ_{EG} between two most dominant iSk eigenmodes E and G remains approximately the same, since their frequencies both increase.

The dependences of resonant frequencies in this sample with $d = 100\,\mathrm{nm}$ are in a good agreement with the PSD maps shown in Fig. 5.4 (a) and Fig. 5.7 (a) and eigenvalue computed results in Supplementary Section S2. This suggests that these identification differences can probably be applied to different sample sizes. At $\mu_0 H = 1\,\mathrm{T}$, we approach the transition from Sk to iSk state and additional peaks in Sk state PSDs, shown in Fig. 5.10, occur.

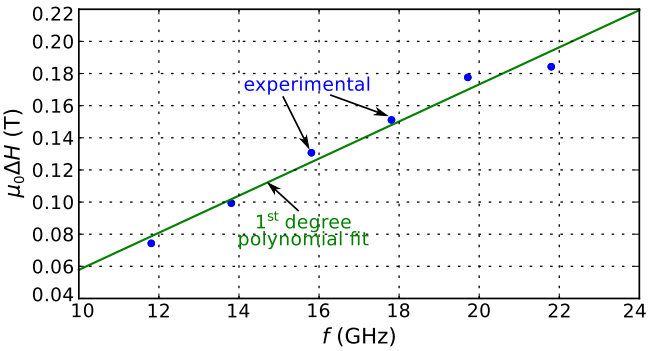

Figure 5.11: The linewidth ΔH (half width at half maximum) measurement points at different resonance frequencies f for a FeGe thin film, together with a first degree polynomial fit from which the Gilbert damping was extracted.

5.3 Simulations with real FeGe damping

In the previous analysis of skyrmionic states dynamics, we intentionally used the small Gilbert damping value $\alpha = 0.002$ as used in other eigenmode studies [49], in order to allow enough separation between peaks in the power spectral densities (enabled by the reduced linewidth) and identify all eigenmodes that can be excited using a particular experimentally feasible excitation. However, in experiments, what eigenmodes can be observed strongly depends on the real value of Gilbert damping. Therefore, in this section, we experimentally measure the FeGe Gilbert damping value α and repeat our simulations in order to determine what eigenmodes are expected to be experimentally observed in helimagnetic FeGe confined nanostructures.

We perform the ferromagnetic resonance measurements[1] in a FeGe thin film with 67.8 ± 0.1 nm thickness, grown on the Si substrate in the (111) direction and capped with a 4.77 ± 0.07 nm thin Ge layer. We show the linewidth ΔH (half width at half maximum) measurement points at different resonance frequencies f, together with a first degree polynomial fit in Fig. 5.11. The polynomial fit allows us to decompose the ΔH dependence into a frequency independent inhomogeneously-broadened component ΔH_0 and an intrinsic damping-related part [124, 125, 126]:

$$\Delta H = \Delta H_0 + \frac{\alpha f}{\gamma}, \tag{5.14}$$

where α is the Gilbert damping and γ is the gyromagnetic ratio. From the slope of the polynomial fit and using the frequency-dependent term that reflects the "viscous" damping of the precessive magnetisation motion associated with the FMR, we find $\alpha = 0.28 \pm 0.02$.

[1] Ferromagnetic resonance measurements and estimation of Gilbert damping were performed by Charles S. Spencer and Christopher H. Marrows (University of Leeds) together with Chiara Ciccarelli and Andrew J. Ferguson (University of Cambridge).

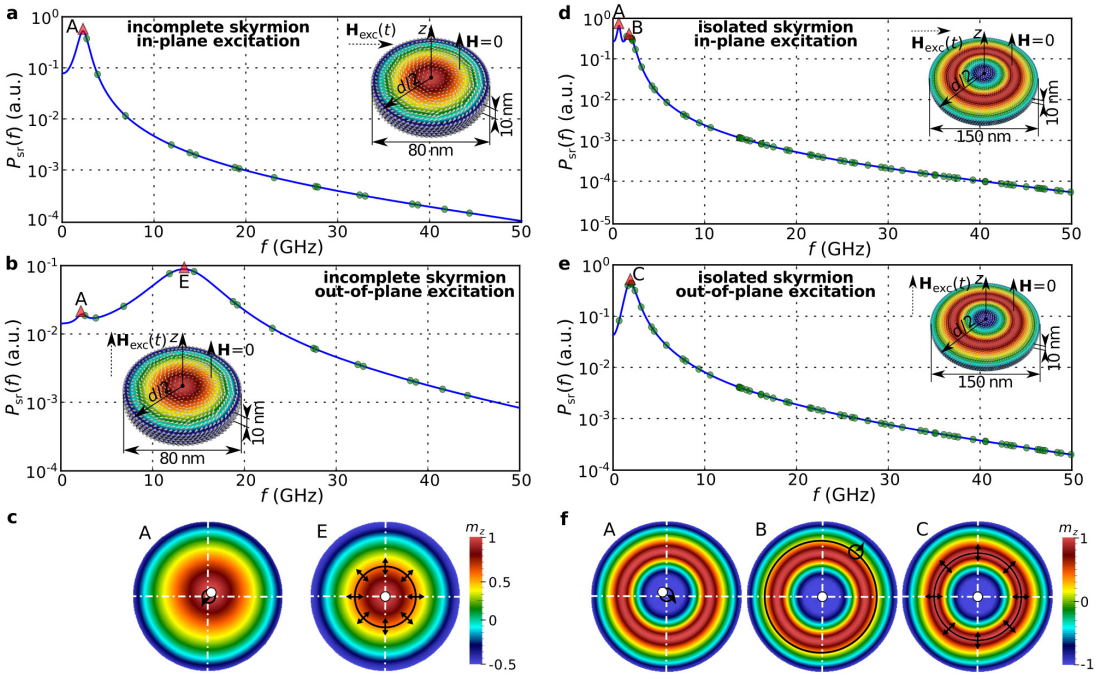

Figure 5.12: The spatially resolved Power Spectral Densities (PSDs) of an incomplete skyrmion state in a 80 nm diameter FeGe disk sample with 10 nm thickness at zero external magnetic bias field for (**a**) in-plane and (**b**) out-of-plane excitation direction. The isolated skyrmion state in a 150 nm diameter thin film disk with 10 nm thickness at $H = 0$ when the system is excited with (**c**) in-plane and (**d**) out-of-plane excitation. The PSDs are computed using the experimentally measured value of FeGe Gilbert damping $\alpha = 0.28$.

Now, we use the measured $\alpha = 0.28$ and repeat the ringdown simulations for the two skyrmionic ground states that can exist in the studied system. We show the spatially resolved power spectral density of an incomplete skyrmion state in a 80 nm diameter disk sample at zero external magnetic bias field for an in-plane and an out-of-plane excitation in Fig. 5.12 (a) and Fig. 5.12 (b), respectively. We observe that, when the system is excited using an in-plane excitation, only the gyrotropic eigenmode A is present in the PSD. On the other hand, for an out-of-plane excitation, we identify two eigenmodes in the PSD shown in Fig. 5.12 (b). The first one is the gyrotropic eigenmode A, which is also present in the in-plane PSD, and another one is the lowest frequency breathing eigenmode E. The PSDs of the isolated skyrmion state in a 150 nm diameter disk sample at zero external magnetic bias field are shown in Fig. 5.12 (c) and Fig. 5.12 (d) for an in-plane and an out-of-plane excitation, respectively. Now, only the three lowest frequency isolated skyrmion eigenmodes are present. The gyrotropic eigenmode A and eigenmode B can be identified when the system is excited using an in-plane excitation. On the other hand, for the out-of-plane excitation, only the breathing eigenmode C is present.

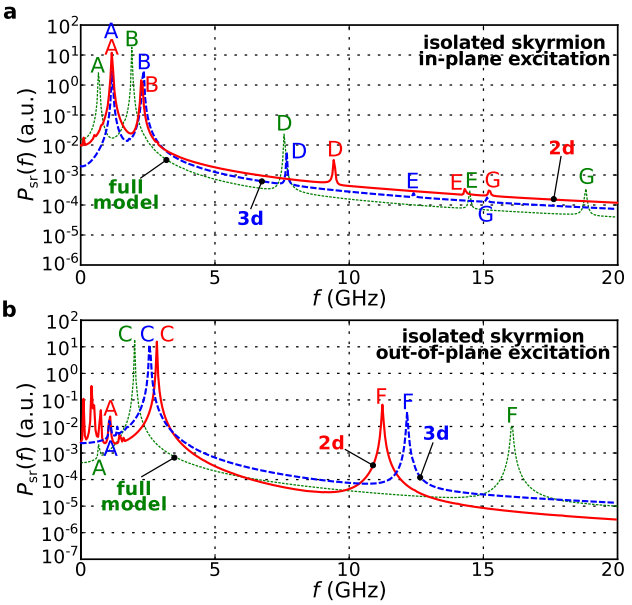

Figure 5.13: The comparison of power spectral densities computed using 3d and 2d models in absence of demagnetisation energy contribution with the PSD obtained using a full simulation model for an isolated skyrmion state in the case of (**a**) in-plane and (**b**) out-of-plane excitation. Simulated sample is a 150 nm diameter disk with 10 nm thickness at zero external magnetic field.

5.4 Demagnetisation energy and out-of-plane magnetisation variation effects

Usually, in the simulations of skyrmionic states dynamics in helimagnetic samples, for simplicity, the demagnetisation energy contribution is neglected and/or a helimagnetic thin film sample is modelled using a two-dimensional mesh. It has been shown in Sec. 3.6 that the demagnetisation energy contribution and the magnetisation variation in the out-of-film direction [40] radically change the energy landscape. Consequently, using these assumptions when the static properties of skyrmionic states are explored is not justified. Because of that, in this section, we investigate how these two assumptions affect the dynamics of the isolated Skyrmion (Sk) state in studied helimagnetic nanostructure. Firstly, we repeat the isolated skyrmion state simulations in a 150 nm diameter disk sample at zero external magnetic bias field, but this time we set the demagnetisation energy contribution w_{d} in Eq. (5.1) artificially to zero. Secondly, again in the absence of demagnetisation energy contribution, we simulate the Sk state dynamics under the same conditions, but this time using a two-dimensional mesh to model a thin film sample (i.e. not allowing the magnetisation variation in the out-of-film direction). We show the comparison of power spectral densities computed using three-dimensional and two-dimensional models in absence of demagnetisation energy contribution with the one computed using a full model in Fig. 5.13 (a) and Fig. 5.13 (b), for an in-plane and an out-of-plane excitation, respectively.

We observe that although the magnetisation dynamics of identified eigenmodes do not change significantly, the resonance frequencies of some eigenmodes change substantially. In the 3d simulations in absence of demagnetisation energy, while the frequency of eigenmode D remains approximately the same, the frequencies of eigenmodes A and B increase by 71% and 18%, respectively. On the other hand, the frequencies of eigenmodes E and G decrease by 14% and 21%, respectively. Furthermore, power spectral densities in Fig. 5.13 (b), computed for the out-of-plane excitation, show that the frequency of breathing eigenmode C increases by 17%, whereas the frequency of eigenmode F decreases by 34%.

If the thin film sample is modelled using a 2d mesh, which does not allow the magnetisation to vary in the z direction, the frequencies of lateral eigenmodes A, B, and G do not change significantly in comparison to the 3d model in absence of demagnetisation energy contribution. Although the frequency of eigenmode D does not change in the 3d simplified ($w_\mathrm{d} = 0$) model, neglecting the sample thickness, increases its frequency by 20%. The frequency of eigenmode E increases so that its frequency is approximately the same as in the full 3d model. In comparison to the 3d simplified model, the frequency of breathing eigenmodes C and F further increase by 19% and 7%, respectively. In the low frequency region of Fig. 5.13 (b) we observe several eigenmodes that are not present in the three-dimensional model. The number of existing eigenmodes is equal to the number of degrees of freedom in the system. This implies that in a two-dimensional mesh we have fewer existing eigenmodes. We believe the reason for this is that although the state is the same, its dynamics quilitatively changes at low frequencies due to the missing thickness dimension.

5.5 Summary

In this chapter we explored the dynamic properties of skyrmionic states in confined helimagnetic nanostructures. We employed two different methods: eigenvalue and ringdown methods. Eigenvalue method allowed us to compute all existing eigenmodes in studied skyrmionic states. However, what eigenmodes can be expeted to be present in power spectral densities strongly depends on the excitation used to perturb the system from its equilibrium state. Because of that, we performed ringdown simulations using two experimentally feasible excitations (in-plane and out-of-plane). We simulated all three skyrmionic states that can emerge in the studied system and found that for all these states, only one low frequency gyrotropic mode exists, which is in contrast to the magnetic bubble. This is a characteristic of massless skyrmion. We also examine what eigenmodes are present in the power spectral density when when a real FeGe Gilbert damping is used. Finally, we show that neglecting the demagnetisation energy and/or modelling helimagnetic nanostructures of finite thickness using two-dimensional meshes does not change the magnetisation dynamics associated to the existing eigenmodes, but

their frequencies are changed substantially. A more detailed discussion of the findings in this chapter is in Chapter 6.

Chapter 6

Conclusion

Through systematic micromagnetic study of equilibrium states in helimagnetic confined nanostructures we identified the ground states and reported the (meta)stability regions of other equilibrium states. We demonstrated that skyrmionic states in the form of incomplete Skyrmion (iSk) and isolated Skyrmion (Sk) configurations are the ground states in disk helimagnetic nanostructures, and that this occurs in a wide d–H (diameter–field) parameter space. Of particular importance is that iSk and Sk states are the ground states at zero external magnetic field which is in contrast to infinite thin film and bulk helimagnetic samples. We note that neither an external magnetic field is necessary nor magnetocrystalline anisotropy is required for this stability. We also note that there is significant flexibility in the skyrmionic state size which provides robustness for technology built on skyrmions, where fabrication of nanostructures and devices introduces unavoidable variation in geometries.

We have established that including the demagnetisation interaction is crucial for the system investigated here, i.e. in the absence of demagnetisation effects, there are other magnetisation configurations with energies lower than that of the incomplete and isolated skyrmion. We also note that the translational variation of the magnetisation from the lower side of the thin film to the top is essential for the physics reported here: if we use a two-dimensional micromagnetic simulation (i.e. assuming translational invariance of the magnetisation $\mathbf{m}$ in the out-of-plane direction), the isolated skyrmion configuration does not arise as the ground state. Our interpretation is that for skyrmion-like configurations the twist of $\mathbf{m}$ between top and bottom layer allows the system's energy to reduce significantly while such a reduction is less beneficial for other configurations such as helices; inline with recent predictions in the case of infinite thin films [40]. Accordingly, we conclude that three-dimensional helimagnetic nanostructure models, where demagnetisation energy contribution is neglected, or the geometry is approximated using a two-dimensional mesh, are not generally justified.

Because of the specific boundary conditions [41] and the importance of including the demagnetisation energy contribution, our predictions cannot be directly applied to other helimagnetic materials without repeating the stability study. For instance, although the size of skyrmionic states in this study was based on cubic FeGe helimagnetic material with helical period $L_{\mathrm{D}} = 70\,\mathrm{nm}$, in order to encourage the experimental verification of our predictions, this study could be repeated for materials with smaller L_{D}. In such materials the skyrmionic core size is considerably reduced, which allows the reduction of hosting nanostructure size and is an essential requirement for advancing future information storage technologies. Similarly, the ordering temperature of simulated FeGe helimagnetic material, $T_{\mathrm{C}} = 278.7\,\mathrm{K}$ [102], is lower than the room temperature, which means that a device operating at the room temperature cannot be constructed using this material. Because of that, we also demonstrate that our predictions are still valid if the ordering temperature of simulated B20 helimagnetic material is artificially increased to 350 K.

We demonstrate that skyrmionic states in confined helimagnetic nanostructures exhibit hysteretic behaviour as a consequence of energy barriers between energetically equivalent stable configurations (skyrmionic state core pointing up or down). In the absence of magnetocrystalline anisotropy and if the demagnetisation energy (demagnetisation-based shape anisotropy) is removed from the system's Hamiltonian, the hysteretic behaviour is still present, demonstrating the existence of a novel Dzyaloshinskii-Moriya-based shape anisotropy. Finally, we show how the reversal of the isolated skyrmion core orientation is facilitated by the Bloch point occurrence and propagation, and demonstrate that the Bloch point can propagate in both directions along the out-of-plane z direction.

Using the eigenvalue method, we compute all eigenmodes with frequencies below 50 GHz for the incomplete skyrmion, isolated skyrmion, and target states in helimagnetic thin film disk samples at zero external magnetic field. Because the eigenmodes that are present in the power spectral density depend strongly on the excitation used to perturb the system from its equilibrium state, we perform the ringdown simulations using two different experimentally feasible excitations (in-plane and out-of-plane). We demonstrate that in all three simulated states, two lateral and one breathing low-frequency eigenmodes exist as previously demonstrated in two-dimensional skyrmion lattice simulations [51] and microwave absorption measurements in bulk helimagnetic materials [52, 53, 54]. However, only one lateral eigenmode is gyrotropic, where the skyrmionic state core gyrates around its equilibrium position. The other lateral eigenmode we observe is not gyrotropic because it consists of a single contour ring (defined by the magnetisation z component distribution) revolving around the static skyrmionic state core. The existence of only one gyrotropic eigenmode is in accordance with the recent analytic (rigid skyrmion two-dimensional model) findings by Guslienko and Gareeva, [58] but in contrast to the magnetic bubble where two gyrotropic eigenmodes

were found. [55, 56, 57] Because the two gyrotropic eigenmodes with opposite gyration direction in a magnetic bubble imply it possesses mass, our findings suggest that the confined DMI-induced skyrmionic states in the studied system are massless. The low-frequency breathing eigenmode we observe, where a single magnetisation z component contour ring shrinks and expands periodically, is in accordance with findings in Ref. [51, 52, 53, 49, 54, 127, 128].

For the incomplete skyrmion and the isolated skyrmion states we find that the resonance frequencies depend nonlinearly on both the disk sample diameter and the external magnetic bias field. We observe that the frequency of the gyrotropic eigenmode approaches zero near the switching field H_{s} (where the reversal of skyrmionic state core occurs) for both incomplete skyrmion and isolated skyrmion states, suggesting that this eigenmode might be the reversal mode of studied skyrmionic states. We find that when the skyrmionic state core orientation reverses, the revolving direction of all lateral eigenmodes changes, which confirms that the revolving direction depends on the direction of gyrovector as shown in Ref. [51, 58].

After we identified all existing eigenmodes of iSk and Sk ground states, we compared their PSDs in the same sample at different external magnetic field values. We identified several characteristics that can contribute to the experimental identification of the state that emerged in the sample by measuring the resonance frequencies.

In the identification and analysis of eigenmodes, we used a small Gilbert damping value in order to provide enough separation between peaks in the Power Spectral Density (PSD). However, what eigenmodes are expected to be observed in experiments strongly depends on the real Gilbert damping value α. Therefore, we measure α in the FeGe thin film, and carry out ringdown simulations with this α. We show that for the incomplete skyrmion, two eigenmodes (gyrotropic and breathing) are present in the out-of-plane PSD, whereas only the gyrotropic eigenmode is present in the in-plane PSD. In the isolated skyrmion case, two lateral eigenmodes are present in the in-plane PSD, whereas a single breathing eigenmode is present in the out-of-plane PSD.

Our simulations take into account the demagnetisation energy contribution, which is usually neglected for simplicity in both analytic and simulation works. To explore the importance of model assumptions, we carry out further systematic simulation studies in which we set the demagnetisation energy contribution artificially to zero. We also repeat the simulations under the same conditions on 3d and 2d meshes (with and without permissible magnetisation variation in the out-of-film direction, respectively). We find that although the magnetisation dynamics of eigenmodes does not change significantly, their frequencies change substantially. This suggests that ignoring the demagnetisation energy contribution or approximating a thin film helimagnetic sample using a two-dimensional mesh is not always justified.

This work revealed some of the basic static and dynamic properties of skyrmionic states in confined helimagnetic nanostructures. The stability at zero external magnetic field and the ability to change the skyrmionic state core orientation using an external magnetic field, suggest that these states can be used for the development of skyrmion-based memory devices. This work provides a systematic dynamics study of skyrmionic states in confined helimagnetic nanostructures, which can be used as a reference guide for determining what skyrmionic state is present in the sample by measuring the set of resonance frequencies.

Appendix A

All eigenmodes of skyrmionic states computed using the eigenvalue method

In this Appendix, we show the schematic representations of all identified eigenmodes with frequencies below 50 GHz computed using the eigenvalue method. We show the incomplete Skyrmion (iSk) eigenmodes in Fig. A.1, isolated Skyrmion (Sk) eigenmodes in Figures A.2 and A.3, and Target (T) eigenmodes in Figures A.4 and A.5.

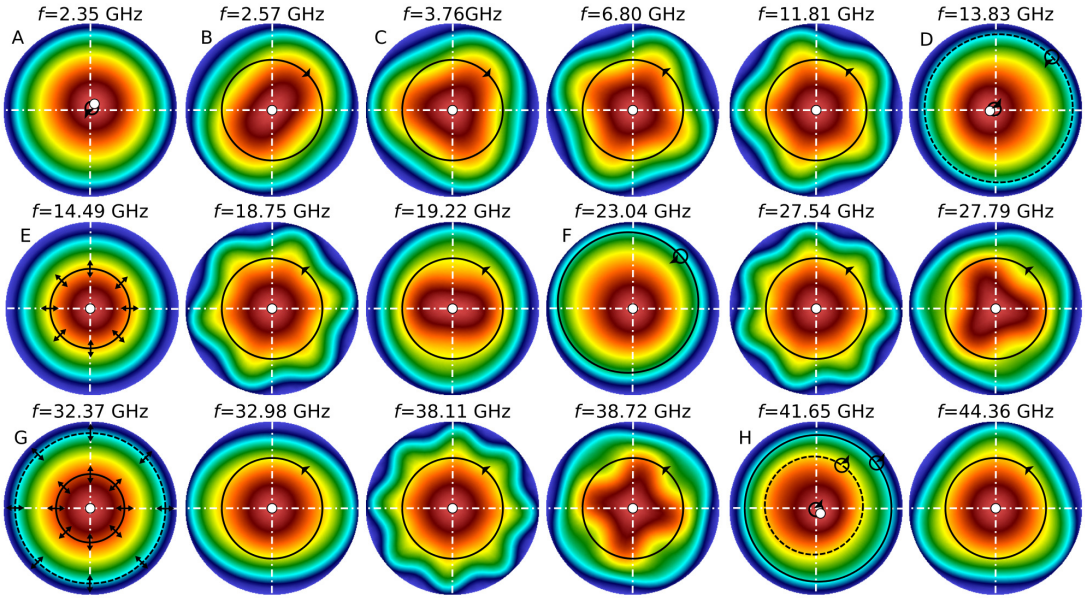

Figure A.1: The schematic representation of magnetisation dynamics corresponding to the identified eigenmodes in the $0-50$ GHz frequency range for an incomplete Skyrmion (iSk) state, obtained using the eigenvalue method. The simulated sample is a 80 nm diameter disk sample with 10 nm thickness at zero external magnetic bias field.

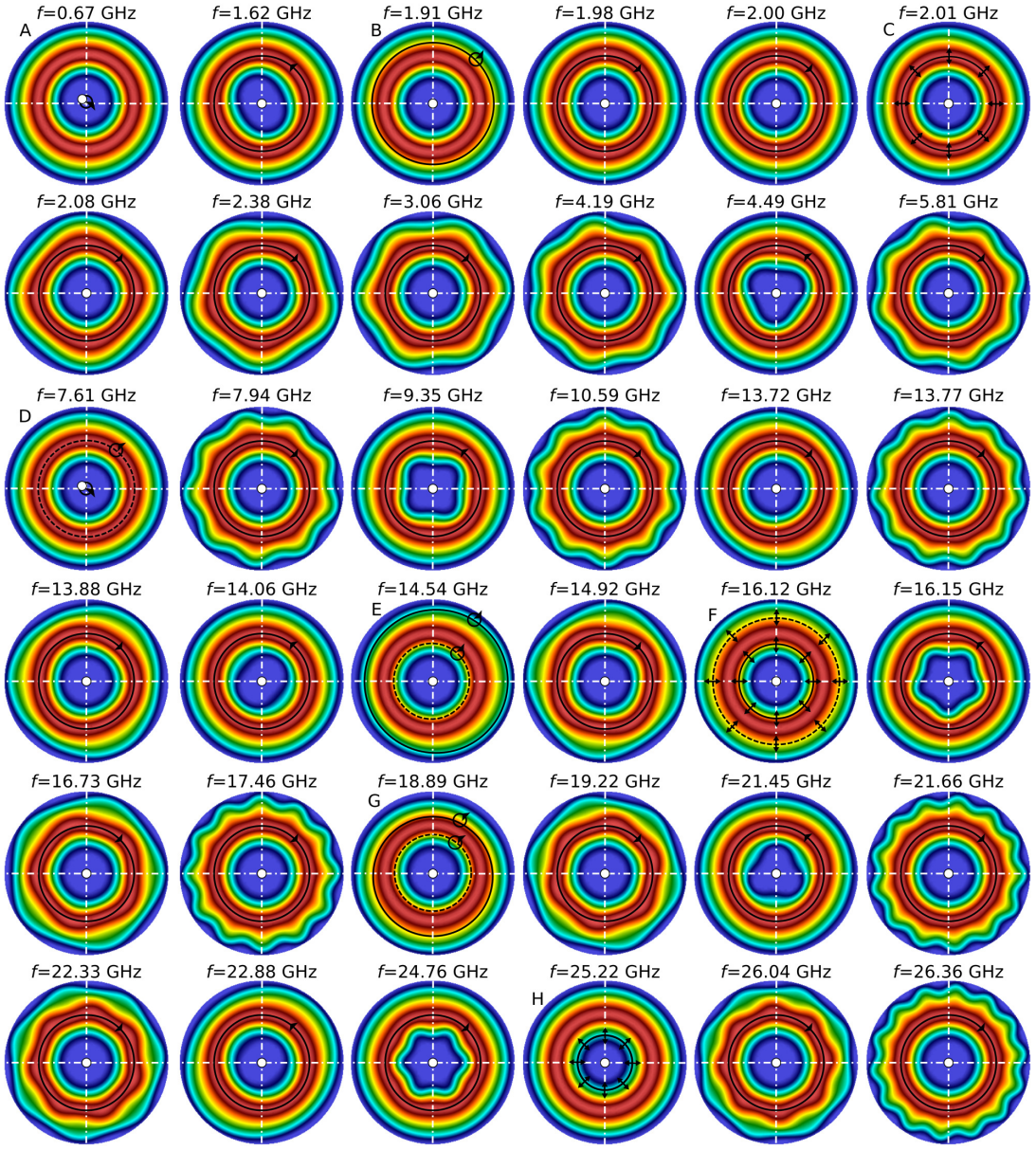

Figure A.2: The schematic representation of magnetisation dynamics corresponding to the identified eigenmodes in the $0 - 27\,\mathrm{GHz}$ frequency range for an isolated Skyrmion (Sk) state, obtained using the eigenvalue method. The simulated sample is a 150 nm diameter disk sample with 10 nm thickness at zero external magnetic bias field.

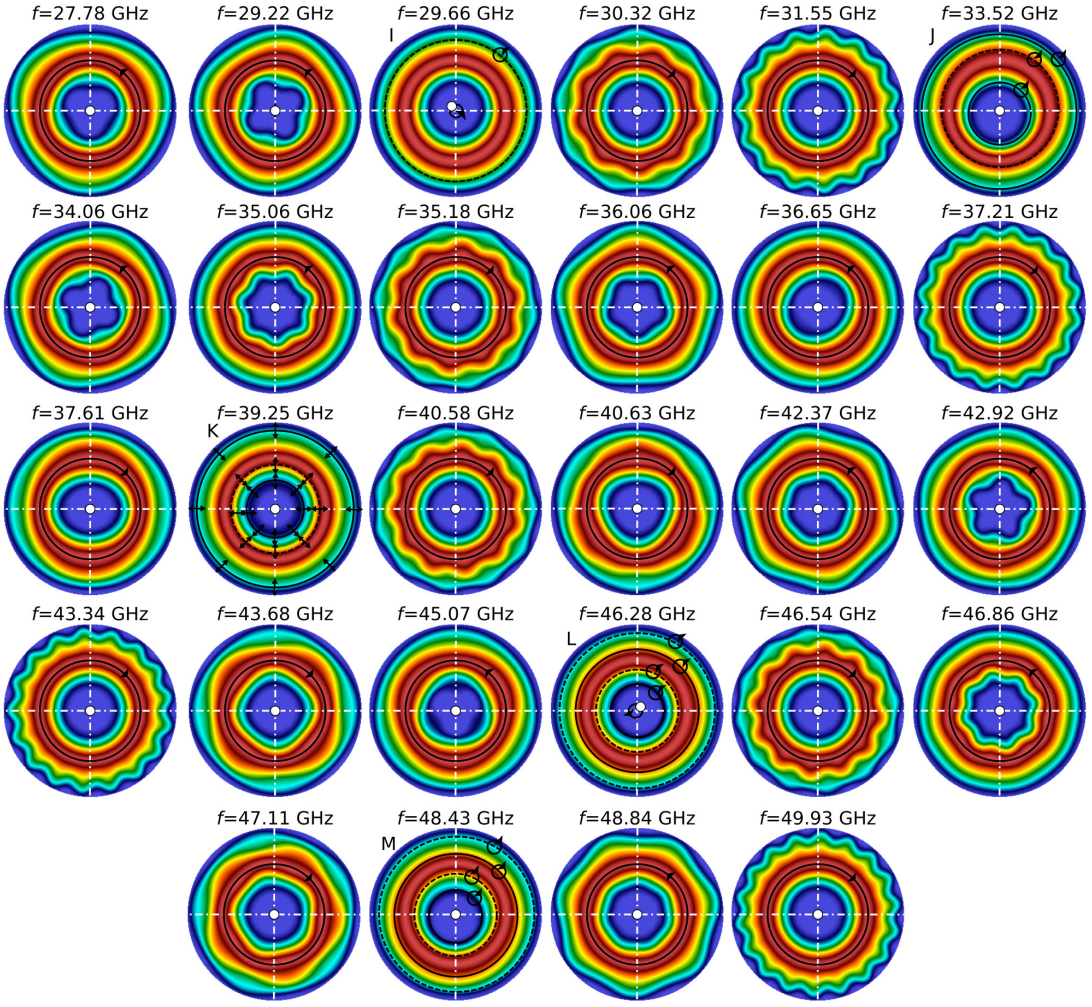

Figure A.3: The schematic representation of magnetisation dynamics corresponding to the identified eigenmodes in the $27 - 50\,\mathrm{GHz}$ frequency range for an isolated Skyrmion (Sk) state, obtained using the eigenvalue method. The simulated sample is a 150 nm diameter disk sample with 10 nm thickness at zero external magnetic bias field.

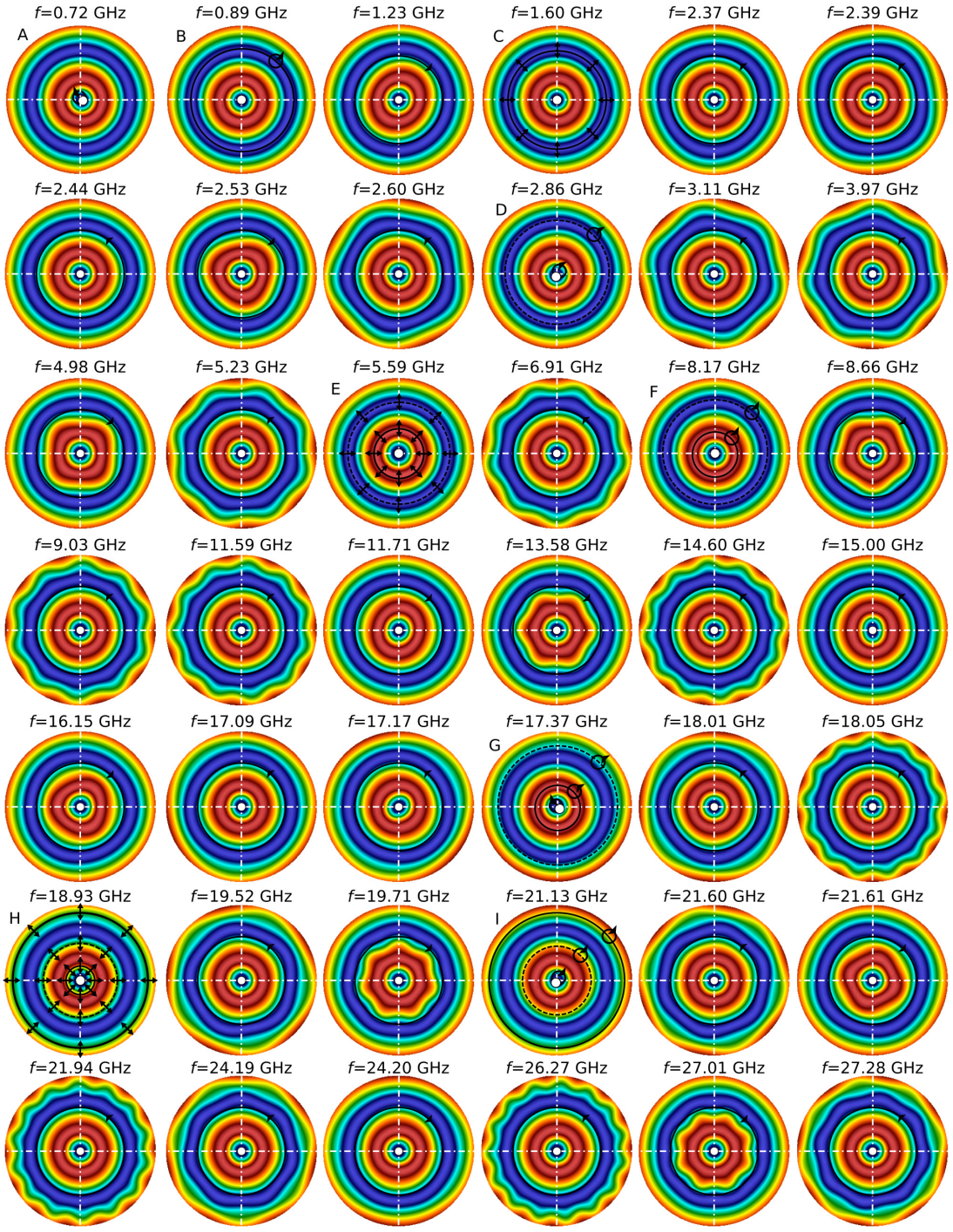

Figure A.4: The schematic representation of magnetisation dynamics corresponding to the identified eigenmodes in the $0 - 28\,\mathrm{GHz}$ frequency range for a Target (T) state, obtained using the eigenvalue method. The simulated sample is a 160 nm diameter disk sample with 10 nm thickness at zero external magnetic bias field.

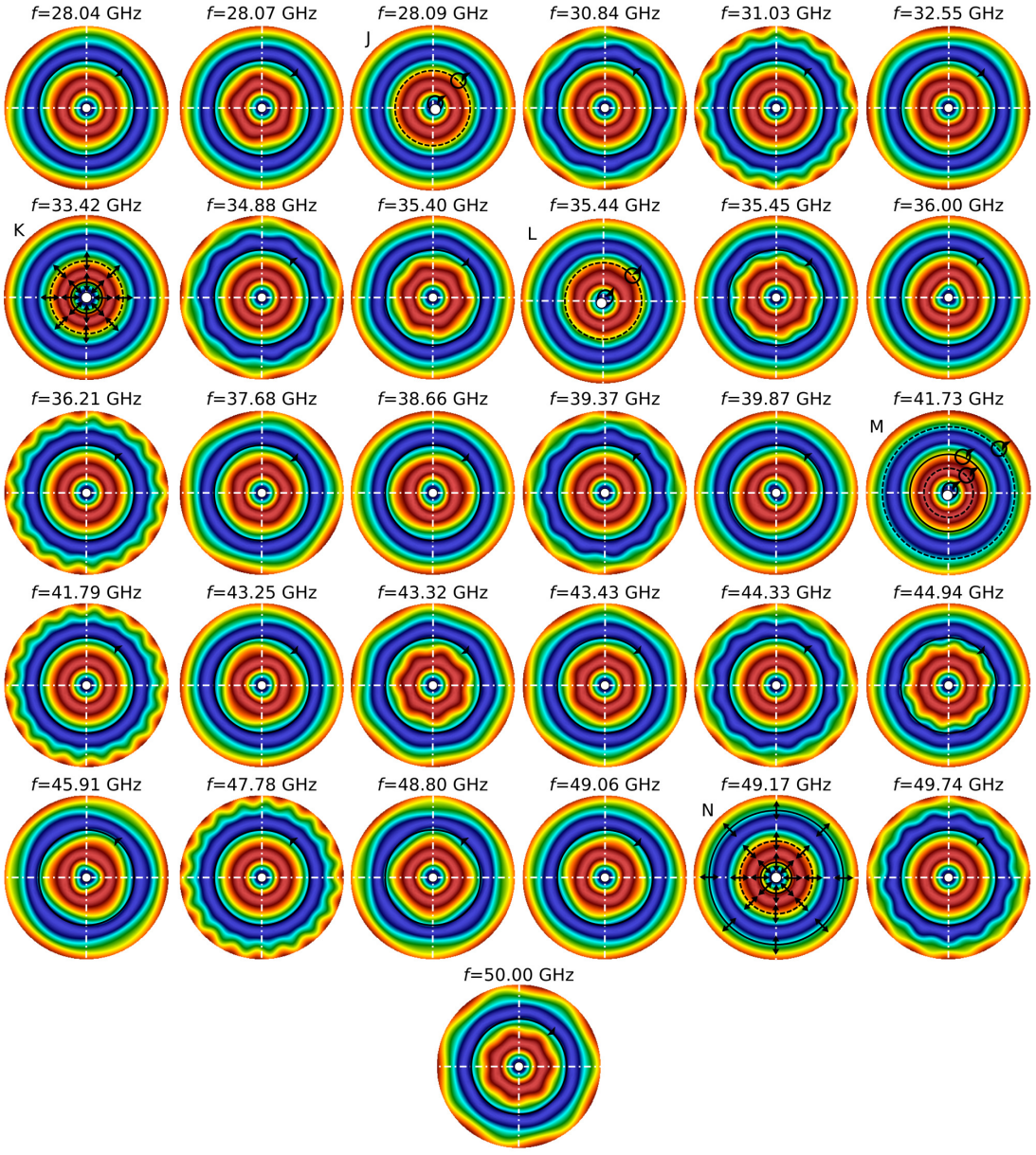

Figure A.5: The schematic representation of magnetisation dynamics corresponding to the identified eigenmodes in the $28 - 50\,\mathrm{GHz}$ frequency range for a Target (T) state, obtained using the eigenvalue method. The simulated sample is a 160 nm diameter disk sample with 10 nm thickness at zero external magnetic bias field.

References

[1] Richter, H. J. The transition from longitudinal to perpendicular recording. *J. Phys. D. Appl. Phys.* **40**, R149–R177 (2007).

[2] Dzyaloshinsky, I. A thermodynamic theory of weak ferromagnetism of antiferromagnetics. *J. Phys. Chem. Solids* **4**, 241–255 (1958).

[3] Moriya, T. Anisotropic superexchange interaction and weak ferromagnetism. *Phys. Rev.* **120**, 91–98 (1960).

[4] Moriya, T. New mechanism of anisotropic superexchange interaction. *Phys. Rev. Lett.* **4**, 228–230 (1960).

[5] Yang, H., Thiaville, A., Rohart, S., Fert, A. & Chshiev, M. Anatomy of Dzyaloshinskii-Moriya Interaction at Co/Pt Interfaces. *Phys. Rev. Lett.* **115**, 1–5 (2015).

[6] Fert, A. & Levy, P. M. Role of anisotropic exchange interactions in determining the properties of spin-glasses. *Phys. Rev. Lett.* **44**, 1538–1541 (1980).

[7] Crépieux, A. & Lacroix, C. Dzyaloshinsky-Moriya interactions induced by symmetry breaking at a surface. *J. Magn. Magn. Mater.* **182**, 341–349 (1998).

[8] Blundell, S. *Magnetism in Condensed Matter (Oxford Master Series in Physics)* (Oxford University Press, 2001), 1st edn.

[9] Aharoni, A. *Introduction to the Theory of Ferromagnetism (International Series of Monographs on Physics)* (Oxford University Press, 2001), 2nd edn.

[10] Bak, P. & Jensen, M. H. Theory of helical magnetic structures and phase transitions in MnSi and FeGe. *J. Phys. C Solid State Phys.* **13**, L881–L885 (1980).

[11] Vedmedenko, E., Udvardi, L., Weinberger, P. & Wiesendanger, R. Chiral magnetic ordering in two-dimensional ferromagnets with competing Dzyaloshinsky-Moriya interactions. *Phys. Rev. B* **75**, 104431 (2007).

[12] Bode, M. *et al.* Chiral magnetic order at surfaces driven by inversion asymmetry. *Nature* **447**, 190–193 (2007).

[13] Heide, M., Bihlmayer, G. & Blügel, S. Dzyaloshinskii-Moriya interaction accounting for the orientation of magnetic domains in ultrathin films: Fe/W(110). *Phys. Rev. B* **78**, 140403 (2008).

[14] Ferriani, P. *et al.* Atomic-scale Spin spiral with a unique rotational sense: Mn monolayer on W(001). *Phys. Rev. Lett.* **101**, 1–4 (2008).

[15] Rößler, U. K., Leonov, A. A. & Bogdanov, A. N. Chiral Skyrmionic matter in non-centrosymmetric magnets. *J. Phys. Conf. Ser.* **303**, 012105 (2011).

[16] Adams, T. *et al.* Long-wavelength helimagnetic order and skyrmion lattice phase in Cu2OSeO3. *Phys. Rev. Lett.* **108**, 1–5 (2012).

[17] Karhu, E. A. *et al.* Chiral modulations and reorientation effects in MnSi thin films. *Phys. Rev. B* **85**, 094429 (2012).

[18] Wilson, M. N., Butenko, A. B., Bogdanov, A. N. & Monchesky, T. L. Chiral skyrmions in cubic helimagnet films: The role of uniaxial anisotropy. *Phys. Rev. B* **89**, 094411 (2014).

[19] Heinze, S. *et al.* Spontaneous atomic-scale magnetic skyrmion lattice in two dimensions. *Nat. Phys.* **7**, 713–718 (2011).

[20] Kanazawa, N. *et al.* Possible skyrmion-lattice ground state in the B20 chiral-lattice magnet MnGe as seen via small-angle neutron scattering. *Phys. Rev. B* **86**, 134425 (2012).

[21] Romming, N. *et al.* Writing and deleting single magnetic skyrmions. *Science* **341**, 636–639 (2013).

[22] Jonietz, F. *et al.* Spin transfer torques in MnSi at ultralow current densities. *Science* **330**, 1648–1651 (2010).

[23] Yu, X. Z. *et al.* Skyrmion flow near room temperature in an ultralow current density. *Nat. Commun.* **3**, 988 (2012).

[24] Kiselev, N. S., Bogdanov, A. N., Schäfer, R. & Rößler, U. K. Chiral skyrmions in thin magnetic films: new objects for magnetic storage technologies? *J. Phys. D. Appl. Phys.* **44**, 392001 (2011).

[25] Fert, A., Cros, V. & Sampaio, J. Skyrmions on the track. *Nat. Nanotechnol.* **8**, 152–156 (2013).

[26] Zhang, X., Ezawa, M. & Zhou, Y. Magnetic skyrmion logic gates: conversion, duplication and merging of skyrmions. *Sci. Rep.* **5**, 9400 (2015).

[27] Bogdanov, A. N. & Yablonskii, D. A. Thermodynamically stable "vortices" in magnetically ordered crystals. The mixed state of magnets. *Sov. Phys. JETP* **68**, 101–103 (1989).

[28] Bogdanov, A. & Hubert, A. Stability of vortex-like structures in uniaxial ferromagnets. *J. Magn. Magn. Mater.* **195**, 182–192 (1999).

[29] Rößler, U. K., Bogdanov, A. N. & Pfleiderer, C. Spontaneous skyrmion ground states in magnetic metals. *Nature* **442**, 797–801 (2006).

[30] Mühlbauer, S. *et al.* Skyrmion lattice in a chiral magnet. *Science* **323**, 915–919 (2009).

[31] Yu, X. Z. *et al.* Near room-temperature formation of a skyrmion crystal in thin-films of the helimagnet FeGe. *Nat. Mater.* **10**, 106–109 (2011).

[32] Yu, X. Z. *et al.* Real-space observation of a two-dimensional skyrmion crystal. *Nature* **465**, 901–904 (2010).

[33] Seki, S., Yu, X. Z., Ishiwata, S. & Tokura, Y. Observation of skyrmions in a multiferroic material. *Science* **336**, 198–201 (2012).

[34] Editorial. Skyrmionics in sight. *Nat. Nanotechnol.* **8**, 883 (2013).

[35] Tokunaga, Y. *et al.* A new class of chiral materials hosting magnetic skyrmions beyond room temperature. *Nat. Commun.* **6**, 7638 (2015).

[36] Woo, S. *et al.* Observation of room-temperature magnetic skyrmions and their current-driven dynamics in ultrathin metallic ferromagnets. *Nat. Mater.* **15**, 501–506 (2016).

[37] Boulle, O. *et al.* Room-temperature chiral magnetic skyrmions in ultrathin magnetic nanostructures. *Nat. Nanotechnol.* **11**, 449–454 (2016).

[38] Jiang, W. *et al.* Blowing magnetic skyrmion bubbles. *Science* **349**, 283–286 (2015).

[39] Sampaio, J., Cros, V., Rohart, S., Thiaville, A. & Fert, A. Nucleation, stability and current-induced motion of isolated magnetic skyrmions in nanostructures. *Nat. Nanotechnol.* **8**, 839–844 (2013).

[40] Rybakov, F. N., Borisov, A. B. & Bogdanov, A. N. Three-dimensional skyrmion states in thin films of cubic helimagnets. *Phys. Rev. B* **87**, 094424 (2013).

[41] Rohart, S. & Thiaville, A. Skyrmion confinement in ultrathin film nanostructures in the presence of Dzyaloshinskii-Moriya interaction. *Phys. Rev. B* **88**, 184422 (2013).

[42] Du, H., Ning, W., Tian, M. & Zhang, Y. Magnetic vortex with skyrmionic core in a thin nanodisk of chiral magnets. *EPL* **101**, 37001 (2013).

[43] Leonov, A. O., Rößler, U. K. & Mostovoy, M. Target-skyrmions and skyrmion clusters in nanowires of chiral magnets. *EPJ Web Conf.* **75**, 05002 (2014).

[44] Du, H., Ning, W., Tian, M. & Zhang, Y. Field-driven evolution of chiral spin textures in a thin helimagnet nanodisk. *Phys. Rev. B* **87**, 014401 (2013).

[45] Guslienko, K. Y. Skyrmion state stability in magnetic nanodots with perpendicular anisotropy. *IEEE Magn. Lett.* **6**, 1–4 (2015).

[46] Buda, L. D., Prejbeanu, I. L., Demand, M., Ebels, U. & Punadjela, K. Vortex states stability in circular Co(0001) dots. *IEEE Trans. Magn.* **37**, 2061–2063 (2001).

[47] Moutafis, C. *et al.* Magnetic bubbles in FePt nanodots with perpendicular anisotropy. *Phys. Rev. B* **76**, 104426 (2007).

[48] Moutafis, C., Komineas, S., Vaz, C. A. F., Bland, J. A. C. & Eames, P. Vortices in ferromagnetic elements with perpendicular anisotropy. *Phys. Rev. B* **74**, 214406 (2006).

[49] Kim, J. V. *et al.* Breathing modes of confined skyrmions in ultrathin magnetic dots. *Phys. Rev. B* **90**, 064410 (2014).

[50] Gareeva, Z. V. & Guslienko, K. Y. Magnetic skyrmion dynamics in thin cylindrical dots. *Phys. status solidi - Rapid Res. Lett.* **10**, 227–232 (2016).

[51] Mochizuki, M. Spin-wave modes and their intense excitation effects in skyrmion crystals. *Phys. Rev. Lett.* **108**, 017601 (2012).

[52] Onose, Y., Okamura, Y., Seki, S., Ishiwata, S. & Tokura, Y. Observation of magnetic excitations of skyrmion crystal in a helimagnetic insulator Cu2OSeO3. *Phys. Rev. Lett.* **109**, 037603 (2012).

[53] Okamura, Y. *et al.* Microwave magnetoelectric effect via skyrmion resonance modes in a helimagnetic multiferroic. *Nat. Commun.* **4**, 2391 (2013).

[54] Schwarze, T. *et al.* Universal helimagnon and skyrmion excitations in metallic, semiconducting and insulating chiral magnets. *Nat. Mater.* **14**, 478–483 (2015).

[55] Makhfudz, I., Krüger, B. & Tchernyshyov, O. Inertia and chiral edge modes of a skyrmion magnetic bubble. *Phys. Rev. Lett.* **109**, 217201 (2012).

[56] Moutafis, C., Komineas, S. & Bland, J. A. C. Dynamics and switching processes for magnetic bubbles in nanoelements. *Phys. Rev. B* **79**, 224429 (2009).

[57] Büttner, F. *et al.* Dynamics and inertia of skyrmionic spin structures. *Nat. Phys.* **11**, 225–228 (2015).

[58] Gusliyenko, K. Y. & Gareeva, Z. Gyrotropic skyrmion modes in ultrathin magnetic circular dots. *IEEE Magn. Lett.* **7**, 1–1 (2016).

[59] D'Aquino, M., Serpico, C., Miano, G. & Forestiere, C. A novel formulation for the numerical computation of magnetization modes in complex micromagnetic systems. *J. Comput. Phys.* **228**, 6130–6149 (2009).

[60] McMichael, R. D. & Stiles, M. D. Magnetic normal modes of nanoelements. *J. Appl. Phys.* **97**, 10J901 (2005).

[61] Griffiths, D. J. *Introduction to Electrodynamics* (Addison-Wesley, 2012), 4th edn.

[62] Richardson, O. W. A mechanical effect accompanying magnetization. *Phys. Rev. (Series I)* **26**, 248–253 (1908).

[63] Einstein, A. Experimenteller Nachweis der Ampèreschen Molekularströme. *Naturwissenschaften* **3**, 237–238 (1915).

[64] Einstein, A. & de Haas, W. J. Experimental proof of the existence of Ampère's molecular currents. *K. Ned. Akad. van Wet. Proc.* **15**, 696–711 (1915).

[65] Barnett, S. J. Magnetization by Rotation. *Phys. Rev.* **6**, 239–270 (1915).

[66] Bohr, N. I. On the constitution of atoms and molecules. *Philos. Mag. Ser. 6* **26**, 1–25 (1913).

[67] Bohr, N. XXXVII. On the constitution of atoms and molecules. *Philos. Mag. Ser. 6* **26**, 476–502 (1913).

[68] Griffiths, D. J. *Introduction to Quantum Mechanics* (Pearson Prentice Hall, 2004), 2nd edn.

[69] Shankar, R. *Principles of Quantum Mechanics* (Plenum Press, 2011), 2nd edn.

[70] Sakurai, J. J. & Napolitano, J. *Modern Quantum Mechanics* (Addison-Wesley, 2011), 2nd edn.

[71] Dirac, P. *The Principles of Quantum Mechanics (International Series of Monographs on Physics)* (Oxford University Press, 1982), 4th edn.

[72] O'Handley, R. C. *Modern Magnetic Materials: Principles and Applications* (Wiley-Interscience, 1999), 1st edn.

[73] Craik, D. J. *Magnetism: Principles and Applications* (Wiley, 1995), 1st edn.

[74] Gerlach, W. & Stern, O. Das magnetische Moment des Silberatoms. *Zeitschrift für Phys.* **9**, 353–355 (1922).

[75] Morrison, M. Spin: All is not what it seems. *Stud. Hist. Philos. Sci. Part B - Stud. Hist. Philos. Mod. Phys.* **38**, 529–557 (2007).

[76] Weinert, F. Wrong theoryRight experiment: The significance of the Stern-Gerlach experiments. *Stud. Hist. Philos. Sci. Part B Stud. Hist. Philos. Mod. Phys.* **26**, 75–86 (1995).

[77] Quinet, P. & Biémont, E. Landé g-factors for experimentally determined energy levels in doubly ionized lanthanides. *At. Data Nucl. Data Tables* **87**, 207–230 (2004).

[78] Landau, L. & Lifshits, E. On the theory of the dispersion of magnetic permeability in ferromagnetic bodies. *Phys. Zeitsch. der Sow.* **8**, 153–169 (1935).

[79] Gilbert, T. L. A phenomenological theory of damping in ferromagnetic materials. *IEEE Trans. Magn.* **40**, 3443–3449 (2004).

[80] Krüger, B. *Current-driven magnetization dynamics: Analytical modeling and numerical simulation dissertation.* Ph.D. thesis, Universität Hamburg (2011).

[81] Heisenberg, W. Mehrkörperproblem und Resonanz in der Quantenmechanik. *Zeitschrift für Phys.* **38**, 411–426 (1926).

[82] Heide, M., Bihlmayer, G. & Blügel, S. Describing Dzyaloshinskii-Moriya spirals from first principles. *Phys. B Condens. Matter* **404**, 2678–2683 (2009).

[83] Kong, L. & Zang, J. Dynamics of an insulating skyrmion under a temperature gradient. *Phys. Rev. Lett.* **111**, 1–5 (2013).

[84] Garca-Cervera, C. J., Gimbutas, Z. & E, W. Accurate numerical methods for micromagnetics simulations with general geometries. *J. Comput. Phys.* **184**, 37–52 (2003).

[85] Buhrandt, S. & Fritz, L. Skyrmion lattice phase in three-dimensional chiral magnets from Monte Carlo simulations. *Phys. Rev. B* **88**, 195137 (2013).

[86] Geuzaine, C. & Remacle, J.-F. Gmsh: A 3-D finite element mesh generator with built-in pre- and post-processing facilities. *Int. J. Numer. Methods Eng.* **79**, 1309–1331 (2009).

[87] Schrefl, T. *et al.* Numerical Methods in Micromagnetics (Finite Element Method). In *Handb. Magn. Adv. Magn. Mater.*, 1–30 (John Wiley & Sons, Ltd, Chichester, UK, 2007).

[88] Andreas, C. *Multiscale Multimodel Simulation of Micromagnetic Singularities.* Ph.D. thesis, Jülich Forschungszentrums (2014).

[89] Logg, A., Mardal, K. A. & Wells, G. N. *Automated solution of differential equations by the finite element method*, vol. 84 of *Lecture Notes in Computational Science and Engineering* (Springer Berlin Heidelberg, Berlin, Heidelberg, 2012).

[90] Franchin, M. *Multiphysics simulations of magnetic nanostructures.* Phd thesis, University of Southampton (2009).

[91] Cohen, S. D., Hindmarsh, A. C. & Dubois, P. F. CVODE, a stiff/nonstiff ODE solver in C. *Comput. Phys.* **10**, 138 (1996).

[92] Hindmarsh, A. C. *et al.* SUNDIALS: Suite of nonlinear and differential/algebraic equation solvers. *ACM Trans. Math. Softw.* **31**, 363–396 (2005).

[93] Fischbacher, T., Franchin, M., Bordignon, G. & Fangohr, H. A systematic approach to multiphysics extensions of finite-element-based micromagnetic simulations: Nmag. *IEEE Trans. Magn.* **43**, 2896–2898 (2007).

[94] Hunter, J. D. Matplotlib: A 2D graphics environment. *Comput. Sci. Eng.* **9**, 99–104 (2007).

[95] Ahrens, J., Geveci, B. & Law, C. *ParaView: An end-user tool for large data visualization* (Elsevier, 2005).

[96] Wilhelm, H. *et al.* Confinement of chiral magnetic modulations in the precursor region of FeGe. *J. Phys. Condens. Matter* **24**, 294204 (2012).

[97] Huang, S. X. & Chien, C. L. Extended skyrmion phase in epitaxial FeGe(111) thin films. *Phys. Rev. Lett.* **108**, 267201 (2012).

[98] Pauling, L. & Soldate, A. M. The nature of the bonds in the iron silicide, FeSi, and related crystals. *Acta Crystallogr.* **1**, 212–216 (1948).

[99] Richardson, M. The partial equilibrium diagram of the Fe-Ge system in the range 40-72 at. % Ge, and the crystallisation of some iron germanides by chemical transport reactions. *Acta Chem. Scand.* **21**, 2305–2317 (1967).

[100] Yamada, H. Electronic structure and magnetism of FeGe with B20-type structure. *Phys. B Condens. Matter* **329-333**, 1131–1133 (2003).

[101] Grigoriev, S. V. *et al.* Critical fluctuations in MnSi near Tc: A polarized neutron scattering study. *Phys. Rev. B* **72**, 134420 (2005).

[102] Lebech, B., Bernhard, J. & Freltoft, T. Magnetic structures of cubic FeGe studied by small-angle neutron scattering. *J. Phys. Condens. Matter* **1**, 6105–6122 (1989).

[103] Hamrle, J. *et al.* Determination of exchange constants of Heusler compounds by Brillouin light scattering spectroscopy: application to Co2 MnSi. *J. Phys. D. Appl. Phys.* **42**, 084005 (2009).

[104] Braun, H. B. Topological effects in nanomagnetism: from superparamagnetism to chiral quantum solitons. *Adv. Phys.* **61**, 1–116 (2012).

[105] Schulz, T. *et al.* Emergent electrodynamics of skyrmions in a chiral magnet. *Nat. Phys.* **8**, 301–304 (2012).

[106] Lee, M., Kang, W., Onose, Y., Tokura, Y. & Ong, N. Unusual Hall effect anomaly in MnSi under pressure. *Phys. Rev. Lett.* **102**, 186601 (2009).

[107] Dittrich, R. *et al.* A path method for finding energy barriers and minimum energy paths in complex micromagnetic systems. *J. Magn. Magn. Mater.* **250**, 12–19 (2002).

[108] Suess, D. *et al.* Reliability of Sharrocks equation for exchange spring bilayers. *Phys. Rev. B* **75**, 174430 (2007).

[109] Bessarab, P. F., Uzdin, V. M. & Jónsson, H. Method for finding mechanism and activation energy of magnetic transitions, applied to skyrmion and antivortex annihilation. *Comput. Phys. Commun.* **196**, 335–347 (2015).

[110] Rybakov, F. N., Borisov, A. B., Blügel, S. & Kiselev, N. S. New Type of Stable Particlelike States in Chiral Magnets. *Phys. Rev. Lett.* **115**, 117201 (2015).

[111] Zhao, X. *et al.* Direct imaging of magnetic field-driven transitions of skyrmion cluster states in FeGe nanodisks. *Proc. Natl. Acad. Sci.* **113**, 4918–4923 (2016).

[112] Feldtkeller, E. Mikromagnetisch stetige und unstetige Magnetisierungskonfigurationen. *Z. Angew. Phys.* **19**, 530–536 (1965).

[113] Döring, W. Point singularities in micromagnetism. *J. Appl. Phys.* **39**, 1006–1007 (1968).

[114] Andreas, C., Kákay, A. & Hertel, R. Multiscale and multimodel simulation of Bloch-point dynamics. *Phys. Rev. B* **89**, 134403 (2014).

[115] Slonczewski, J. C. Properties of Bloch points in bubble domains. *AIP Conf. Proc.* **24**, 613–614 (1975).

[116] Thiaville, A., García, J., Dittrich, R., Miltat, J. & Schrefl, T. Micromagnetic study of Bloch-point-mediated vortex core reversal. *Phys. Rev. B* **67**, 094410 (2003).

[117] Elías, R. G. & Verga, A. Magnetization structure of a Bloch point singularity. *Eur. Phys. J. B* **82**, 159–166 (2011).

[118] Oliphant, T. E. Python for Scientific Computing. *Comput. Sci. Eng.* **9**, 10–20 (2007).

[119] van der Walt, S., Colbert, S. C. & Varoquaux, G. The NumPy Array: A Structure for Efficient Numerical Computation. *Comput. Sci. Eng.* **13**, 22–30 (2011).

[120] Venkat, G. *et al.* Proposal for a Standard Micromagnetic Problem: Spin Wave Dispersion in a Magnonic Waveguide. *IEEE Trans. Magn.* **49**, 524–529 (2013).

[121] Baker, A. *et al.* Proposal of a micromagnetic standard problem for ferromagnetic resonance simulations. *J. Magn. Magn. Mater.* **421**, 428–439 (2017).

[122] Antoniou, A. *Digital Signal Processing: Signals, Systems, and Filters* (McGraw-Hill Professional, 2005).

[123] Beg, M. *et al.* Ground state search, hysteretic behaviour, and reversal mechanism of skyrmionic textures in confined helimagnetic nanostructures. *Sci. Rep.* **5**, 17137 (2015).

[124] Xiaomin L., Rantschler, J., Alexander, C. & Zangari, G. High-frequency behavior of electrodeposited Fe-Co-Ni alloys. *IEEE Trans. Magn.* **39**, 2362–2364 (2003).

[125] Kalarickal, S. S. *et al.* Ferromagnetic resonance linewidth in metallic thin films: Comparison of measurement methods. *J. Appl. Phys.* **99**, 093909 (2006).

[126] Kawai, T., Itabashi, A., Ohtake, M., Takeda, S. & Futamoto, M. Gilbert damping constant of FePd alloy thin films estimated by broadband ferromagnetic resonance. *EPJ Web Conf.* **75**, 02002 (2014).

[127] Wang, W., Beg, M., Zhang, B., Kuch, W. & Fangohr, H. Driving magnetic skyrmions with microwave fields. *Phys. Rev. B* **92**, 020403 (2015).

[128] Zhang, B., Wang, W., Beg, M., Fangohr, H. & Kuch, W. Microwave-induced dynamic switching of magnetic skyrmion cores in nanodots. *Appl. Phys. Lett.* **106**, 102401 (2015).